Thesis for Degree of Doctor of Philosophy

Growth, fabrication, and optical properties of high-quality two-dimensional van der Waals heterostructures

（高品質原子層ヘテロ積層構造の合成・創成とその光学特性の研究）

Mitsuhiro Okada

岡田 光博

Department Chemistry, Graduate School of Science

Nagoya University

2018

Contents

Preface

Under the supervision of Professor Hisanori Shinohara at Department of Chemistry, Graduate School of Science and Institute for Advanced Research, Nagoya University, the studies in this thesis were carried out from April 2015 to January 2018. These studies focus on the growth, fabrication, and optical properties of group-VI transition-metal dichalcogenides and their heterostructures.

First, I would like to express appreciation to my supervisor, Prof. Hisanori Shinohara, for his strenuous support of my Ph.D. studies and for related discussions. While conducting research in the Nano-structured Materials Laboratory, I learned numerous research-related skills, including techniques and field-specific knowledge, and was motivated to conduct research. I am lucky to have been afforded the opportunity to conduct research under Prof. H. Shinohara, whom I consider an exemplary researcher.

I also offer sincere thanks to Assoc. Prof. Ryo Kitaura, an adviser who frequently offered fruitful discussions. He answered every question when I requested help. Without his advice and support, my research would have suffered. I wish him success in his future studies. I also thank Asst. Prof. Haruka Omachi, Asst. Prof. Yusuke Nakanishi, and my collaborators, especially Dr. Kenji Watanabe and Dr. Takashi Taniguchi (National Institute for Materials Science, Japan), who graciously provided high-quality hexagonal boron nitride samples. I extend many thanks to my collaborators, Dr. Alex

Kutana, Mr. Sunny Gupta, and Prof. Boris I. Yakobson (Department of Materials Science & Nanoengineering, Rice University, USA); Prof. Kazunari Matsuda (Institute of Advanced Energy, Kyoto University, Japan); Assoc. Prof. Yuhei Miyauchi (Institute of Advanced Energy, Kyoto University and Itami Molecular Nanocarbon Project, Nagoya University, Japan); Mr. Yu Kobayashi, Mr. Tetsuki Saito, and Assoc. Prof. Yasumitsu Miyata (Department of Physics, Tokyo Metropolitan University, Japan); Prof. Hiroki Hibino (former: NTT Basic Research Laboratories; present: Department of Nanotechnology for Sustainable Energy, Kwansei Gakuin University, Japan); Prof. Yuika Saito (Department of Chemistry, Gakushuin University, Japan); Prof. Kenichiro Itami (Itami Molecular Nanocarbon Project, Nagoya University, Japan); as well as Dr. Yoshikatsu Sato and Prof. Tetsuya Higashiyama (Higashiyama Live Holonics Project, Nagoya University, Japan), for their support and intelligent commentary on my research. Many thanks are also due to Prof. Jamie H. Warner and all the lab members of the Nano-Structured Materials Group in the Department of Materials, University of Oxford, UK for hosting me.

I would like to thank all members of the Shinohara Group for helpful discussions and support. Dr. Yuki Sasaki, in particular, provided extensive advice on multiple occasions. I am also grateful for the support from Ms. Ryoko Ogawa (former) and Ms. Eiko Hattori, who are the secretaries of our group.

My Ph.D. study was supported by three scholarships. I would like to express my gratitude to the Japan Society for the Promotion of Science (JSPS) for a Research Fellowship for Young Scientists (DC2). Also, I got financial supports from “International Research Experience for Young Scientists in Graduate School of Science,” Nagoya University and the Program for Leading Graduate Schools in Nagoya

University “Integrative Graduate Education and Research Program in Green Natural Sciences (IGER)” of MEXT, Japan. This financial support enabled me to focus on research and acquire the experience and knowledge necessary to be a researcher.

Finally, I would like to thank my family for supporting me intellectually, mentally, and financially throughout my life. My father and Ms. Sachiko Nakane, in particular, provided extensive and unquestionable support, for which I am very grateful.

Mitsuhiro Okada

Department of Chemistry, Graduate School of Science

Nagoya University

January, 2018

Chapter 1
1.General Introduction

1.1. Two-dimensional materials

Since Novoselov and Geim reported the isolation of graphene—the monolayer limit of graphite—and demonstrated its unique electrical properties in 2004 (and were awarded the Nobel Prize in Physics in 2010), two-dimensional (2D) materials have been attracting intensive attention because of their unique optical and electrical properties [1-5].

Two-dimensional materials are layered materials with a typical thickness of approximately 1 nm or less; they exhibit unique characteristics as a consequence of their ultimate thinness and structure. For example, graphene exhibits an extremely high carrier mobility of over 200,000 $cm^2/(V \cdot s)$ at 5 K [6]. This phenomenon originates from its unique band structure with linear band dispersion called as Dirac cone around the K point in the Brillouin zone. Numerous 2D materials exhibit various unusual characteristics. For example, hexagonal boron nitride (hBN) is also an atomic layered material and its band gap is 5.97 eV [7]. In addition, MoS_2 and WS_2, which are group-VI transition-metal dichalcogenides (TMDC), are semiconductors when in their 2H state [8,9].

1.2. Group-VI TMDC

Group-VI TMDC are layered materials composed of a group-VI transition metal (Mo or W) and a chalcogen (S, Se, or Te). Their structures are shown in Figure 1.1. They are three-atom thick-layered materials in which transition-metal layers are sandwiched by chalcogen layers with trigonal prismatic geometries at 2H phase. Their structure is shown in Figure 1.1 These layers are bonded by van der Waals (vdW) interactions, and their crystals can be easily exfoliated into monolayers from bulk TMDC [5,10].

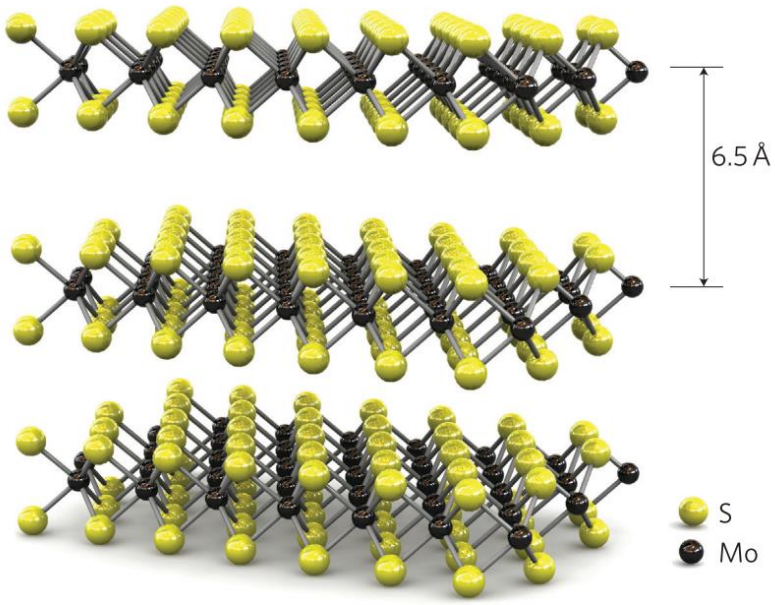

Figure 1.1. A schematic of the crystal structure of MoS_2. [11] .

Recent studies have revealed fascinating properties of monolayer TMDC not only for electrical applications but also for exploring the fundamental physics related to the 2D limit. For example, Radisavljevic *et al.* fabricated a high-mobility monolayer MoS_2 transistor as a high-K dielectric whose carrier mobility reaches 200 $cm^2/(V \cdot s)$ with a high on/off ratio that exceeds 10^8 even at room temperature [11]. In 2012, Xiao *et al.*

reported the possibility of achieving valleytronics using MoS_2 [4]. Valleytronics is a new basic principle of devices based on the valley degree of freedom—i.e., the freedom of moment of carriers in k-space—instead of on the charge or spin degree of freedom (electronics or spintronics, respectively). And TMDC show strong PL emission from exciton and trion even in room temperature because of their low-dimensional structure [5,10,12]. This means that they are excellent field for exploring 2D exciton physics. These reports clearly indicate that MoS_2 and other group-VI TMDC can play an important role in replacing silicon transistors in the future and provide an excellent opportunity for exploring the fundamental physics of the 2D limit.

1.3. Band structure of Group-VI TMDC

The band structures of MoS_2 and WS_2 as well as their layer-number dependence are shown illustrated in Figure 1.2.

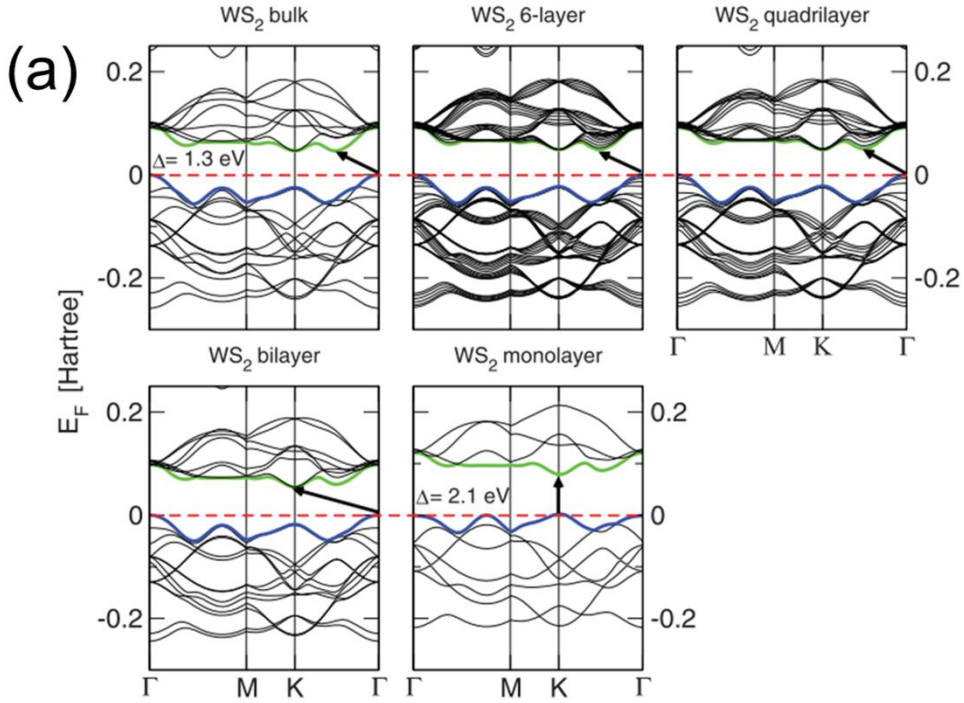

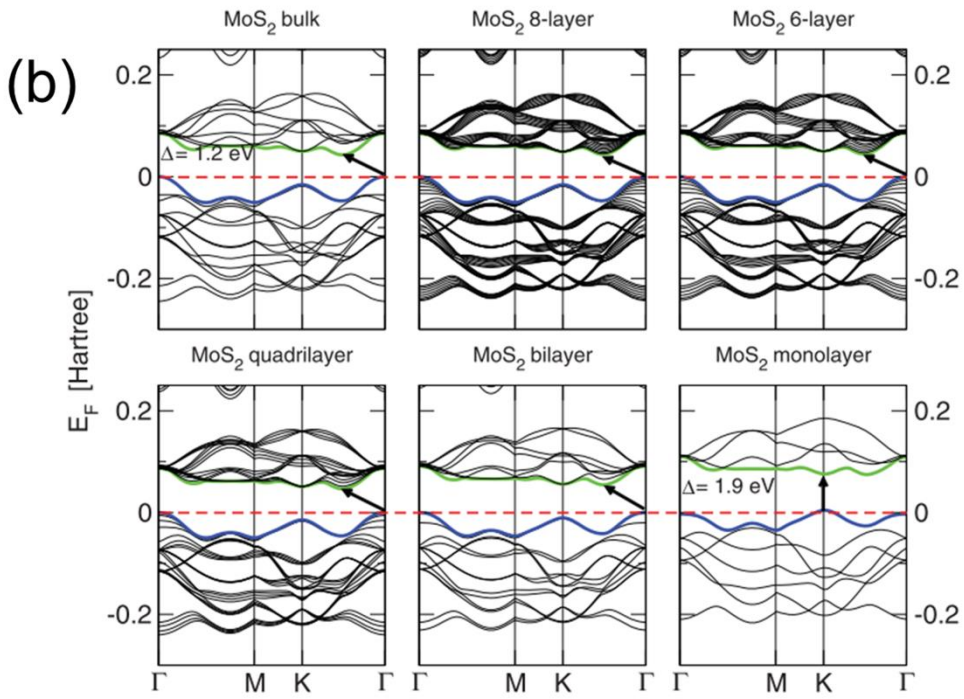

Figure 1.2. Band structures and layer-number dependence of the band structures of (a): WS_2 and (b): MoS_2 [13].

As shown in Figure 1.2, the band structures of monolayer TMDC are observed to differ from those of the corresponding bulk materials, and because W and Mo atoms are members of the same group of the periodic table, W- and Mo-based TMDC exhibit very similar band structures. Bulk WS_2 and MoS_2 are indirect-gap semiconductors; by contrast, monolayer WS_2 and MoS_2 are direct-gap semiconductors. This difference is caused by the spatial distribution of wave function. In MoS_2, band dispersion of conduction band around the K point mainly arises from the *d*-orbitals of Mo atoms which localized at the center of the layer, which means that the bands do not suffer effects caused by multiple layers. By contrast, band dispersion near the Γ and Q point (point between K and Γ point) arises from the linear combination of *d*-orbitals of the metal and the antibonding p_z orbitals of sulfur. Because sulfur atoms are located at the surface, they are affected by interlayer coupling, making multilayer TMDC indirect-gap

semiconductors [10].

In the 2H phase and odd-layer TMDC, spin splitting at the K point and the K′ point in the first Brillouin zone is inversed (Figure 1.3) [4]. These inequivalent valleys of K and K′ points lead to the valley degree of freedom.

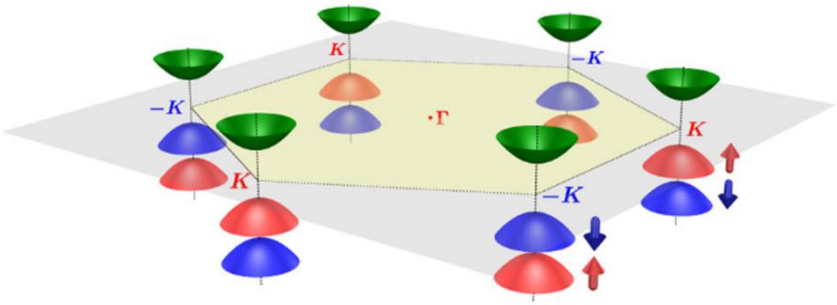

Figure 1.3. Schematic of the band structure around band edges at K and –K (K´) points in monolayer MoS_2 [4].

These inequivalent valleys of K and K´ points make different, leading to formation of valley degree of freedom.

1.4. Optical properties of group-VI TMDC

Because TMDC are crystallographic and layered semiconductors, they exhibit unique Raman and photoluminescence (PL) properties. Raman and PL spectra are used to evaluate TMDC because these techniques provide important information about the materials layer numbers and quality and these methods are easy and inexpensive. And due to the unique structure of TMDC, they show higher order excitonic effect and specific Raman mode at low frequency region. These phenomena mean that group-VI TMDC is excellent field for exploring fundamental optics in 2D limit.

1.4.1. Raman spectra of TMDC

Raman scattering was discovered by C. V. Raman, who was awarded the Nobel Prize in Physics in 1930. The Raman effect refers to the inelastic scattering of photons by phonons in a crystal. Because this effect is caused by the phonon mode in crystals and is specific to the crystal structure and composition of a material, the vibrational modes in a specimen can be characterized on the basis of its Raman spectrum.

E′ and A'_1 Raman scattering modes of MoS_2 and WS_2 are well documented [14-16]. These scattering modes correspond to in-plane and out-of-plane vibrations, respectively (Figure 1.5). The layer-number dependence of these peaks has also been well researched. Figure 1.6 shows the layer-number dependence of the peak positions of the E′ and A'_1 modes in WS_2 and MoS_2.

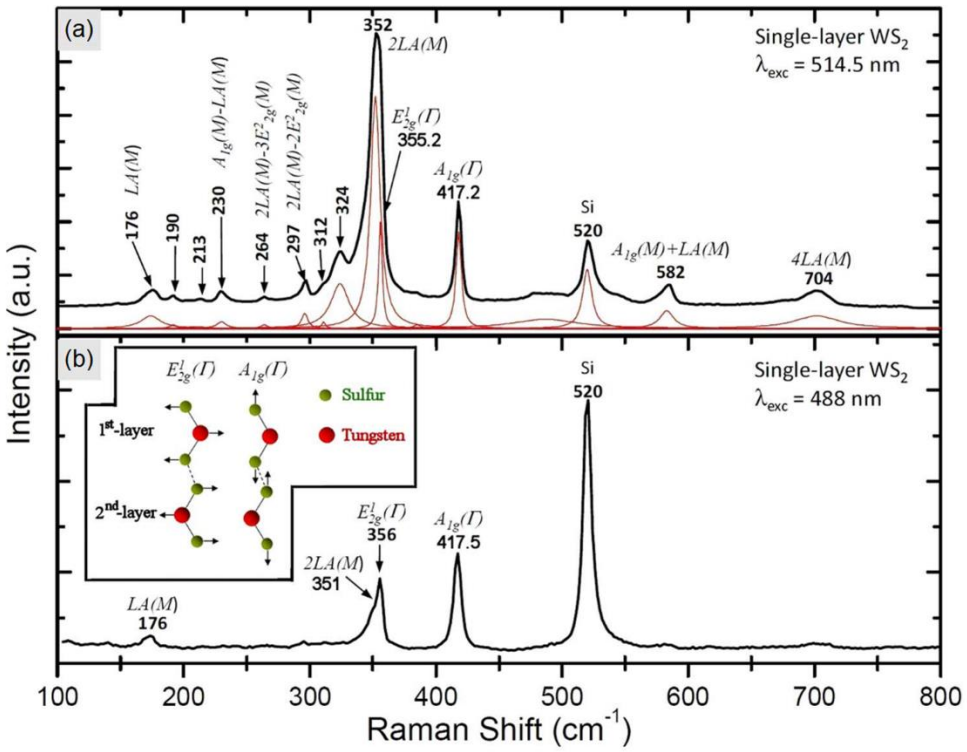

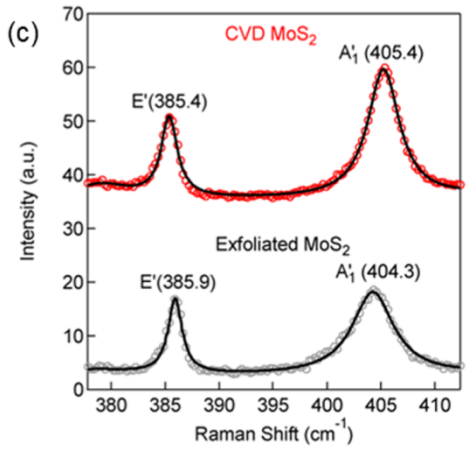

Figure 1.5 (a) and (b): A typical Raman spectrum of monolayer WS_2. Spectra were obtained using an excitation wavelength of (a): 514.5 nm and (b): 488 nm, respectively. The inset shows a schematic of the vibration mode and crystal structure of WS_2 [16]; (c): A typical Raman spectrum of CVD (chemical vapor deposition)-grown and exfoliated monolayer MoS_2 [17].

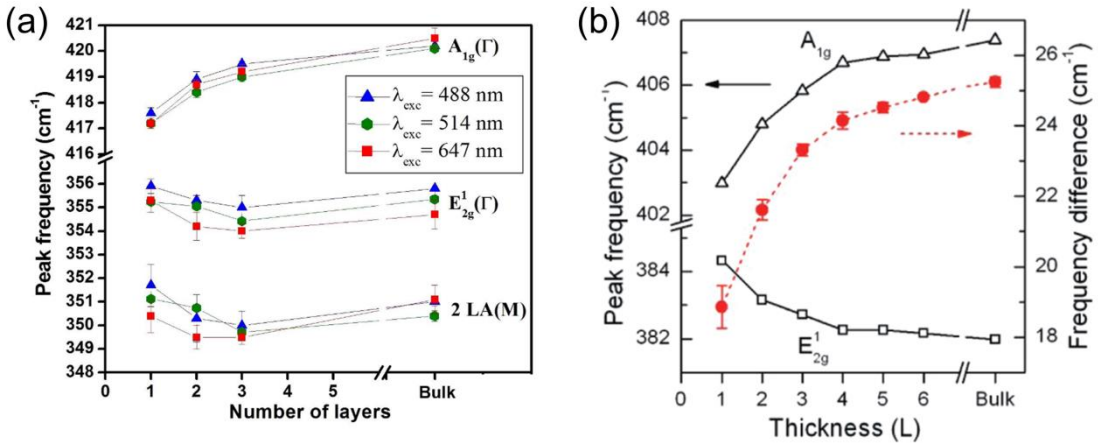

Figure 1.6. A typical Raman spectrum and layer number dependence of (a):WS_2 [16] and (b):MoS_2 [15].

As shown in Figure 1.6, the Raman peak position is dependent on the layer number. This change in peak position is caused by interlayer vdW interaction and dielectric screening of the long-range Coulombic interactions between the effective charges. With increasing layer number, the A'_1 mode exhibits a large blue shift, whereas the E′ modes are red-shifted [18].

In addition, the spectra of multilayered TMDC show additional peaks in the very-low-frequency region [19,20]. These peaks are referred to as the shear mode (SM) and layer-breathing mode (LBM). Corresponding schematics of the vibration mode are shown in Figure 1.7.

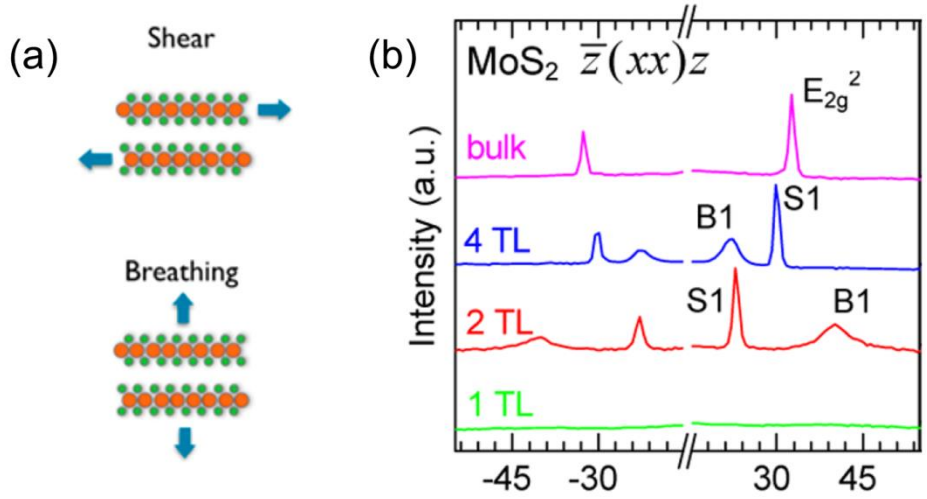

Figure 1.7. (a) :A schematic of SM and LBM [21]; (b): Layer number dependence of low-frequency Raman spectrum MoS_2.with parallel configuration. S1 and B1 correspond to SM and LBM, respectively [19].

These features are observed only in the spectra of multilayered TMDC because two or more layers are required to vibrate. The appearance of these spectral features, therefore, indicates the condition of stacking. The appearance of these peaks requires strong coupling of layers and, therefore, means that the interface of the atomic layers is clean [22]. The LBM is caused by a change in the interlayer distance; the corresponding peaks appear when two or more layers are stacked, and the appearance of peaks is not strongly affected the effect of the stacking angle and lattice mismatch. By contrast, the occurrence of the SM requires lateral lattice matching between layers. Thus, the appearance of SM peaks indicates that the lattice constant of the layers and

crystallographic orientation of them is matched or near to match [22-24].

1.4.2. PL properties of TMDC

TMDC have been attracted a great deal of interest not only for their electrical properties but also for their unique optical properties, which include a strong excitonic effect. Monolayer TMDC show PL emission from A excitons around 1.6–2.0 eV [10,25-27].

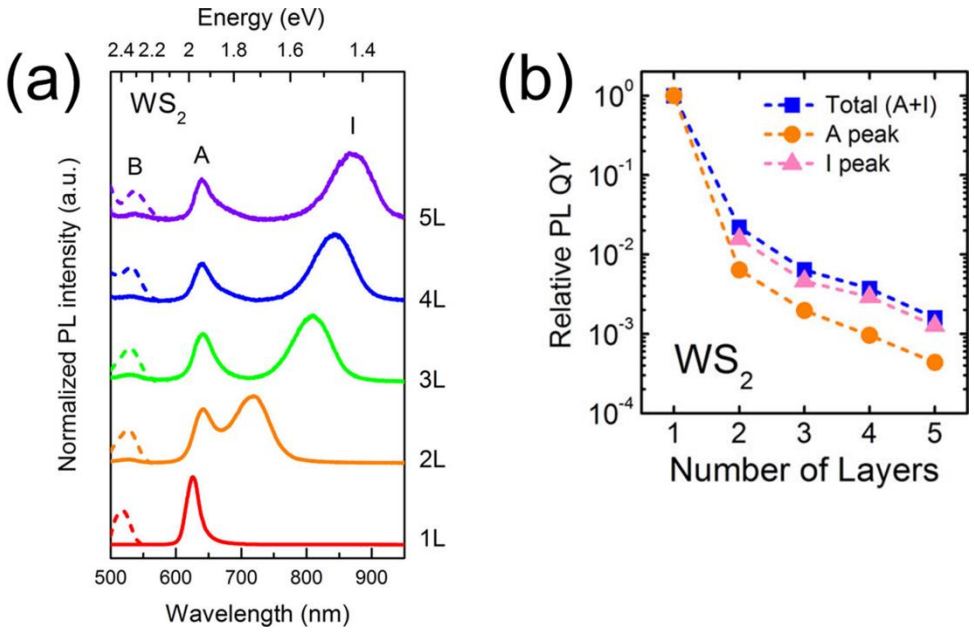

Figure 1.8. Layer-number dependence of (a): the normalized PL spectrum and (b): the PL quantum yield (QY) in mechanically exfoliated WS_2. A, B and I correspond to the PL emission from A, B-exciton and indirect transition [26].

In the case of TMDC, the many-body effect is prominent, and the excitonic effect dominates their optical transition because of their reduced dimensions and screening effects. The binding energy of excitons in TMDC reaches several hundreds of meV [28-30]. This value is much larger than the thermal energy at room temperature

($k_BT \approx 26$ meV, where k_B and T are the Boltzmann constant and temperature, respectively) and the binding energy of excitons in 3D materials such as Si (14.7 meV) [31]. Consequently, TMDC exhibit PL emission from excitons even at room temperature. And as previously mentioned, monolayer TMDC are direct-gap semiconductors, whereas multilayer TMDC are indirect-gap semiconductors. This property causes monolayer TMDC to exhibit more intense PL emission than their multilayer counterparts (Figure 1.8) [5,26]. And not only direct transition, multilayered TMDC show indirect peaks (Figure 1.8(a)).

TMDC show PL emissions from trions at room temperature (Figure 1.9). A trion is a charged exciton such as an electron–electron–hole or an electron–hole–hole pair. In the case of MoS_2 and WS_2, negatively charged trions are observed. Their binding energy reaches several tens of meV, and PL emissions are observed from trions even at room temperature [12]. In addition, their PL intensity can be modified through carrier doping [32].

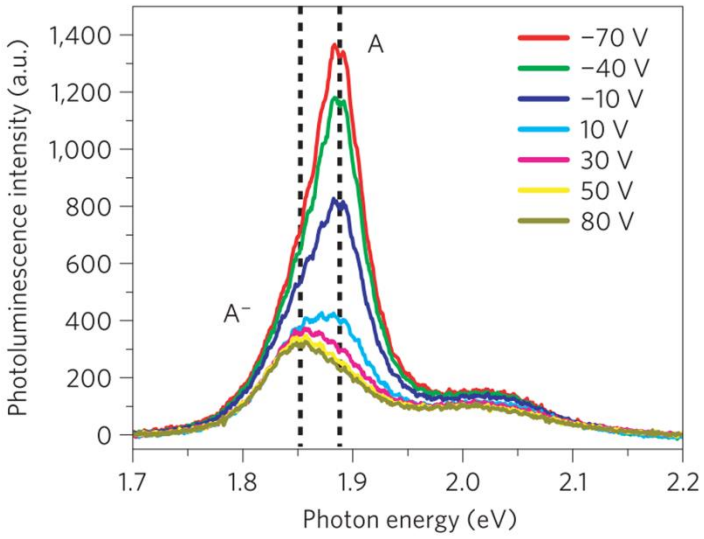

Figure 1.9. PL spectra at different back-gate voltages in MoS_2. A and A^- correspond to a neutral exciton and a trion, respectively [12].

Stabilizing excitonic states represents a new field for exploring basic optical physics. The high binding energies of excitons and trions mean that additional higher-order excitonic states can be stabilized and observed in TMDC. For example, a biexciton, which is a complex of two excitons, has been observed in both WS_2 and WSe_2 [33-35]. The binding energy of a biexciton in 2D and quantum well system is predicted to be proportional to that of an exciton and to the ratio of effective mass between electrons and holes [36-38]. Thus, due to the large binding energy of excitons, biexcitonic states are also stabilized and observed in TMDC. These possibilities and phenomena are important for exploring fundamental quantum mechanics.

As shown in Figure 1.3, TMDC with odd numbers of layers have inequivalent valleys at the K and K′ points. Photocarriers can be selectively excited at the K or K′ point using circularly polarized light [2,4,39]. Figure 1.10 shows the PL spectra of monolayer WS_2 under circularly polarized light.

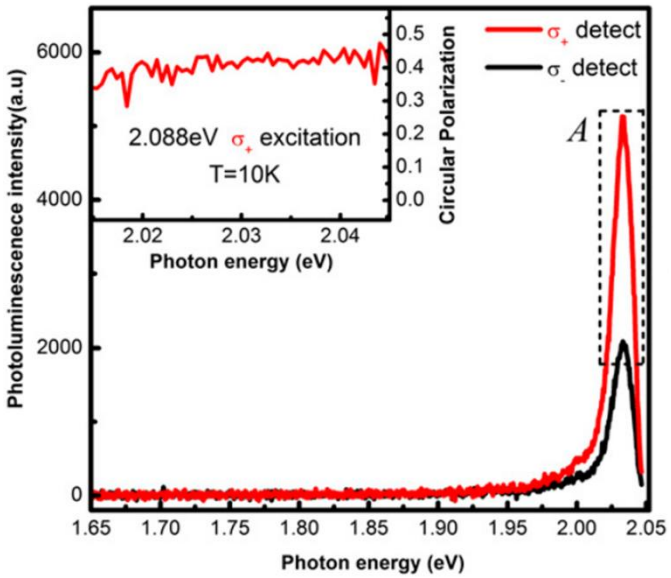

Figure 1.10. PL spectra excitation by circular-polarized light and an excitation energy of 2.088 eV at 10 K. Red and black line denote co-circular (σ+) and contra circular (σ−) detection with

excitation. Inset shows the calculated value of *P* at the PL peak [40].

Valley-polarized excitons can thus be created at the K or K′ point. Polarization *P* is given by the following equation:

$$\mathrm{P} = \frac{I(\sigma+) - I(\sigma-)}{I(\sigma+) + I(\sigma-)} \quad (1.1)$$

where $I(\sigma+)$ and $I(\sigma-)$ are the intensity of each peak that exhibits co-circular and contra-circular polarization with excitation, respectively. Valley-polarized excitons can be delocalized through an exchange interaction, and their lifetime is approximately 6 ps at 4 K in WSe_2 [41,42].

1.5. Growth methods of TMDC

Numerous methods have been developed to prepare monolayer TMDC and other 2D materials [1,9,43-46]. They are usually prepared by one of two main methods: mechanical exfoliation and chemical vapor deposition (CVD). Typically, 2D materials obtained by mechanical exfoliation are highly crystalline, with a small domain size. By contrast, the CVD method enables the large-scale preparation of monolayer 2D materials; however, the materials' quality is relatively poor [47,48]. Several attempts to overcome the disadvantages of these methods have been reported. For example, to improve the grain size of the exfoliation method, the use of gold as a new adhesion layer is effective. Using this method, large grain sizes (as large as 500 μm) have been achieved [49].

1.5.1. Mechanical exfoliation

The mechanical exfoliation method is commonly used for obtaining thin flakes of 2D materials [1,15,16]. This method is a very simple yet efficient approach to obtaining high-quality small crystals that are still sufficiently large to allow characterization of their properties. The typical mechanical exfoliation procedure includes 1) adhering bulk 2D crystals onto a piece of adhesive (e.g., Scotch® tape); 2) stacking adhesive layers of tapes and then peeling them off; 3) repeating step 2 10–20 times; 4) placing the tape with exfoliated crystals onto a substrate such as an oxidized surface, a heavily doped silicon substrate (SiO_2/Si), or sapphire; and 5) peeling off the tape. Exfoliated 2D crystals with various thicknesses and sizes are thus obtained, the researcher have to select individual crystals for experiments. An optical image of a typical monolayer WSe_2 that was obtained by the exfoliation method is shown in Figure 1.11.

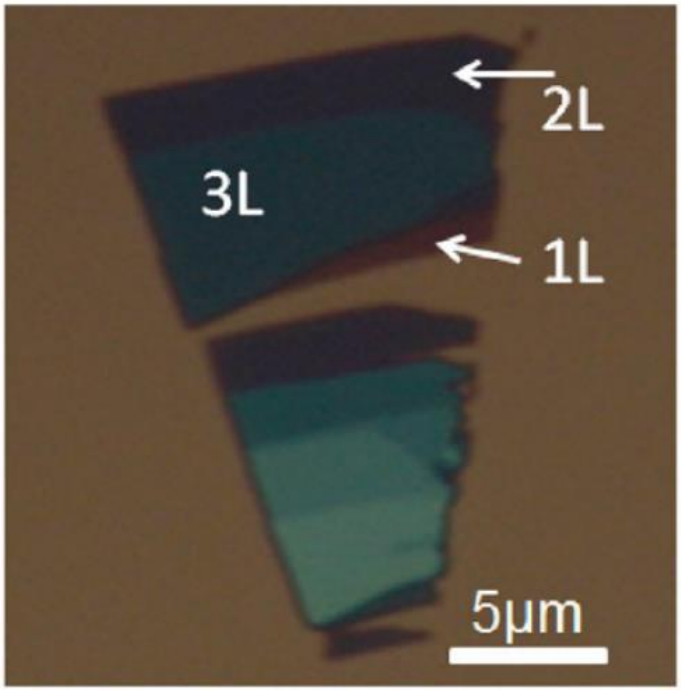

Figure 1.11. Optical image of exfoliated WSe_2 on an SiO_2/Si substrate [50].

The advantage of the mechanical exfoliation method is that we can obtain high-quality samples from crystals obtained by the high-pressure and high-temperature (HPHT) or chemical vapor transfer method [51]. In addition, high-quality samples can be obtained at an extremely low cost. The disadvantage of this method is that it does not enable control of the layer number and size. Such control requires the CVD or molecular beam epitaxy growth method.

1.5.2. The CVD method

The CVD method is also commonly used to obtain large-scale, monolayer 2D materials [44,52,53]. Because a substrate with a catalytic effect is not required to grow them, TMDC can be grown on various substrates that are selected on the basis of properties the investigator intends to measure. The literature contains numerous reports of successful growth of TMDC on substrates such as SiO_2/Si, sapphire, hBN, and graphite [44,54-56]. Typical precursors to grow MoS_2 and WS_2 are a metal oxide (MoO_3 or WO_3) and elemental sulfur [54,57,58]. The precursors are evaporated by an electric furnace and deposited onto a substrate, and various TMDC can be deposited using this approach. The number of layers and the grain size can be controlled through variation of the CVD growth conditions. In fact, sub-millimeter-sized MoS_2 monolayers have been grown using this method [44]. Figure 1.12 (a) shows a typical optical image of MoS_2 grown on SiO_2/Si substrate.

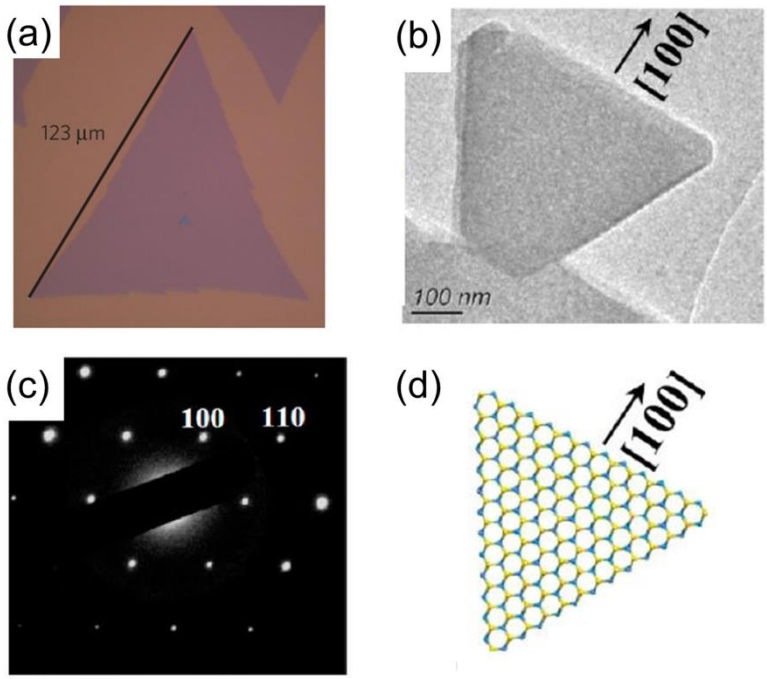

Figure 1.12. (a): Typical optical image of CVD-grown MoS_2 on an SiO_2/Si substrate [44]; (b): A TEM image, (c): electron-diffraction pattern, and (d): the corresponding schematic image of a single domain, triangular crystal of WS_2. Edges of crystals are perpendicular to the [100] direction (zig-zag edges) [25].

Numerous other precursors can be used to grow TMDC. For example, metal chlorides can be used as a metal source. Because the melting points of metal chlorides are lower than those of the corresponding metal oxides, they are more easily supplied than metal oxides. In addition, metal chlorides have also been used to grow MoS_2, NbS_2, and WS_2 [45,55,59].

CVD-grown TMDC are typically triangular crystals. The formation of triangular-shaped TMDC crystals can be explained by appearance of the zig-zag edge, which is an energetically preferred edge (Figure 1.12 (b), (c), and (d)) [25,44,60]. When a zig-zag sulfur or metal edge is assumed, the shape of crystal is uniquely determined as triangular. In many previous reports about the CVD growth of monolayer TMDC on

various substrates such as SiO_2/Si, sapphire, and graphite, the formation of triangular-shaped crystals has also been observed [44,54,56].

1.6. hBN

hBN is a 2D material composed of boron and nitrogen. Figure 1.13 shows the crystal structure of hBN. Its structure is similar to and isoelectronic with that of graphite [61,62]. However, the band structure of hBN differs substantially from that of graphite: hBN is an insulator, and the bandgap of hBN is approximately 5.97 eV [7].

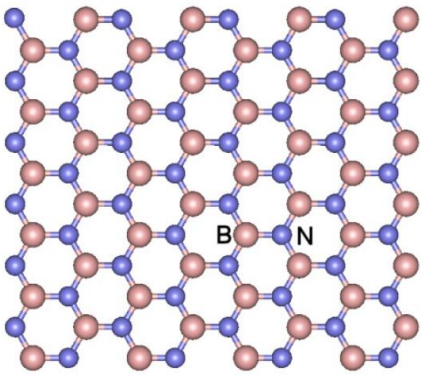

Figure 1.13 A schematic image of hBN layer [63].

hBN can be obtained by the HPHT method or the CVD method [64,65]. HPHT method tends to result in high-quality hBN that is, however, obtained as bulk crystals. HPHT hBN is commonly used as a substrate or as a protection layer (see Section 1.7.4) in conjunction with the mechanical exfoliation method because hBN is an ideal protection layer and substrate in that it is an atomic layered insulator without dangling bonds, surface roughness, or charged impurities on its surface [66]. We will introduce this at chapter 1.7.4.

1.7. van der Waals heterostructures of 2D materials

In 2D materials, the layers are bonded not by chemical bonding but by vdW interaction. Thus, a 2D material can be peeled off and stacked onto other 2D materials. The resultant structures are called vdW heterostructures (Figure 1.14).

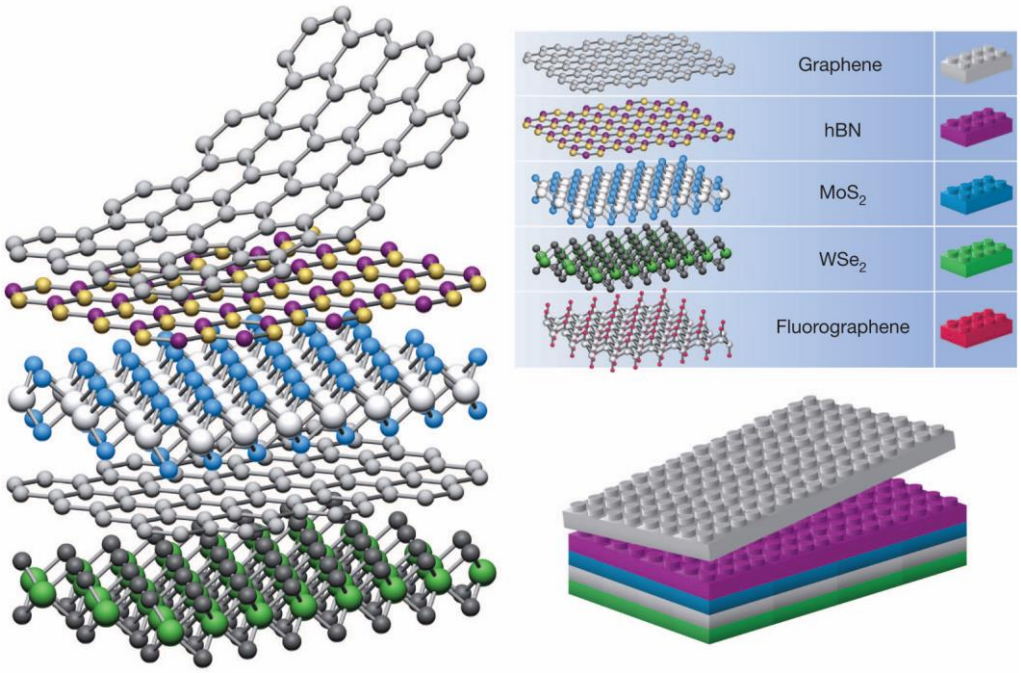

Figure 1.14. A schematic of van der Waals heterostructures [67].

Three-dimensional (3D) stacked heterostructures have already been achieved using a molecular beam epitaxy system; however, its ability to fabricate such structures is limited. Because 3D materials have chemical bonds between layers, to form high-quality interface, lattice matching of materials is needed. By contrast, 2D materials circumvent this problem. As previously noted, 2D materials have no chemical bonds between layers; thus, limitations related to lattice constants, crystal structures, and

stacking angles are not encountered. Consequently, various 2D vdW heterostructures with different components, properties, and structures can be assembled. In the current study, we focused on the growth, fabrication, and optical properties of WS_2-, MoS_2-, and hBN-based vdW heterostructures. We first survey the electrical and optical properties of WS_2 and MoS_2 vdW heterostructures (i.e., WS_2/MoS_2) and then discuss the effect of hBN as a substrate and protection layer.

1.7.1. Band structure of WS_2/MoS_2 vdW heterostructures

Figure 1.15 shows the band structure of WS_2/MoS_2 with a stacking angle of 60°, as obtained by density function theory (DFT) calculations.

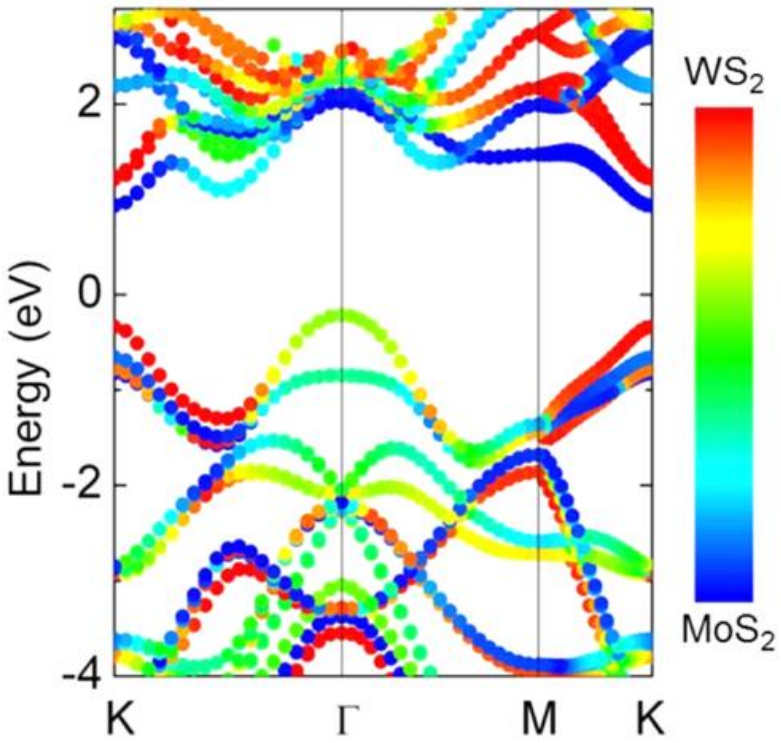

Figure 1.15. Band structure of WS_2/MoS_2 heterostructures obtained by DFT calculations. The color scale corresponds to the contributions of different layers [68].

WS_2 and MoS_2 heterostructures exhibit type-II band alignment at K point and are indirect semiconductors [69-72]. This band structure changes with variations in the stacking angle [73,74]. Figure 1.16 shows the stacking-angle dependence of the band structure of WS_2/MoS_2. As shown in the figure, the band structure of WS_2/MoS_2 varies with the stacking angle, which means that the optical responses also vary with the stacking angle. We will discuss this phenomenon in Section 1.7.2.

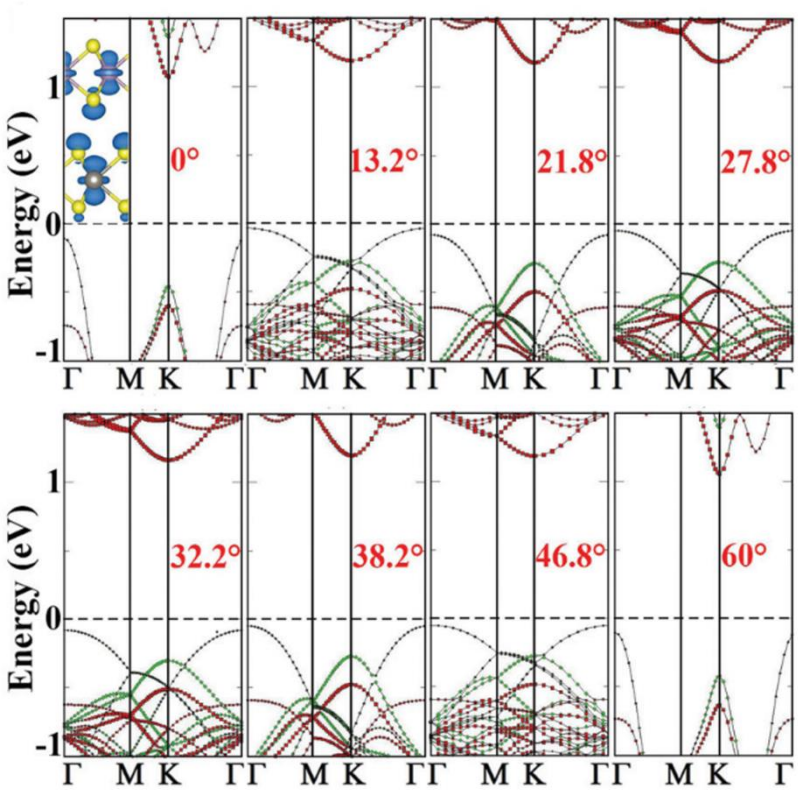

Figure 1.16. Stacking angle dependence of band structure of WS_2/MoS_2 [73].

1.7.2. Optical properties of 2D vdW heterostructures

As with the Raman spectra of multilayered TMDC, the Raman spectra of

TMDC-based vdW heterostructures show the same vibrational modes observed in the spectra of the corresponding TMDC monolayers. Figure 1.17 shows typical Raman spectra of WS_2/MoS_2 heterostructures and their dependence on the fabrication method.

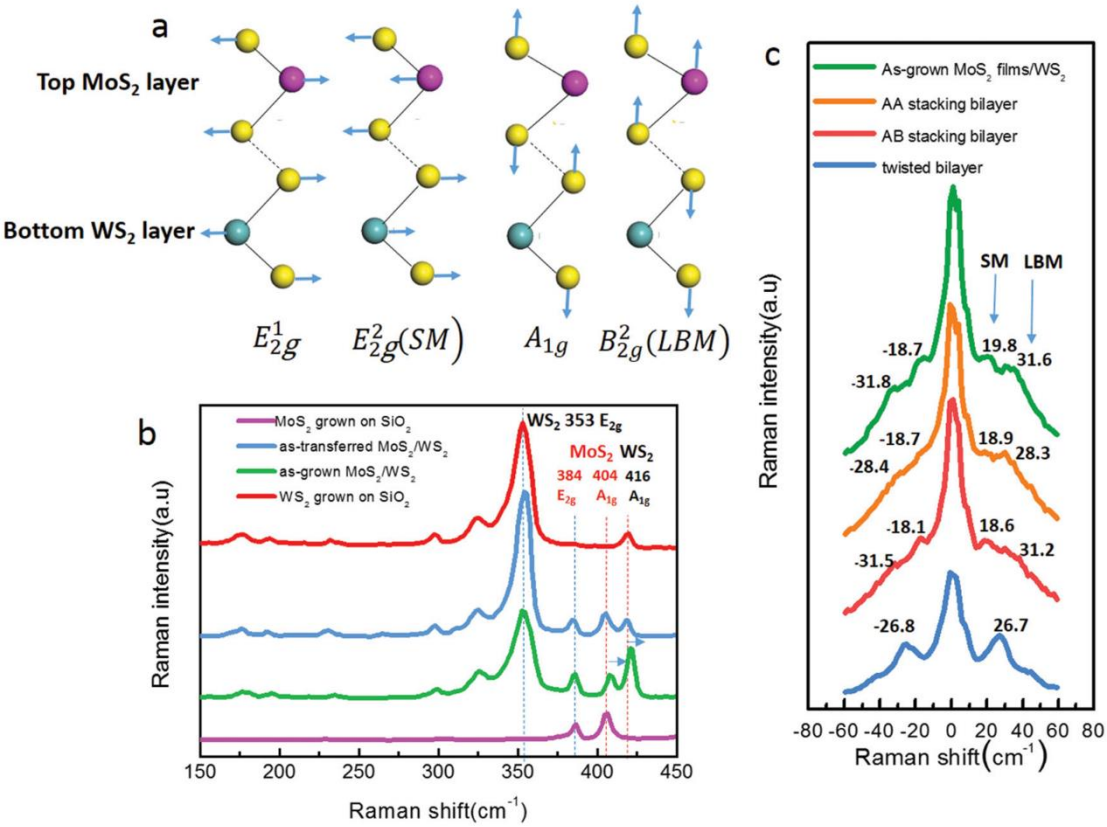

Figure 1.17. Raman spectra of WS_2/MoS_2 heterostructures with various fabrication methods. (a): A schematic of the lattice structure and the vibrational mode for a WS_2/MoS_2 heterostructures; (b): Raman spectra at high frequency region of as-grown monolayer WS_2, MoS_2, and MoS_2/WS_2 heterostructures fabricated by a direct CVD growth and a transfer method; (c): Raman spectra at low-frequency region of the SM and the LBM for CVD-grown MoS_2/WS_2 heterostructures with AA and AB stacked, and twisted stacked heterostructures fabricated by a transfer method [23].

As shown in Figures 1.17(a) and 1.17(b), the high-frequency region of the Raman spectrum of the MoS_2/WS_2 heterostructure consists of the combined spectral features of

WS_2 and MoS_2. Peak shifts occurred as a result of interlayer coupling [23], then A'_1 modes are red shifted especially in CVD grown samples, where interlayer coupling is strong (Figure 1.17 (b)).

In the low-frequency region, the SM and the LBM are not only observed in the spectrum of the multilayered TMDC but also in the spectrum of the heterostructure. Like the low frequency Raman spectrum of a multilayered TMDC, that of a WS_2/MoS_2 heterostructure with AA or AB stacking shows both the SM and the LBM, whereas the spectrum of the twisted heterostructures shows only the LBM in the low-frequency region (Figures 1.17(a) and 1.17(c)). In addition, the appearance of these peaks indicates that the interface between the layers is clean [22].

Two-dimensional heterostructures with type-II band alignment, such as WS_2/MoS_2 or $MoSe_2/WSe_2$ vdW heterostructures, exhibit PL emission from interlayer excitons [75,76]. When a photon is absorbed in MoS_2 or WS_2, a photocarrier can transfer from one layer to another, resulting in an interlayer exciton (Figure 1.18).

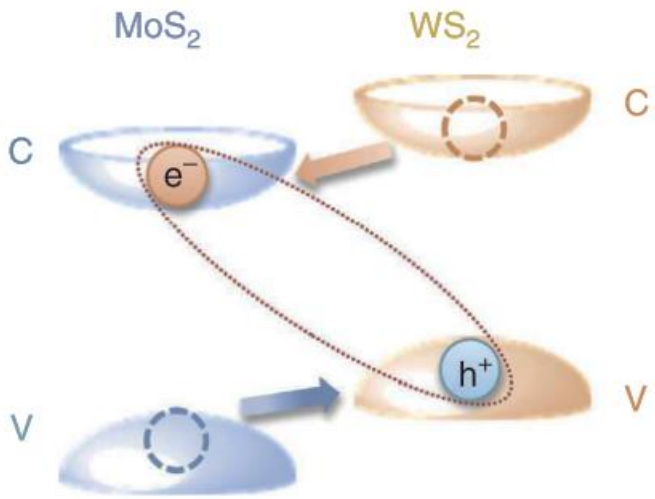

Figure 1.18. A schematic of the band alignment of a MoS_2/WS_2 heterostructure. C and V correspond to the conduction-band bottom and valence-band top, respectively [77].

In the case of a WS_2/MoS_2 heterostructure, electrons and holes are located in the MoS_2 and WS_2 layers, respectively. These species in $WSe_2/MoSe_2$ exhibit a longer lifetime of approximately 138 ns at 4.5 K [78] because the electrons and holes are spatially separated, and they show a very long valley lifetime of approximately 40 ns at 30 K [79]. These lifetimes are much longer than those in monolayer TMDC [42,80,81]. These results strongly indicate that 2D vdW heterostructures are excellent materials for exploring valleytronics.

In addition, because TMDC vdW heterostructures are a multivalley system, numerous valleys are available to serve as points of origin of interlayer excitons. For example, the K, Q, and Γ points can contribute to the formation of interlayer excitons in in TMDC-based heterostructures [68,74,82]. Because these interlayer excitons have different origins, they should exhibit different optical responses. In a previous report, PL peaks in a WS_2/MoS_2 heterostructure were suggested to originate from interlayer excitons corresponding to K–K and K–Γ transitions [83]; however, further spectroscopic characterization and theoretical analyses are needed to fully elucidate the origin of the PL emissions.

As previously discussed, the band structure of TMDC-based heterostructures can be modulated by their stacking angle. Thus, optical responses of interlayer excitons can also be varied by changing the stacking angle. Figure 1.19 shows the stacking-angle dependence of light cones in $MoSe_2/WSe_2$ and MoS_2/WSe_2 heterostructures [84].

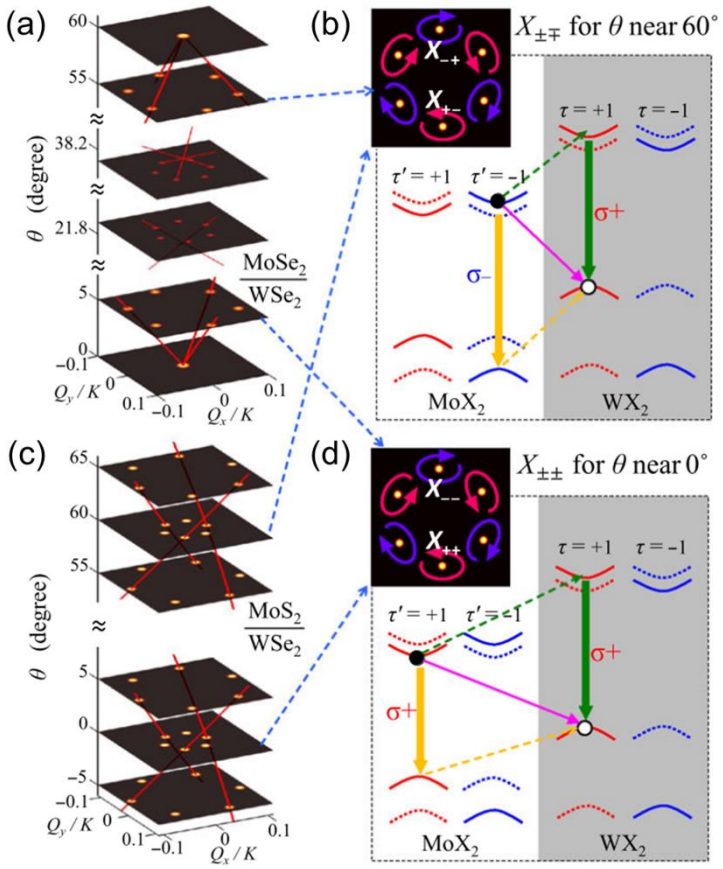

Figure 1.19. Calculated light cones of (a): $MoSe_2/WSe_2$ and (c): MoS_2/WSe_2 heterostructures at K point. Thick and thin red line shows the evolution of main and second Umklapp light cones, respectively; (b) and (d); The corresponding optical transitions and polarization. Inset shows the elliptical polarization of PL emission at the main light cones. Solid and dashed allows denote the dipole transition and interlayer hopping. These are obtained by DFT calculations.[84]

Figure 1.19 shows that the optical transition from a K point to a K or K´ point should be suppressed without a stacking angle of approximately 0° or 60°. But in the case of $MoSe_2/WSe_2$ system, second Umklapp light cones would also appear at lowest energy in the stacking angle of 21.8° or 38.2° (Figure 1.19(a)), but this have small dipole strength. Then, their PL is weaker rather than stacking angle of 0° or 60°. Figure 1.20 shows the stacking-angle dependence of the optical transition energy between K–K (direct) and K–Γ (indirect) transitions in a WS_2/MoS_2 heterostructure. The energies of

these transitions are strongly dependent on the stacking angle, especially at a stacking angle of 0° or 60°. Thus, to measure their physical properties and estimate the origin of the interlayer excitons, controlling the stacking angle is indispensable.

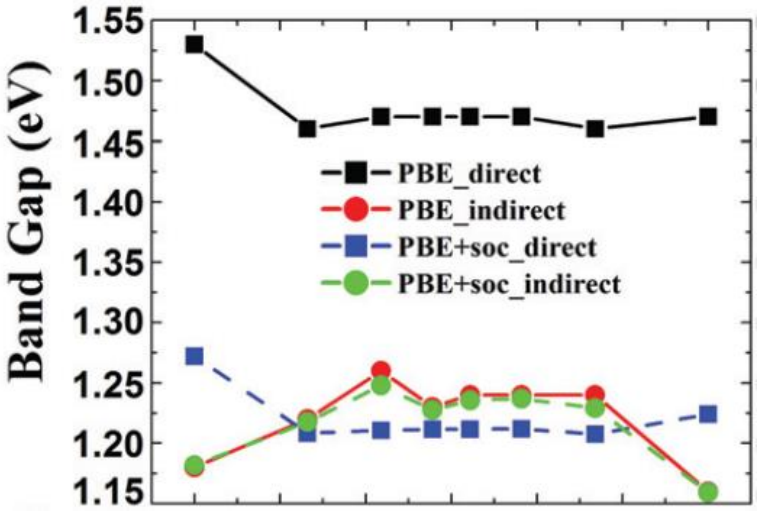

Figure 1.20. Stacking-angle dependence of the optical transition energy between K–K (direct) and K–Γ (indirect) transitions in WS_2/MoS_2 heterostructures, as obtained by DFT calculations [73].

1.7.3. Fabrication method of van der Waals heterostructures

The polymer-assisted dry transfer method is commonly used to fabricate vdW heterostructures. Because no chemical bonds exist between layers, heterostructures can be fabricated via manual stacking of sheets. Using optical microscope and three axis micrometer stage with a polymer such as polydimethylsiloxane (PDMS) and some other polymers (e.g., polypropylene carbonate (PPC) or polymethyl methacrylate (PMMA)), heterostructures can be fabricated by like a “stamping” [85-87]. Figure 1.21 shows a schematic of the typical setup and diagram of the fabricating heterostructures by dry transfer method.

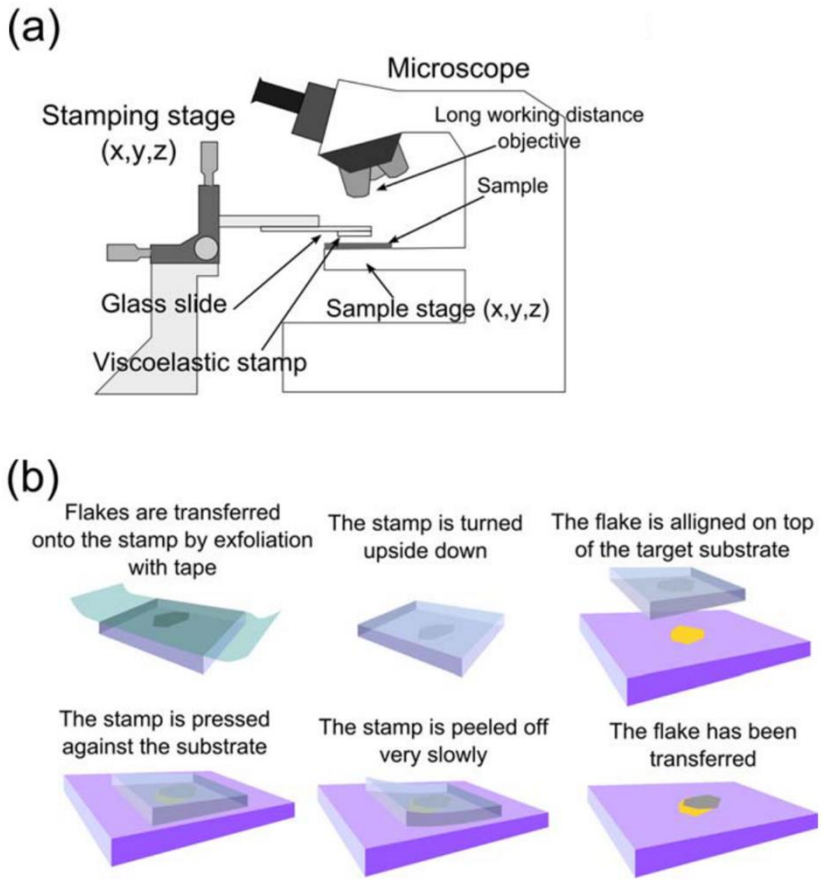

Figure 1.21. (a): A schematic of the dry-transfer setup; (b): diagram of the steps involved in dry transfer [87].

Optical images of typical fabricated heterostructures are shown in Figure 1.22.

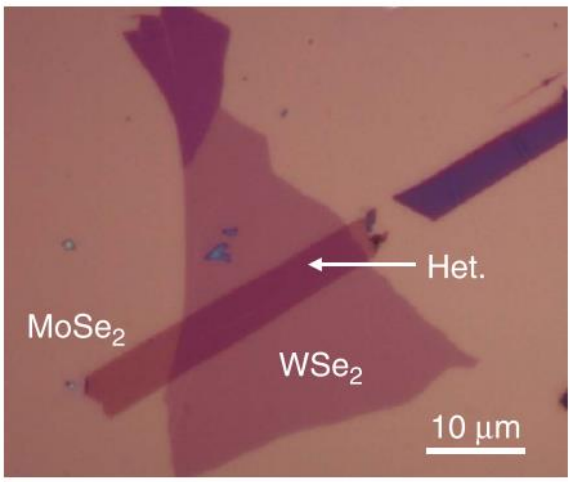

Figure 1.22. Optical image of an $MoSe_2/WSe_2$ heterostructure prepared by the dry-transfer method [88].

The advantage of this method is that various 2D materials can be stacked with control of their position and stacking angle. In addition, no solvent is used in all dry transfer method with exfoliated samples. The interface between layers is, therefore, free of bubbles and residues [86]. The use of a solvent results in residues between the layers, which can adversely affect a heterostructure's intrinsic properties [22]. The disadvantage of this method is that the crystallographic orientation of exfoliated samples is difficult to estimate, which makes the crystallographic orientation of the samples difficult to control. One reported solution to this problem involves using second-harmonic-generation microscopy to estimate the crystallographic orientation of exfoliated samples [79,88].

The literature also contains numerous reports of the direct CVD growth of heterostructures [76,89]. Typically, CVD-grown TMDC show a stacking angle of 0° (AA stacking) or 60° (AB stacking) because the second layer is grown epitaxially on the first layer [23].

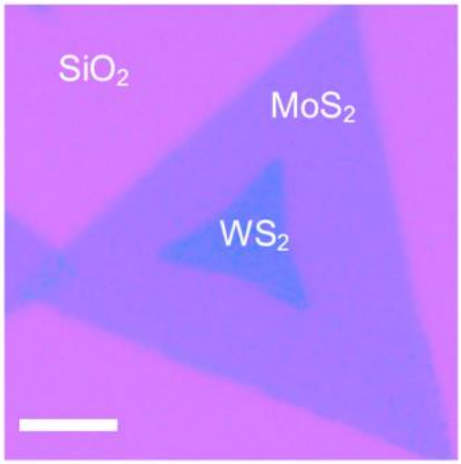

Figure 1.23. Optical image of a typical CVD-grown WS_2/MoS_2 heterostructure on SiO_2/Si substrate. Scale bar: 10 μm [90].

In addition, numerous accounts of fabricating vdW heterostructures by transferring CVD-grown TMDC samples have been reported [22,68,91]. One of the merits of these fabrication methods is that the stacking angle is easily controlled because the crystallographic orientation of the components is easily estimated from the shape of the crystals [44]. As previously noted, CVD-grown TMDC crystals typically exhibit a triangular shape with a zig-zag edge appearance. Their crystallographic orientation is easily estimated by optical microscopy, enabling the fabrication of heterostructures with controlled stacking angles. The weak point of this method which commonly reported is residues. In these reports, when CVD is used to grow samples for the dry-transfer method, a wet-transfer method is typically used to detach the TMDC samples from the grown substrate [68,92]. This method results in a dirty interface between layers, and sometimes prohibits their intrinsic properties [22].

1.7.4. Using hBN as a substrate and a protection layer

One of the largest problems encountered in investigations of the properties and potential applications of 2D materials is environmental effects. In the case of 2D materials, almost all atoms are located at the surface. Consequently, the materials' properties change in response to their environment, such as the substrate they are deposited on or surrounding gases that adsorb onto their surface [93,94]. For example, the carrier mobility of graphene is limited by surface roughness, charged dangling bonds, optical phonons, and charged impurities on SiO_2/Si substrates [94]. To mitigate

such environmental effects, hBN have commonly been used as a substrate and as a protection layer [86,95,96]. As previously noted, hBN is also a 2D material and an insulator without surface roughness, charged impurities, or low-energy optical phonons. These properties make hBN an ideal substrate and protection layer. Thus, when encapsulated by hBN, or using hBN as a substrate, samples are free from these environmental effects.

Figure 1.24 shows an optical image, an atomic force microscopy (AFM) image, and a cross-sectional transmission electron microscopy (TEM) image of hBN-sandwiched graphene (hBN/graphene/hBN). As shown in Figures 1.24(b) and 1.24(c), the fabricated heterostructure exhibits a clean interface between the graphene and the hBN. The carrier mobility of hBN/graphene/hBN reaches 140,000 $cm^2/(V \cdot s)$, whereas that of graphene on SiO_2/Si substrates is limited to ~40,000 $cm^2/(V \cdot s)$ at room temperature [86,94]. This high carrier mobility is achieved because of the ability of hBN to reduce environmental effects. This approach can also be used with other 2D materials. For example, WS_2 grown on hBN shows a sharper PL emission (~23 meV), and MoS_2 grown on hBN shows a higher carrier mobility (~30 $cm^2/(V \cdot s)$) than those on SiO_2/Si substrates (42–68 meV and ~7 $cm^2/(V \cdot s)$, respectively) [25,97-99]. In addition, hBN encapsulation of TMDC is also key factor to reduce the substrate effect, leading to observation of their intrinsic properties like trion quantum beats and valley Landau levels [100,101]. These results indicate that using hBN as a substrate or protection layer is essential for exploring the possibilities of 2D materials.

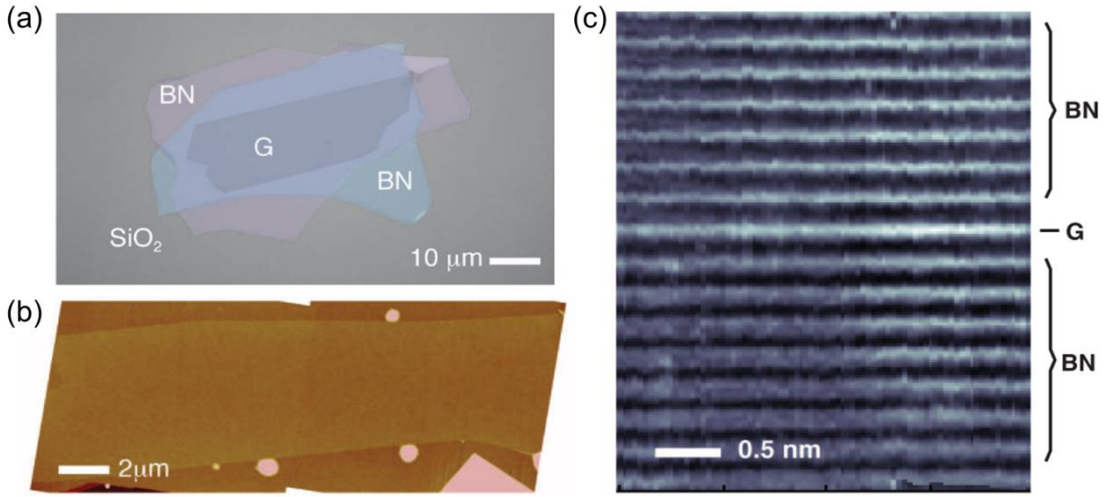

Figure 1.24. (a): An optical image and (b): an AFM image of fabricated hBN/graphene/hBN heterostructures as well as (c): a cross-sectional TEM image of the sample shown in (b) [86].

1.8. Research overview

As post-silicon materials and a new field for exploring quantum mechanics in the 2D limit, TMDC and its vdW heterostructures are attracting intensive attention. To investigate these possibilities, high-quality samples are indispensable. To obtain such samples, we have focused on using hBN as a substrate and protection layer and on investigating the fundamental PL properties of monolayer WS_2 and WS_2/MoS_2 vdW heterostructures.

In Chapter 2, we report a direct CVD method for growing WS_2 on exfoliated hBN substrates. We successfully synthesized WS_2 directly on hBN (WS_2/hBN) using a multifurnace CVD method. The grown WS_2 shows a very sharp and strong PL emission compared with WS_2 grown on SiO_2/Si and sapphire substrates. This sharp and strong PL emission strongly indicates that our WS_2 sample is a high-quality monolayer.

In Chapter 3, we report biexcitonic emission from WS_2 grown on hBN. In this chapter, we discuss the characteristics of biexcitonic PL emission from WS_2/hBN.

Biexcitonic emission from WS_2/hBN was achieved at an extremely low excitation power, which suggests that our sample has sufficiently high quality to enable exploration of fundamental physics in two dimensions.

In Chapter 4, we report the fabrication and optical properties of hBN-encapsulated WS_2/MoS_2 heterostructures (i.e., hBN/WS_2/MoS_2/hBN). In this chapter, we describe a new and simple method of fabricating hBN-encapsulated WS_2/MoS_2 heterostructures with controlled stacking angles. By using this sample, we report the identification of three interlayer excitons in these heterostructures through detailed PL measurements and DFT calculations.

1.9. References

[1] K. S. Novoselov, A. K. Geim, S. V. Morozov, D. Jiang, Y. Zhang, S. V. Dubonos, I. V. Grigorieva and A. A. Firsov, ***Science***, 306, 666-669, (2004).

[2] K. F. Mak, K. L. McGill, J. Park and P. L. McEuen, ***Science***, 344, 1489-1492, (2014).

[3] Y. Shimazaki, M. Yamamoto, I. V. Borzenets, K. Watanabe, T. Taniguchi and S. Tarucha, ***Nat. Phys.***, 11, 1032, (2015).

[4] D. Xiao, G.-B. Liu, W. Feng, X. Xu and W. Yao, ***Phys. Rev. Lett.***, 108, 196802, (2012).

[5] K. F. Mak, C. Lee, J. Hone, J. Shan and T. F. Heinz, ***Phys. Rev. Lett.***, 105, 136805, (2010).

[6] K. I. Bolotin, K. J. Sikes, Z. Jiang, M. Klima, G. Fudenberg, J. Hone, P. Kim and H. L. Stormer, ***Solid State Commun.***, 146, 351-355, (2008).

[7] K. Watanabe, T. Taniguchi and H. Kanda, ***Nat. Mater.***, 3, 404-409, (2004).

[8] A. Kumar and P. K. Ahluwalia, ***Eur. Phys. J. B***, 85, 186, (2012).

[9] G. Eda, H. Yamaguchi, D. Voiry, T. Fujita, M. Chen and M. Chhowalla, ***Nano Lett.***, 11, 5111-5116, (2011).

[10] A. Splendiani, L. Sun, Y. Zhang, T. Li, J. Kim, C. Y. Chim, G. Galli and F. Wang, ***Nano Lett.***, 10, 1271-1275, (2010).

[11] B. Radisavljevic, A. Radenovic, J. Brivio, V. Giacometti and A. Kis, ***Nat. Nanotechnol.***, 6, 147-150, (2011).

[12] K. F. Mak, K. He, C. Lee, G. H. Lee, J. Hone, T. F. Heinz and J. Shan, ***Nat. Mater.***, 12, 207-211, (2013).

[13] A. Kuc, N. Zibouche and T. Heine, ***Phys. Rev. B***, 83, 245213, (2011).

[14] H. Terrones, E. Del Corro, S. Feng, J. M. Poumirol, D. Rhodes, D. Smirnov, N. R. Pradhan, Z. Lin, M. A. Nguyen, A. L. Elias, T. E. Mallouk, L. Balicas, M. A. Pimenta and M. Terrones, ***Sci. Rep.***, 4, 4215, (2014).

[15] C. Lee, H. Yan, L. E. Brus, T. F. Heinz, J. Hone and S. Ryu, ***ACS Nano***, 4, 2695-2700, (2010).

[16] A. Berkdemir, H. R. Gutiérrez, A. R. Botello-Méndez, N. Perea-López, A. L. Elías, C.-I. Chia, B. Wang, V. H. Crespi, F. López-Urías, J.-C. Charlier, H. Terrones and M. Terrones, ***Sci. Rep.***, 3, 1755, (2013).

[17] D. Dumcenco, D. Ovchinnikov, K. Marinov, P. Lazić, M. Gibertini, N. Marzari, O. L. Sanchez, Y.-C. Kung, D. Krasnozhon, M.-W. Chen, S. Bertolazzi, P. Gillet, A. Fontcuberta i Morral, A. Radenovic and A. Kis, ***ACS Nano***, 9, 4611-4620, (2015).

[18] H. Li, Q. Zhang, C. C. R. Yap, B. K. Tay, T. H. T. Edwin, A. Olivier and D. Baillargeat, ***Adv. Funct. Mater.***, 22, 1385-1390, (2012).

[19] Y. Zhao, X. Luo, H. Li, J. Zhang, P. T. Araujo, C. K. Gan, J. Wu, H. Zhang, S. Y. Quek, M. S. Dresselhaus and Q. Xiong, ***Nano Lett.***, 13, 1007-1015, (2013).

[20] H. Zeng, B. Zhu, K. Liu, J. Fan, X. Cui and Q. M. Zhang, ***Phys. Rev. B***, 86, 241301, (2012).

[21] S.-Y. Chen, C. Zheng, M. S. Fuhrer and J. Yan, ***Nano Lett.***, 15, 2526-2532, (2015).

[22] C. H. Lui, Z. Ye, C. Ji, K.-C. Chiu, C.-T. Chou, T. I. Andersen, C. Means-Shively, H. Anderson, J.-M. Wu, T. Kidd, Y.-H. Lee and R. He, ***Phys. Rev. B***, 91, 165403, (2015).

[23] J. Zhang, J. Wang, P. Chen, Y. Sun, S. Wu, Z. Jia, X. Lu, H. Yu, W. Chen, J. Zhu, G. Xie, R. Yang, D. Shi, X. Xu, J. Xiang, K. Liu and G. Zhang, ***Adv. Mater.***, 28, 1950-1956, (2016).

[24] A. A. Puretzky, L. Liang, X. Li, K. Xiao, B. G. Sumpter, V. Meunier and D. B. Geohegan, ***ACS Nano***, 10, 2736-2744, (2016).

[25] H. R. Gutiérrez, N. Perea-López, A. L. Elías, A. Berkdemir, B. Wang, R. Lv, F. López-Urías, V. H. Crespi, H. Terrones and M. Terrones, ***Nano Lett.***, 13, 3447-3454, (2012).

[26] W. Zhao, Z. Ghorannevis, L. Chu, M. Toh, C. Kloc, P.-H. Tan and G. Eda, ***ACS Nano***, 7, 791-797, (2012).

[27] S. Tongay, J. Zhou, C. Ataca, K. Lo, T. S. Matthews, J. Li, J. C. Grossman and J. Wu, ***Nano Lett.***, 12, 5576-5580, (2012).

[28] B. Zhu, X. Chen and X. Cui, ***Sci. Rep.***, 5, 9218, (2015).

[29] C. Zhang, A. Johnson, C. L. Hsu, L. J. Li and C. K. Shih, ***Nano Lett.***, 14, 2443-2447, (2014).

[30] K. He, N. Kumar, L. Zhao, Z. Wang, K. F. Mak, H. Zhao and J. Shan, ***Phys. Rev. Lett.***, 113, 026803, (2014).

[31] K. L. Shaklee and R. E. Nahory, ***Phys. Rev. Lett.***, 24, 942-945, (1970).

[32] J. S. Ross, S. Wu, H. Yu, N. J. Ghimire, A. M. Jones, G. Aivazian, J. Yan, D. G. Mandrus, D. Xiao, W. Yao and X. Xu, ***Nat. Commun.***, 4, 1474, (2013).

[33] Y. You, X.-X. Zhang, T. C. Berkelbach, M. S. Hybertsen, D. R. Reichman and T. F. Heinz, ***Nat. Phys.***, 11, 477-481, (2015).

[34] G. Plechinger, P. Nagler, J. Kraus, N. Paradiso, C. Strunk, C. Schüller and T. Korn, ***Phys. Status Solidi RRL***, 9, 457-461, (2015).

[35] J. Shang, X. Shen, C. Cong, N. Peimyoo, B. Cao, M. Eginligil and T. Yu, ***ACS***

Nano, 9, 647-655, (2015).

[36] D. A. Kleinman, ***Phys. Rev. B***, 28, 871-879, (1983).

[37] J. Singh, D. Birkedal, V. Lyssenko and J. M. Hvam, ***Phys. Rev. B***, 53, 15909, (1996).

[38] S.-Y. Shiau, M. Combescot and Y.-C. Chang, ***Ann. Phys.***, 336, 309-330, (2013).

[39] K. F. Mak, K. He, J. Shan and T. F. Heinz, ***Nat. Nanotechnol.***, 7, 494-498, (2012).

[40] B. Zhu, H. Zeng, J. Dai, Z. Gong and X. Cui, ***Proc. Natl. Acad. Sci. U. S. A.***, 111, 11606-11611, (2014).

[41] T. Yu and M. W. Wu, ***Phys. Rev. B***, 89, 205303, (2014).

[42] C. R. Zhu, K. Zhang, M. Glazov, B. Urbaszek, T. Amand, Z. W. Ji, B. L. Liu and X. Marie, ***Phys. Rev. B***, 90, 161302, (2014).

[43] X. Li, W. Cai, J. An, S. Kim, J. Nah, D. Yang, R. Piner, A. Velamakanni, I. Jung, E. Tutuc, S. K. Banerjee, L. Colombo and R. S. Ruoff, ***Science***, 324, 1312-1314, (2009).

[44] A. M. van der Zande, P. Y. Huang, D. A. Chenet, T. C. Berkelbach, Y. You, G.-H. Lee, T. F. Heinz, D. R. Reichman, D. A. Muller and J. C. Hone, ***Nat. Mater.***, 12, 554-561, (2013).

[45] W. Ge, K. Kawahara, M. Tsuji and H. Ago, ***Nanoscale***, 5, 5773-5778, (2013).

[46] Y. Gong, Z. Lin, G. Ye, G. Shi, S. Feng, Y. Lei, A. L. Elías, N. Perea-Lopez, R. Vajtai, H. Terrones, Z. Liu, M. Terrones and P. M. Ajayan, ***ACS Nano***, 9, 11658-11666, (2015).

[47] S. Li, S. Wang, D.-M. Tang, W. Zhao, H. Xu, L. Chu, Y. Bando, D. Golberg and G. Eda, ***Appl. Mater. Today***, 1, 60-66, (2015).

[48] D. Ovchinnikov, A. Allain, Y. S. Huang, D. Dumcenco and A. Kis, ***ACS Nano***, 8, 8174-8181, (2014).

[49] S. B. Desai, S. R. Madhvapathy, M. Amani, D. Kiriya, M. Hettick, M. Tosun, Y. Zhou, M. Dubey, J. W. Ager, III, D. Chrzan and A. Javey, ***Adv. Mater.***, 28, 4053-4058, (2016).

[50] W. Liu, J. Kang, D. Sarkar, Y. Khatami, D. Jena and K. Banerjee, ***Nano Lett.***, 13, 1983-1990, (2013).

[51] J. Kim, C. Jin, B. Chen, H. Cai, T. Zhao, P. Lee, S. Kahn, K. Watanabe, T. Taniguchi, S. Tongay, M. F. Crommie and F. Wang, ***Sci. Adv.***, 3, e1700518, (2017).

[52] A. L. Elías, N. Perea-López, A. Castro-Beltrán, A. Berkdemir, R. Lv, S. Feng, A. D. Long, T. Hayashi, Y. A. Kim, M. Endo, H. R. Gutiérrez, N. R. Pradhan, L.

Balicas, T. E. Mallouk, F. López-Urías, H. Terrones and M. Terrones, ***ACS Nano***, 7, 5235-5242, (2013).

[53] X. Wang, Y. Gong, G. Shi, W. L. Chow, K. Keyshar, G. Ye, R. Vajtai, J. Lou, Z. Liu, E. Ringe, B. K. Tay and P. M. Ajayan, ***ACS Nano***, 8, 5125-5131, (2014).

[54] Y. Zhang, Y. Zhang, Q. Ji, J. Ju, H. Yuan, J. Shi, T. Gao, D. Ma, M. Liu, Y. Chen, X. Song, H. Y. Hwang, Y. Cui and Z. Liu, ***ACS Nano***, 7, 8963-8971, (2013).

[55] M. Okada, T. Sawazaki, K. Watanabe, T. Taniguch, H. Hibino, H. Shinohara and R. Kitaura, ***ACS Nano***, 8, 8273-8277, (2014).

[56] Y. Kobayashi, S. Sasaki, S. Mori, H. Hibino, Z. Liu, K. Watanabe, T. Taniguchi, K. Suenaga, Y. Maniwa and Y. Miyata, ***ACS Nano***, 9, 4056-4063, (2015).

[57] Y. Gao, Z. Liu, D.-M. Sun, L. Huang, L.-P. Ma, L.-C. Yin, T. Ma, Z. Zhang, X.-L. Ma, L.-M. Peng, H.-M. Cheng and W. Ren, ***Nat. Commun.***, 6, 8569, (2015).

[58] Y.-H. Lee, X.-Q. Zhang, W. Zhang, M.-T. Chang, C.-T. Lin, K.-D. Chang, Y.-C. Yu, J. T.-W. Wang, C.-S. Chang, L.-J. Li and T.-W. Lin, ***Adv. Mater.***, 24, 2320-2325, (2012).

[59] Y. Yu, C. Li, Y. Liu, L. Su, Y. Zhang and L. Cao, ***Sci. Rep.***, 3, 1866, (2013).

[60] S. Najmaei, Z. Liu, W. Zhou, X. Zou, G. Shi, S. Lei, B. I. Yakobson, J.-C. Idrobo, P. M. Ajayan and J. Lou, ***Nat. Mater.***, 12, 754-759, (2013).

[61] K. K. Kim, A. Hsu, X. Jia, S. M. Kim, Y. Shi, M. Hofmann, D. Nezich, J. F. Rodriguez-Nieva, M. Dresselhaus, T. Palacios and J. Kong, ***Nano Lett.***, 12, 161-166, (2012).

[62] S. Reich, A. C. Ferrari, R. Arenal, A. Loiseau, I. Bello and J. Robertson, ***Phys. Rev. B***, 71, 205201, (2005).

[63] S. Azevedo, J. R. Kaschny, C. M. C. de Castilho and F. de Brito Mota, ***Nanotechnology***, 18, 495707, (2007).

[64] T. Taniguchi and K. Watanabe, ***J. Cryst. Growth***, 303, 525-529, (2007).

[65] L. Song, L. Ci, H. Lu, P. B. Sorokin, C. Jin, J. Ni, A. G. Kvashnin, D. G. Kvashnin, J. Lou, B. I. Yakobson and P. M. Ajayan, ***Nano Lett.***, 10, 3209-3215, (2010).

[66] Y. Hoshi, T. Kuroda, M. Okada, R. Moriya, S. Masubuchi, K. Watanabe, T. Taniguchi, R. Kitaura and T. Machida, ***Phys. Rev. B***, 95, 241403, (2017).

[67] A. K. Geim and I. V. Grigorieva, ***Nature***, 499, 419-425, (2013).

[68] S. Tongay, W. Fan, J. Kang, J. Park, U. Koldemir, J. Suh, D. S. Narang, K. Liu, J. Ji, J. Li, R. Sinclair and J. Wu, ***Nano Lett.***, 14, 3185-3190, (2014).

[69] H.-P. Komsa and A. V. Krasheninnikov, ***Phys. Rev. B***, 88, 085318, (2013).

[70] H. M. Hill, A. F. Rigosi, K. T. Rim, G. W. Flynn and T. F. Heinz, ***Nano Lett.***, 16, 4831-4837, (2016).

[71] K. Keyshar, M. Berg, X. Zhang, R. Vajtai, G. Gupta, C. K. Chan, T. E. Beechem, P. M. Ajayan, A. D. Mohite and T. Ohta, ***ACS Nano***, 11, 8223-8230, (2017).

[72] K. Kośmider and J. Fernández-Rossier, ***Phys. Rev. B***, 87, 075451, (2013).

[73] N. Lu, H. Guo, Z. Zhuo, L. Wang, X. Wu and X. C. Zeng, ***Nanoscale***, 9, 19131-19138, (2017).

[74] H. Heo, J. H. Sung, S. Cha, B.-G. Jang, J.-Y. Kim, G. Jin, D. Lee, J.-H. Ahn, M.-J. Lee, J. H. Shim, H. Choi and M.-H. Jo, ***Nat. Commun.***, 6, 7372, (2015).

[75] P. Rivera, J. R. Schaibley, A. M. Jones, J. S. Ross, S. Wu, G. Aivazian, P. Klement, K. Seyler, G. Clark, N. J. Ghimire, J. Yan, D. G. Mandrus, W. Yao and X. Xu, ***Nat. Commun.***, 6, 6242, (2015).

[76] Y. Gong, J. Lin, X. Wang, G. Shi, S. Lei, Z. Lin, X. Zou, G. Ye, R. Vajtai, B. I. Yakobson, H. Terrones, M. Terrones, B. K. Tay, J. Lou, S. T. Pantelides, Z. Liu, W. Zhou and P. M. Ajayan, ***Nat. Mater.***, 13, 1135-1142, (2014).

[77] H. Chen, X. Wen, J. Zhang, T. Wu, Y. Gong, X. Zhang, J. Yuan, C. Yi, J. Lou, P. M. Ajayan, W. Zhuang, G. Zhang and J. Zheng, ***Nat. Commun.***, 7, 12512, (2016).

[78] P. Nagler, G. Plechinger, M. V. Ballottin, A. Mitioglu, S. Meier, N. Paradiso, C. Strunk, A. Chernikov, P. C. M. Christianen, C. Schüller and T. Korn, ***2D Mater.***, 4, 025112, (2017).

[79] P. Rivera, K. L. Seyler, H. Yu, J. R. Schaibley, J. Yan, D. G. Mandrus, W. Yao and X. Xu, ***Science***, 351, 688-691, (2016).

[80] T. Godde, D. Schmidt, J. Schmutzler, M. Aßmann, J. Debus, F. Withers, E. M. Alexeev, O. Del Pozo-Zamudio, O. V. Skrypka, K. S. Novoselov, M. Bayer and A. I. Tartakovskii, ***Phys. Rev. B***, 94, 165301, (2016).

[81] G. Wang, L. Bouet, D. Lagarde, M. Vidal, A. Balocchi, T. Amand, X. Marie and B. Urbaszek, ***Phys. Rev. B***, 90, 075413, (2014).

[82] B. Miller, A. Steinhoff, B. Pano, J. Klein, F. Jahnke, A. Holleitner and U. Wurstbauer, ***Nano Lett.***, 17, 5229-5237, (2017).

[83] Y. Kobayashi, S. Yoshida, R. Sakurada, K. Takashima, T. Yamamoto, T. Saito, S. Konabe, T. Taniguchi, K. Watanabe, Y. Maniwa, O. Takeuchi, H. Shigekawa and Y. Miyata, ***Sci. Rep.***, 6, 31223, (2016).

[84] H. Yu, Y. Wang, Q. Tong, X. Xu and W. Yao, ***Phys. Rev. Lett.***, 115, 187002, (2015).

[85] T. Uwanno, Y. Hattori, T. Taniguchi, K. Watanabe and K. Nagashio, ***2D Mater.***,

2, 041002, (2015).

[86] L. Wang, I. Meric, P. Y. Huang, Q. Gao, Y. Gao, H. Tran, T. Taniguchi, K. Watanabe, L. M. Campos, D. A. Muller, J. Guo, P. Kim, J. Hone, K. L. Shepard and C. R. Dean, ***Science***, 342, 614-617, (2013).

[87] A. Castellanos-Gomez, M. Buscema, R. Molenaar, V. Singh, L. Janssen, H. S. J. van der Zant and G. A. Steele, ***2D Mater.***, 1, 011002, (2014).

[88] J. R. Schaibley, P. Rivera, H. Yu, K. L. Seyler, J. Yan, D. G. Mandrus, T. Taniguchi, K. Watanabe, W. Yao and X. Xu, ***Nat. Commun.***, 7, 13747, (2016).

[89] Y. Gong, S. Lei, G. Ye, B. Li, Y. He, K. Keyshar, X. Zhang, Q. Wang, J. Lou, Z. Liu, R. Vajtai, W. Zhou and P. M. Ajayan, ***Nano Lett.***, 15, 6135-6141, (2015).

[90] S. Pak, J. Lee, Y.-W. Lee, A.-R. Jang, S. Ahn, K. Y. Ma, Y. Cho, J. Hong, S. Lee, H. Y. Jeong, H. Im, H. S. Shin, S. M. Morris, S. Cha, J. I. Sohn and J. M. Kim, ***Nano Lett.***, 17, 5634-5640, (2017).

[91] X. Hong, J. Kim, S.-F. Shi, Y. Zhang, C. Jin, Y. Sun, S. Tongay, J. Wu, Y. Zhang and F. Wang, ***Nat. Nanotechnol.***, 9, 682-686, (2014).

[92] K. Wang, B. Huang, M. Tian, F. Ceballos, M. W. Lin, M. Mahjouri-Samani, A. Boulesbaa, A. A. Puretzky, C. M. Rouleau, M. Yoon, H. Zhao, K. Xiao, G. Duscher and D. B. Geohegan, ***ACS Nano***, 10, 6612-6622, (2016).

[93] S. Tongay, J. Suh, C. Ataca, W. Fan, A. Luce, J. S. Kang, J. Liu, C. Ko, R. Raghunathanan, J. Zhou, F. Ogletree, J. Li, J. C. Grossman and J. Wu, ***Sci. Rep.***, 3, 2657, (2013).

[94] J.-H. Chen, C. Jang, S. Xiao, M. Ishigami and M. S. Fuhrer, ***Nat. Nanotechnol.***, 3, 206-209, (2008).

[95] F. Cadiz, E. Courtade, C. Robert, G. Wang, Y. Shen, H. Cai, T. Taniguchi, K. Watanabe, H. Carrere, D. Lagarde, M. Manca, T. Amand, P. Renucci, S. Tongay, X. Marie and B. Urbaszek, ***Phys. Rev. X***, 7, 021026, (2017).

[96] C. R. Dean, A. F. Young, I. Meric, C. Lee, L. Wang, S. Sorgenfrei, K. Watanabe, T. Taniguchi, P. Kim, K. L. Shepard and J. Hone, ***Nat. Nanotechnol.***, 5, 722-726, (2010).

[97] M. Okada, Y. Miyauchi, K. Matsuda, T. Taniguchi, K. Watanabe, H. Shinohara and R. Kitaura, ***Sci. Rep.***, 7, 322, (2017).

[98] H. Yu, Z. Yang, L. Du, J. Zhang, J. Shi, W. Chen, P. Chen, M. Liao, J. Zhao, J. Meng, G. Wang, J. Zhu, R. Yang, D. Shi, L. Gu and G. Zhang, ***Small***, 13, 1603005, (2017).

[99] J. Zhang, H. Yu, W. Chen, X. Tian, D. Liu, M. Cheng, G. Xie, W. Yang, R. Yang, X. Bai, D. Shi and G. Zhang, ***ACS Nano***, 8, 6024-6030, (2014).

[100] Z. Wang, J. Shan and K. F. Mak, ***Nat. Nanotechnol.***, 12, 144-149, (2017).
[101] G. D. Shepard, J. V. Ardelean, O. A. Ajayi, D. Rhodes, X. Zhu, J. C. Hone and S. Strauf, ***ACS Nano***, 11, 11550-11558, (2017).

Chapter 2

2.Direct CVD growth of WS_2 on hBN

2.1. Introduction

In recent years, monolayer group VI TMDC, such as MoS_2 and WS_2, have attracted much attention as post silicon, graphene materials and represent an excellent field for exploring fundamental physics in two dimensions [1-3]. Monolayer MoS_2, WS_2, $MoSe_2$, and WSe_2 are three-atom thick, direct gap semiconductors with hexagonal lattices [4]. Their low-dimensional structures with semiconducting properties provide opportunities for applications in electronics and optoelectronics with ultimate thinness [1,5]. Furthermore, due to their low-dimensional structure, they show a strong excitonic effect from a strong many-body effect mediated by Coulomb interactions, as well as PL emission from excitons and trions even at room temperature [6-8]; recent research revealed that they have a valley degree of freedom [9,10]. Broken inversion symmetry in monolayer TMDC crystals and strong spin-orbit interactions make their K and K´ valleys distinguishable and allow the possibility of achieving "valleytronics" devices. These indicate significant opportunities for TMDC in next-generation materials for various devices and the exploration of 2D physics.

One of the greatest problems with these atomic materials is environmental effects. In atomic layered materials like WS_2, MoS_2, and graphene, almost all atoms locate at their surface. This means that their properties can be modulated easily by a substrate or by

gas adsorption. For example, free-standing high-quality graphene shows an excellent carrier mobility of over 200,000 $cm^2/(V \cdot s)$ at 5 K, but in graphene on SiO_2/Si, the carrier mobility is limited to about 10,000 $cm^2/(V \cdot s)$ [11-13]. This is caused by a substrate effect: on SiO_2, there are many charged impurities, dangling bonds, and low-energy optical phonons, together with surface roughness [14]. This is also important in TMDC – a recent study revealed that the substrate effect also degrades the electrical and optical properties of TMDC, and this causes localized states, resulting in resonant tunneling at low temperatures and variable range hopping at high temperatures [15].

To improve this, we have focused on direct CVD growth of TMDC on hBN; this is an atomic-layered dielectric with a bandgap of about 6.0–6.4 eV [16,17], and there are no dangling bonds, surface roughness, or charged impurities at its surface. Due to these characteristics, hBN has been demonstrated to be the most suitable substrate and protection layers for observing the intrinsic optical and electrical properties of 2D materials [18]. For example, the carrier mobility of graphene on an hBN substrate reaches about 60,000 $cm^2/(V \cdot s)$ even at room temperature [19]. This strongly indicates that the hBN substrate can allow us to explore new physics and electronic applications of graphene. This also occurred in TMDC – TMDC/hBN is a key structure for exploring intrinsic electrical and optical properties such as the valley Hall effect, photoinduced spin-Hall effect [9].

Here, we report the direct CVD growth of atomic layered WS_2, a group VI TMDC, on high-quality hBN (WS_2/hBN, Figure 2.1).

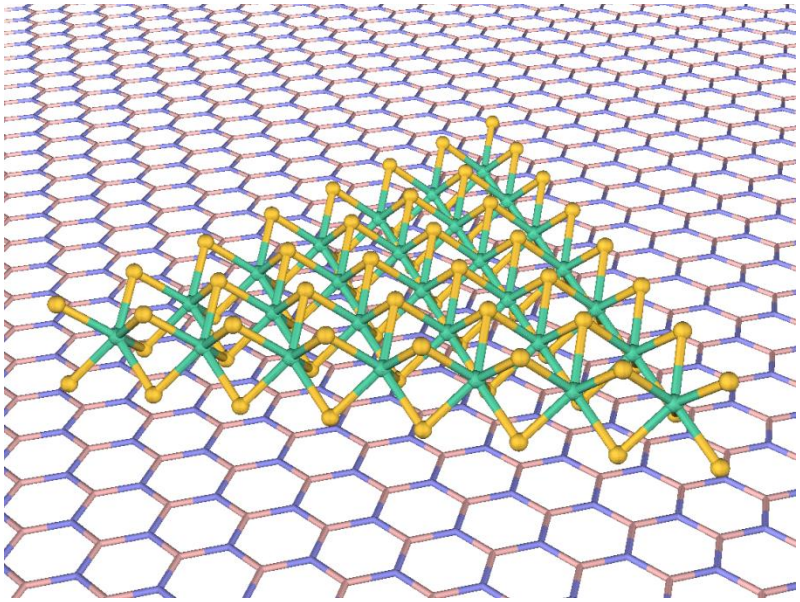

Figure 2.1. A schematic image of WS_2/hBN. The top and bottom layers correspond to WS_2 and hBN, respectively. Yellow, light green, pink, and light blue correspond to sulfur, tungsten, boron, and nitrogen atoms, respectively.

Although fabricating a TMDC/hBN structure has already been realized by many groups by mechanical exfoliation and dry or wet transfer methods, direct CVD growth of TMDC/hBN has a significant advantage over these methods [20]. When we grew a TMDC on hBN, it was deposited directly with no transfer process, realizing a clean interface between the TMDC and hBN. On the other hand, when using a dry-transfer method, polymer deposition and a transferring and washing process based on solution are required. This strongly indicates that to observe the intrinsic properties of TMDC, the clean interface between the TMDC and hBN is one of the key factors. Furthermore, the CVD growth method is more scalable and simpler than the exfoliation method. These advantages are essential for fabricating TMDC/hBN devices for exploring the intrinsic properties of TMDC.

2.2. CVD growth

Our strategy for synthesizing high-quality TMDC on hBN is the using high-quality hBN flakes. high-quality hBN flakes were obtained by a mechanical exfoliation method from single-crystal hBN synthesized by a HPHT method [21]. The typical size of hBN flakes exfoliated onto quartz, sapphire, and SiO_2/Si is several tens of micrometers. We confirmed the surface roughness of prepared hBN by AFM (Veeco Dimension 3100).

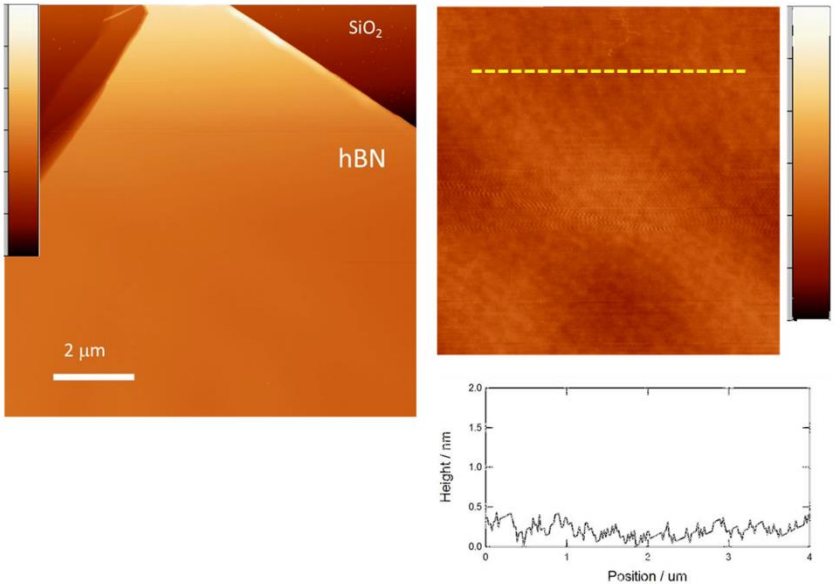

Figure 2.2. A typical AFM image and height profile of prepared hBN.

Figure 2.2 shows the result. The roughness rms is about 0.09 nm, and this means that the surface of hBN is atomically flat. The Raman spectrum of the hBN transferred to SiO_2/Si, measured at room temperature with 2.54 eV excitation (Jobin Yvon LabRAM HR-800, with COHERENT Sapphire 488 LP CW laser), shows sharp Raman peaks corresponding to the E_{2g} mode [22,23] at 1,367 cm^{-1} with a FWHM (full width at half maximum) of 8 cm^{-1}(Figure 2.3), meaning that exfoliated hBN has high crystallinity.

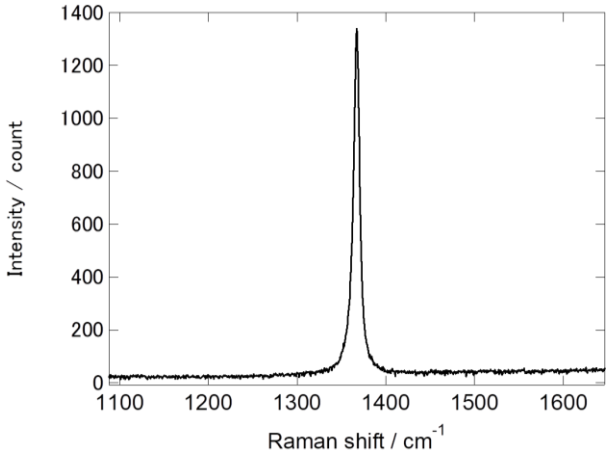

Figure 2.3. A typical Raman spectrum of hBN exfoliated on a quartz substrate.

And Figure 2.4 shows a handmade CVD growth setup for WS_2/hBN.

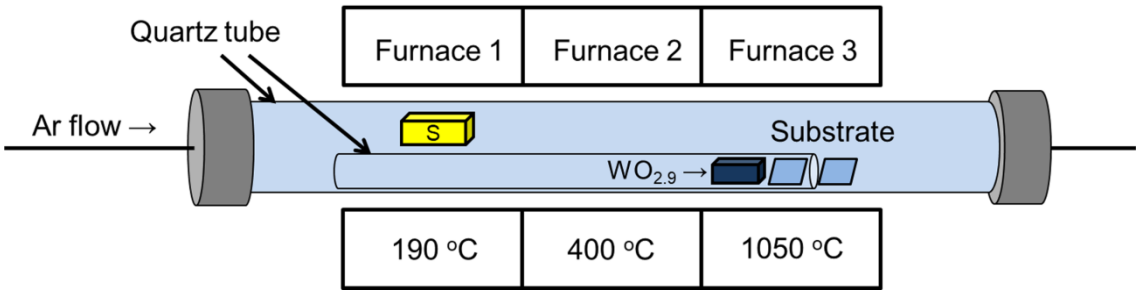

Figure 2.4. A schematic image of the setup for CVD of WS_2 on hBN.

As a precursor, we used metal oxide ($WO_{2.9}$, Alfa Aesar) and elemental sulfur. We separated the flow paths of the metal and sulfur (Sigma-Aldrich, 99.98%) precursor by using a small diameter quartz tube to avoid unwanted reaction between $WO_{2.9}$ and sulfur before reaching the substrate. (Also, the substrate was placed in the small diameter quartz tube, and $WO_{2.9}$ reacted with sulfur that flowed back from the outlet of the tube). As shown in the figure, $WO_{2.9}$ and the substrate were placed in the hottest zone, while elemental sulfur is placed in the coolest zone. A furnace placed at the center

was used as a buffer zone to avoid unwanted heating of Furnace 1. We used Ar as a buffer gas at a flow rate of 200 sccm (standard cubic centimeters per minute) at ambient pressure. The typical reaction temperature and time for this method were about 1,050 degrees and 60 minutes, respectively, and we cooled all furnaces rapidly after the growth. The CVD growth method of WS_2 on hBN using metal chloride as a precursor is reported in Reference publications No. 1.

2.3. Results and discussion

2.3.1. Elemental analysis, PL image, and AFM

Initially, we performed TEM (JEOL JEM-2100F, acceleration voltage of 80 kV) and elemental analysis. Figure 2.5 shows a typical TEM image, and EDX (energy dispersive X-ray spectroscopy) and EELS (electron-energy loss spectroscopy) spectra.

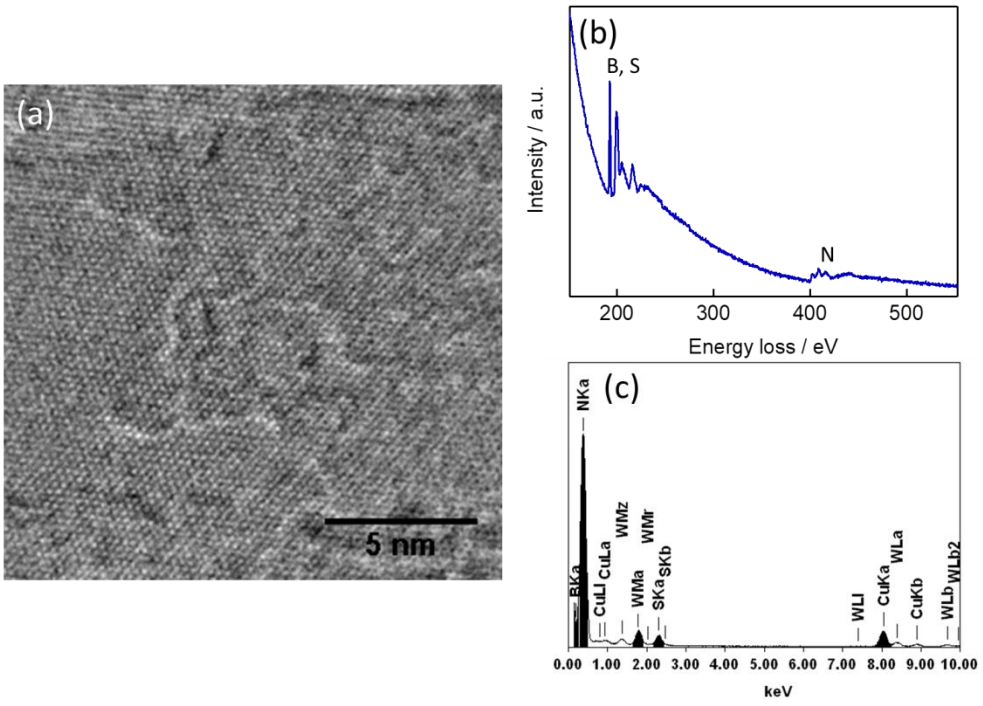

Figure 2.5. (a): A typical TEM image of WS_2/hBN; (b) and (c): corresponding (b) : EELS and

(c): EDX spectra.

In the TEM image of WS_2/hBN, we can see lattice fringes. Elemental analysis clearly shows the existence of boron, nitrogen, sulfur, and tungsten, which is consistent with WS_2/hBN, and there is no significant contamination by elements such as molybdenum and chromium. A Cu signal in the EDX spectrum originates from a copper TEM grid that we used.

Figure 2.6 shows a typical PL image of CVD grown WS_2 on hBN. We used a fluorescence microscope (Leica TCS SP8 gSTED, excitation was performed with a supercontinuum laser at 2.54 eV) to obtain this image, which was constructed from a bright field image (monochrome) and one taken at 1.77–2.07 eV (red).

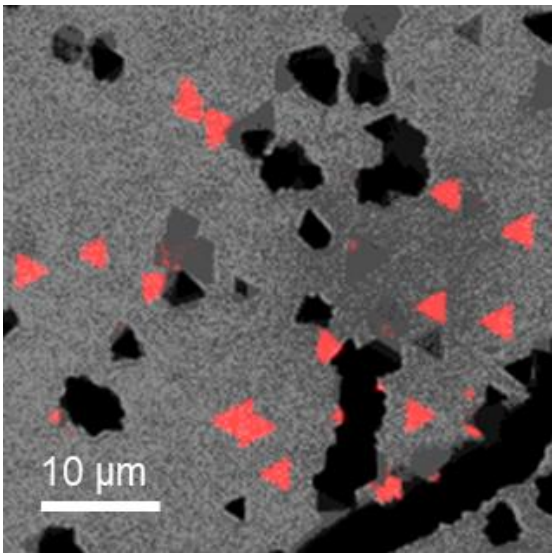

Figure 2.6. A typical PL image of WS_2/hBN.

As clearly seen in the Figure 2.6, there are strong PL emissions with triangular contrasts having an average size of ca. 2–3 μm on hBN, indicating that triangular monolayer WS_2 is formed. The dark contrast is from the bulk WS_2. The formation of

triangular WS_2 crystals suggests the appearance of the zigzag edge, which is an energetically preferred edge [7,24]. When a zig-zag sulfur or metal edge is assumed, the shape of crystal is uniquely determined as triangular. In previous reports about the CVD growth of TMDC on various substrates such as SiO_2/Si, sapphire, and graphite, the formation of triangular-shaped crystals has also been observed [24-26]. As seen in Figure 2.6, the density of WS_2 at the edge is much higher than that at the center of hBN flakes. This suggests that the edge of hBN is an effective site for nucleation for WS_2 growth. There are many dangling bonds at the hBN edge, and they provide nucleation sites during WS_2 growth. There is also a large nuclear density at the center of the hBN flakes. This might be due to the existence of large steps of hBN.

Figure 2.7 shows a typical AFM image and the corresponding height profile of CVD grown WS_2.

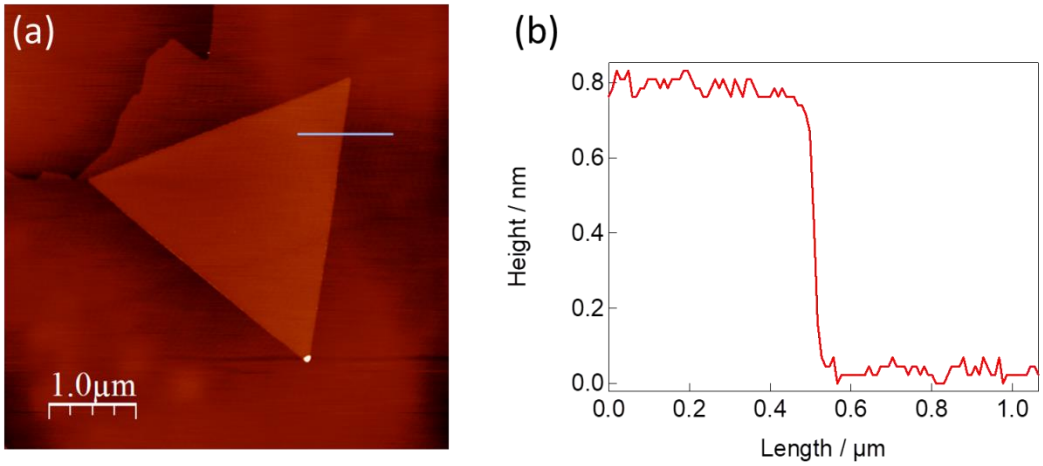

Figure 2.7. (a): AFM image of WS_2/hBN; (b): height profile along the blue line shown in Figure 2.7(a).

The figures show a triangular WS_2 crystal with a height of about 0.8 nm. This indicates that the grown WS_2 is a monolayer [7,25]. As shown in the height profile, the surface of

the WS_2 crystal is atomically flat – the surface roughness of WS_2 grown on hBN is around 0.1 nm.

2.3.2. Raman spectrum

Figure 2.8 shows a typical Raman spectrum of WS_2/hBN measured at room temperature with an excitation energy of 2.54 eV.

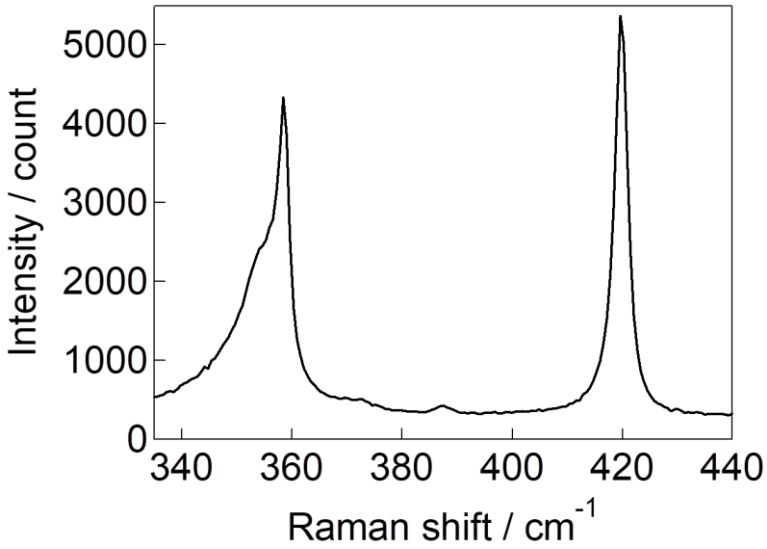

Figure 2.8. A typical Raman spectrum of WS_2/hBN.

There are two strong Raman bands appeared at 358.6 and 419.8 cm^{-1}, which originate from E´ and $A´_1$ modes, respectively [7,27,28]. The observed peak positions of these bands are different from those of bulk WS_2 (355.5 and 420.5 cm^{-1} for E´ and $A´_1$ modes, respectively). As shown in Chapter 1, this difference is caused by dielectric screening of the long-range coulombic interactions between the effective charges and interlayer van der Waals interactions [29]. Since these peaks are shifted by this interlayer coupling,

when the number of layers decreased, red and blue shifts were occurred for E´ and $A´_1$ modes, respectively. The observed peak separation between E´ and $A´_1$ modes is 61.2 cm^{-1}, consistent with monolayer WS_2 [7].

We can confirm the crystal quality by Raman spectroscopy. The observed FWHM of the $A´_1$ mode is 2.8 cm^{-1}, which is sharper than in previous studies [30] and clearly demonstrates the high crystallinity of our sample. We will discuss this further later in this thesis.

2.3.3. PL spectrum

Figure 2.9 shows a PL spectrum measured at room temperature with an excitation energy of 2.54 eV. As seen in the Figure 2.9, WS_2 shows a strong, single PL emission peak appeared at 2.014 eV, and this can be assigned to PL emission from A excitons of monolayer WS_2 [31].

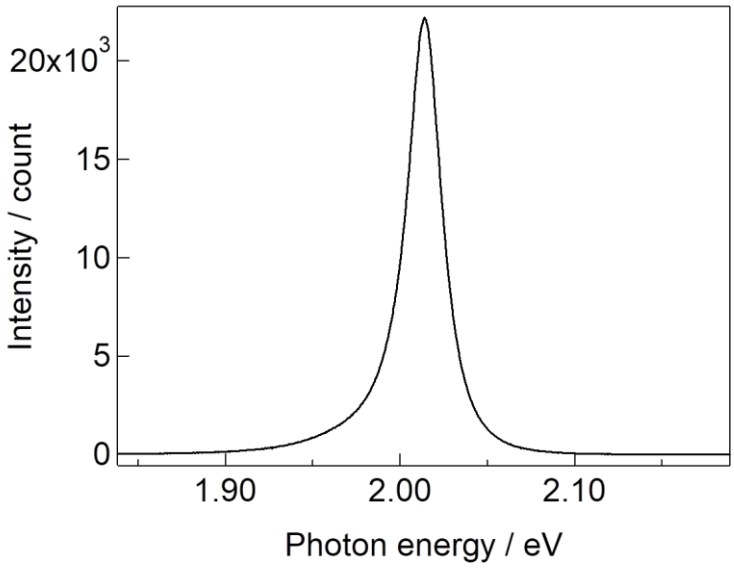

Figure 2.9. A PL spectrum of WS_2/hBN at room temperature.

The FWHM of neutral excitons in Figure 2.8 is 24 meV. This value is much smaller than those of CVD-grown and exfoliated monolayer WS_2 on SiO_2/Si or sapphire (0001) substrates (42 to 75 meV) [7,31]. And PL emission from trions in Figure 12.8 is almost negligible. This means that the amount of free carriers in our sample is small.

We tried to obtain more information on the substrate effect on PL properties. Figure 2.10 and Table 2.1 show optical images, PL spectra, and peak parameters of CVD-grown WS_2 on various substrates measured at room temperature. Peak fitting was performed with the Voigt function.

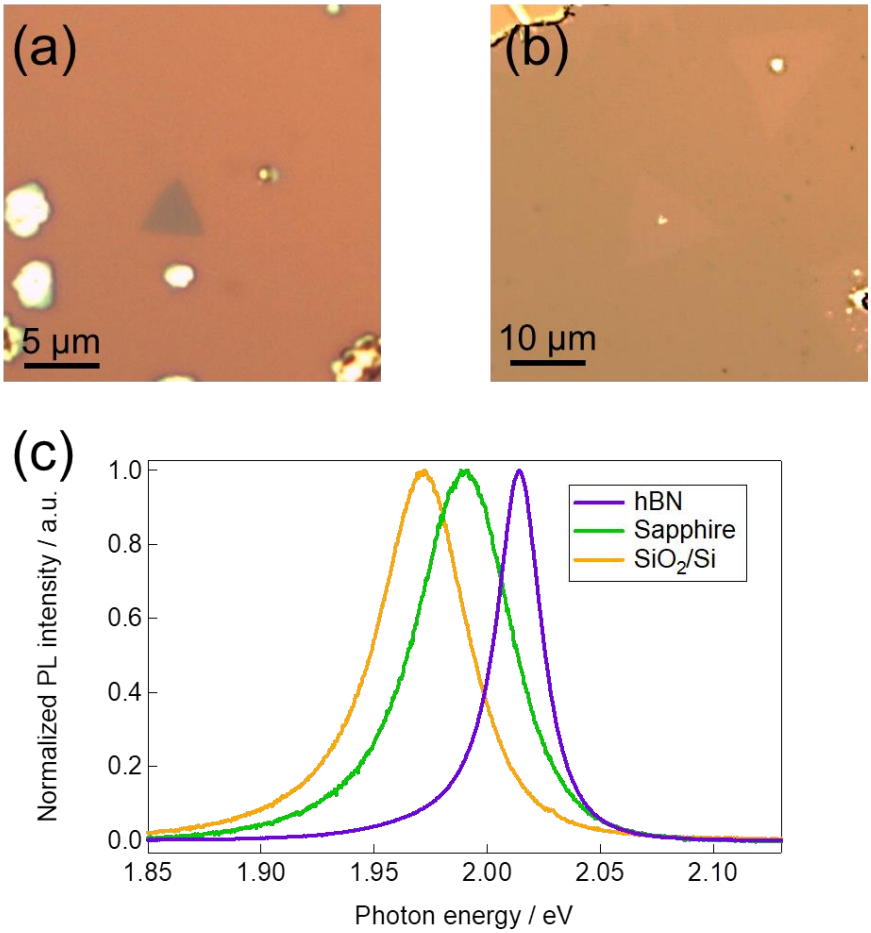

Figure 2.10. Typical optical image of WS_2 grown on (a): SiO_2 and (b): sapphire substrate; (c):

PL spectra of WS_2 grown on SiO_2/Si, sapphire, and hBN at room temperature.

Table 2.1. Peak parameters of WS_2 grown on SiO_2/Si, sapphire, and hBN.

Substrate	Peak position / eV	FWHM / meV
hBN	2.014	24
Sapphire	1.991	47
SiO_2/Si	1.972	44

As seen in Figure 2.10 and Table 2.1, WS_2 grown on hBN shows the strongest and sharpest PL spectrum. In general, the FWHM of the PL emission is related to lifetime of exciton and environment of crystal. These PL properties should originate from high-quality WS_2/hBN, indicating fewer trapping sites and reduced surface roughness in this sample. In fact, as seen in Figure 2.5, the surface of WS_2/hBN is atomically flat. A recent study revealed that WS_2 encapsulated with hBN has fewer trapping sites than WS_2 on a SiO_2/Si substrate formed by the substrate effect [32]. This ultimate flatness and small substrate effect result in sharp PL and Raman spectra for WS_2/hBN.

2.3.4. Electron diffraction and LEEM/LEED observation

Figure 2.11 shows a typical SEM image of WS_2 grown on hBN using metal chlorides as a precursor (for details, see reference publications No.1). As seen in the figure, the two dominant orientations of WS_2/hBN have relative angles of 0° and 60°. This indicates that there is a relationship between WS_2 and hBN.

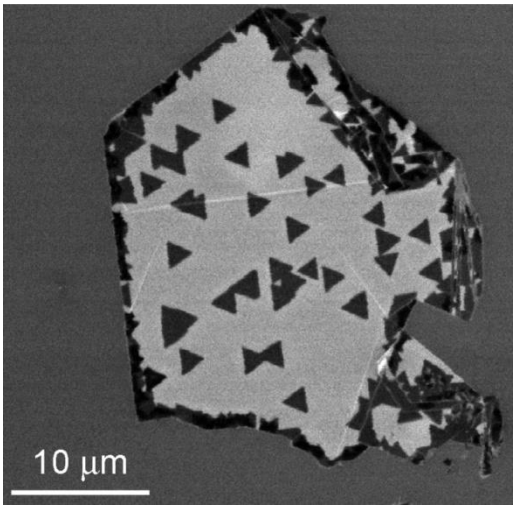

Figure 2.11. A typical SEM image of WS_2 grown on hBN. Dark triangular contrasts correspond to WS_2 grown on hBN.

To get more information about the relative orientation of these two crystals, we used LEEM (low-energy electron microscopy) and LEED (low-energy electron diffraction). Figure 2.12 shows the results.

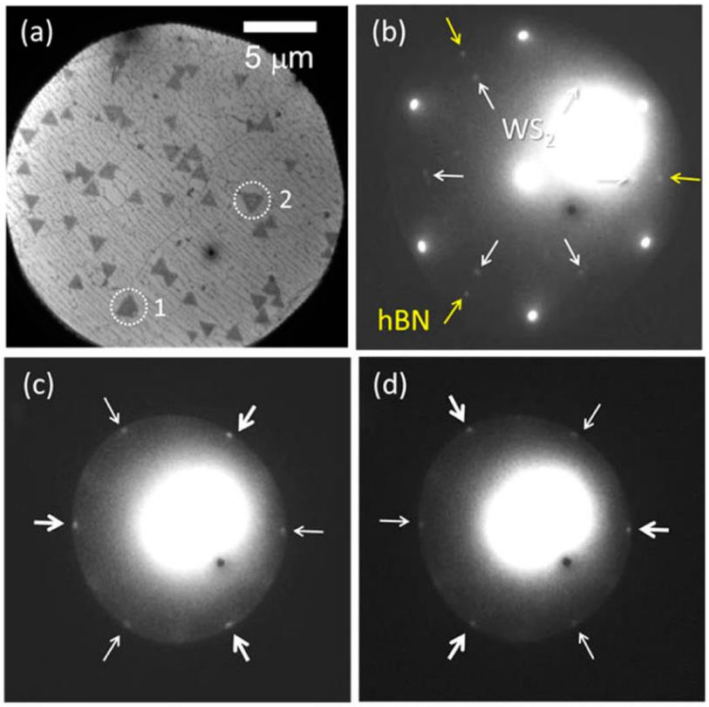

Figure 2.12. (a): LEEM image of WS_2/hBN; (b) and (c): LEED patterns of WS_2 crystal at

position 1 in (a) with electron energies of (b) 50 and (c) 22 eV; (d) LEED pattern of the crystal at position 2 in (a) with an electron energy of 22 eV.

Figure 2.12(b) shows a typical LEED pattern of WS_2/hBN. The LEED pattern of WS_2/hBN shows two hexagonal spots with three-fold symmetry. These spots come from hBN and WS_2. The strongest pattern with hexagonal spot is from graphene transferred to WS_2/hBN to avoid charging up. As clearly seen in the figure, the crystallographic orientations of WS_2 and hBN perfectly coincide. In addition, as shown in Figure 2.12(c) and (d), triangular WS_2 crystals show different LEED patterns of their different orientations; 0° or 60° rotation. This clearly indicates that all WS_2 crystals with triangular shape grown on hBN have identical edge structures, which means that existence of zigzag edges. We also measured the electron diffraction pattern of WS_2/hBN.

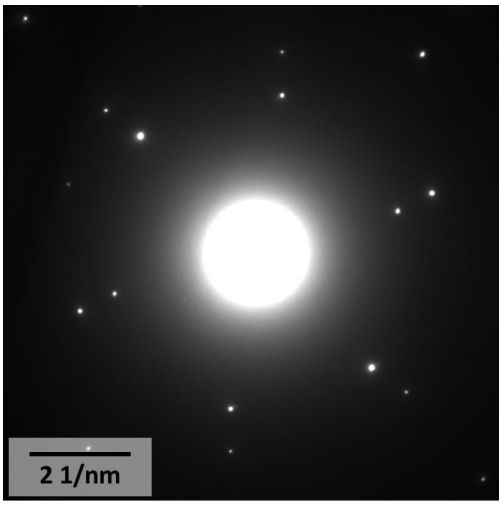

Figure 2.13. An electron diffraction pattern of WS_2/hBN. The corresponding TEM image is shown in Figure 2.5(a).

As shown in Figure 2.13, the crystallographic orientations of WS_2 and hBN are almost

the same. This means that information on crystallographic orientation between WS_2 and hBN obtained by electron diffraction pattern is also consistent with the results from the LEED observation. There is a mismatch of lattice constants between WS_2 and hBN (the lattice constant of a-axis of WS_2 and hBN are 0.318 and 0.250 nm, respectively), and WS_2 and hBN make an incommensurate moiré superlattice. And the periodicity of this superlattice is about five times larger than that of WS_2 (Figure 2.14).

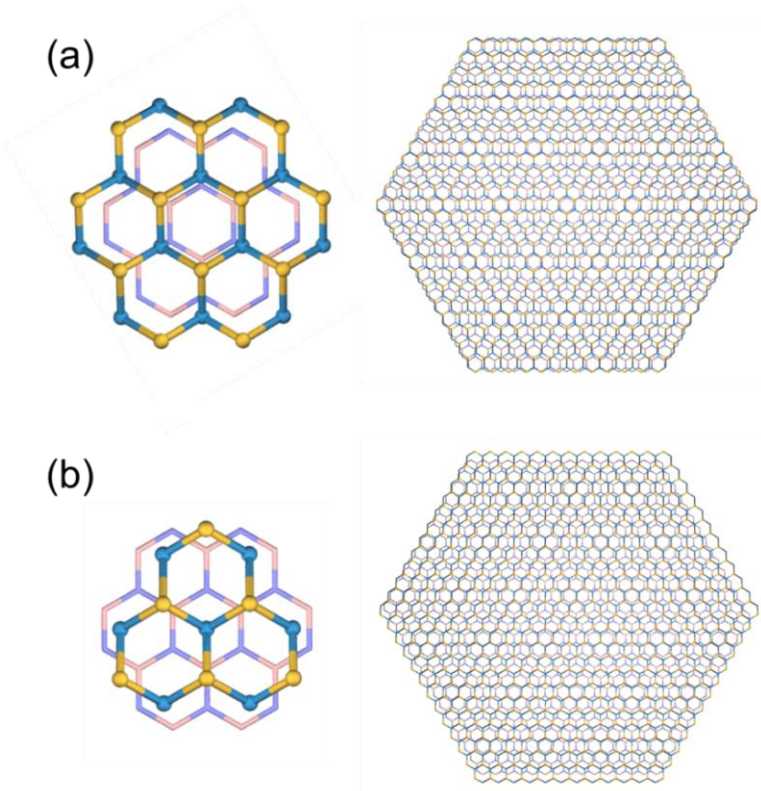

Figure 2.14. Proposed structural model of WS_2/hBN based on the PL image and the LEEM/LEED observations. WS_2 and hBN show the (a): the same and (b): inverse orientations. The top and bottom layers correspond to WS_2 and hBN, respectively. Yellow, cyan, pink, and light blue correspond to sulfur, tungsten, boron, and nitrogen atoms, respectively.

The growth mechanism of WS_2 on hBN involves a Frank-van der Merwe mechanism. In this mechanism, at first, small nuclei of WS_2 are formed. Then, these small nuclei grow

to large 2D WS_2 crystals. Since WS_2 crystals only have dangling bonds at their edges, additional precursor atoms selectively attach at their edges. Then, 2D WS_2 crystals are formed. The problem here is why WS_2 and hBN show strict crystallographic orientations. In previous reports, CVD-grown TMDC on SiO_2/Si substrates showed random crystallographic orientations [24]. On the other hand, NbS_2 and $NbSe_2$ grown on exfoliated hBN and WS_2 grown on exfoliated graphite show a similar tendency to WS_2/hBN [25,33,34]. Also, MoS_2 grown on CVD-grown graphene shows a strict relative crystallographic orientation [35]. As regards studies that used exfoliated 2D materials as a substrate, one possible explanation is that WS_2 crystals were grown from the step edge of hBN or graphite. If this hypothesis is true, most of WS_2 crystals should align at a step edge of hBN or graphite. However, this is inconsistent with most of the observed WS_2 crystals by PL image. For example, in the AFM image shown in Figure 2.7(a), there are no step edges at the edge of the WS_2 crystal, but it exists on near the WS_2; a part of Figure 2.15 shows linear alignment of the WS_2 crystal, which probably arises from the growth initiated from the step edge.

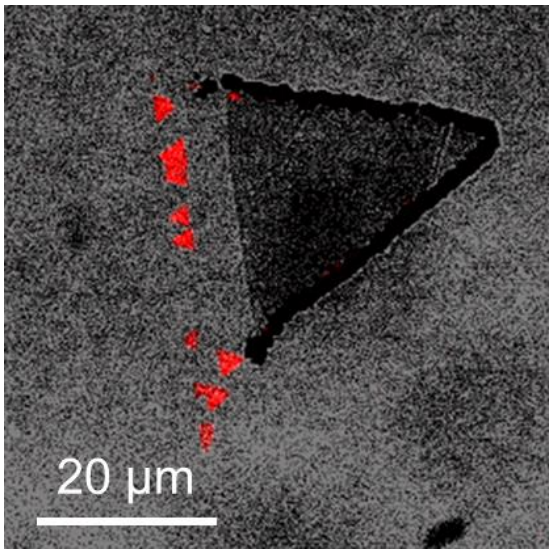

Figure 2.15. A PL image of WS_2 grown on hBN. WS_2 shows linear alignment. The coloring is the same as in Figure 2.6.

Also, this scenario is not valid for MoS_2/graphene because there are no step edges in the center of monolayer graphene. The distinct crystallographic relation between TMDC and 2D material substrates (graphite, hBN) in this and previous studies thus indicates that there is a substantial interaction between the TMDC and the substrate materials. Because TMDC, hBN, and graphite show hexagonal lattices without dangling bonds at their surfaces, van der Waals interactions and the Coulomb (especially in hBN because there are differences in electronegativity between B and N atoms) presumably play a role in to determine the orientation of WS_2 crystals on hBN. In a previous study, MoS_2 grown on sapphire (0001), which also has a hexagonal lattice, shows a similar tendency [36]. In that report, authors calculated the adsorption energies for MoS_2 and sapphire. They revealed that MoS_2 with same or inversed orientation show energy difference in in-plane translations in adsorption energies. On the other hand, with other orientations, this shows a flat energy surface, leading to the formation of aligned crystals. We believe that similar phenomena occur in our samples. Initially, small WS_2 nuclei form at the hBN surface. Then, since there is no chemical bonding between the WS_2 and hBN, WS_2 nuclei can probably rotate and translate at the early stage of the WS_2 growth. The random motion allows nuclei to adopt an energetically favored orientation and form large WS_2 atomic layers with a limited crystallographic orientation (like Figure 2.14). We counted the number of WS_2 crystals which show triangular shape in two dominant orientations. (Figure 2.16)

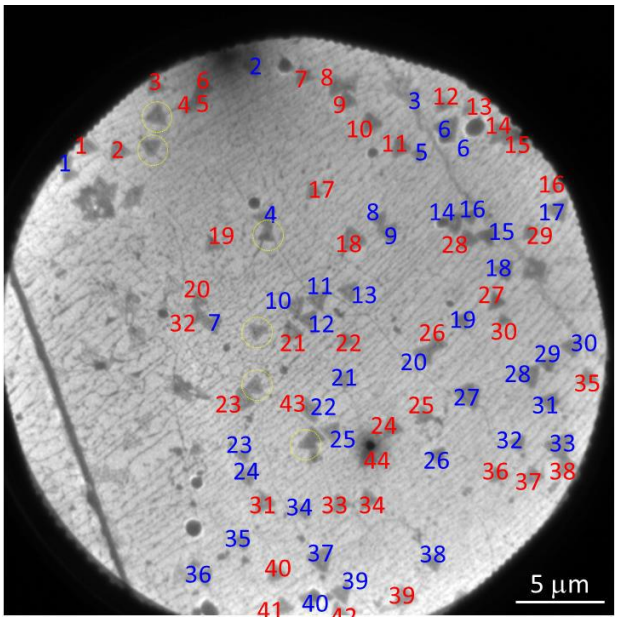

Figure 2.16. A LEEM image of the WS_2/hBN.

In Figure 2.16, triangles marked by red and blue numbers are WS_2 crystals with the two dominant orientations. Yellow circles correspond to WS_2 crystals with minor orientations. We found that the number of two dominant orientations is equally. This means that the energy difference between these orientations is small. These results strongly suggest that WS_2 grows directly on hBN, forming a clean interface.

2.4. Conclusion

In conclusion, we directly grew high-quality WS_2 atomic layers on hBN by a CVD growth method. The triangular WS_2 grown on hBN shows monolayer thickness, with Raman spectrum characteristic of monolayer WS_2, and a strong and sharp PL emission appeared at 2.014 eV at room temperature. The FWHM of the neutral excitons in PL emission peak is only 24 meV, which is much sharper than that of the WS_2 grown on the other substrate, indicating that the quality of our WS_2/hBN samples is quite high.

Furthermore, we have observed that there is a distinct relationship of crystallographic orientation between the WS_2 and hBN. This relationship may be caused by the van der Waals forces of these two layers and Coulomb interactions. This direct CVD growth method of TMDC on hBN can be applied to obtain high-quality monolayer TMDC samples. And these are suitable for exploring the intrinsic electrical and optical properties of many other TMDC and 2D materials. And which would prose to initiate a new field for exploring fundamental quantum mechanics and application based on high-quality TMDC.

In the next chapter, we report the availability of WS_2/hBN for exploring fundamental physics through observing its biexciton states.

2.5. References

[1] B. Radisavljevic, A. Radenovic, J. Brivio, V. Giacometti and A. Kis, ***Nat. Nanotechnol.***, 6, 147-150, (2011).

[2] K. F. Mak, C. Lee, J. Hone, J. Shan and T. F. Heinz, ***Phys. Rev. Lett.***, 105, 136805, (2010).

[3] Y. You, X.-X. Zhang, T. C. Berkelbach, M. S. Hybertsen, D. R. Reichman and T. F. Heinz, ***Nat. Phys.***, 11, 477-481, (2015).

[4] A. Kumar and P. K. Ahluwalia, ***Eur. Phys. J. B***, 85, 186, (2012).

[5] Q. H. Wang, K. Kalantar-Zadeh, A. Kis, J. N. Coleman and M. S. Strano, ***Nat. Nanotechnol.***, 7, 699-712, (2012).

[6] A. Splendiani, L. Sun, Y. Zhang, T. Li, J. Kim, C. Y. Chim, G. Galli and F. Wang, ***Nano Lett.***, 10, 1271-1275, (2010).

[7] H. R. Gutiérrez, N. Perea-López, A. L. Elías, A. Berkdemir, B. Wang, R. Lv, F. López-Urías, V. H. Crespi, H. Terrones and M. Terrones, ***Nano Lett.***, 13, 3447-3454, (2012).

[8] K. F. Mak, K. He, C. Lee, G. H. Lee, J. Hone, T. F. Heinz and J. Shan, ***Nat. Mater.***, 12, 207-211, (2013).

[9] D. Xiao, G.-B. Liu, W. Feng, X. Xu and W. Yao, ***Phys. Rev. Lett.***, 108, 196802, (2012).

[10] K. F. Mak, K. He, J. Shan and T. F. Heinz, ***Nat. Nanotechnol.***, 7, 494-498, (2012).

[11] E. V. Castro, H. Ochoa, M. I. Katsnelson, R. V. Gorbachev, D. C. Elias, K. S. Novoselov, A. K. Geim and F. Guinea, ***Phys. Rev. Lett.***, 105, 266601, (2010).

[12] K. S. Novoselov, A. K. Geim, S. V. Morozov, D. Jiang, Y. Zhang, S. V. Dubonos, I. V. Grigorieva and A. A. Firsov, ***Science***, 306, 666-669, (2004).

[13] K. I. Bolotin, K. J. Sikes, Z. Jiang, M. Klima, G. Fudenberg, J. Hone, P. Kim and H. L. Stormer, ***Solid State Commun.***, 146, 351-355, (2008).

[14] J.-H. Chen, C. Jang, S. Xiao, M. Ishigami and M. S. Fuhrer, ***Nat. Nanotechnol.***, 3, 206-209, (2008).

[15] H. Qiu, T. Xu, Z. Wang, W. Ren, H. Nan, Z. Ni, Q. Chen, S. Yuan, F. Miao, F. Song, G. Long, Y. Shi, L. Sun, J. Wang and X. Wang, ***Nat. Commun.***, 4, 2642, (2013).

[16] L. Museur, G. Brasse, A. Pierret, S. Maine, B. Attal-Tretout, F. Ducastelle, A. Loiseau, J. Barjon, K. Watanabe, T. Taniguchi and A. Kanaev, ***Phys. Status Solidi RRL***, 5, 214-216, (2011).

[17] K. Watanabe, T. Taniguchi and H. Kanda, ***Nat. Mater.***, 3, 404-409, (2004).

[18] C. R. Dean, A. F. Young, P. Cadden-Zimansky, L. Wang, H. Ren, K. Watanabe, T. Taniguchi, P. Kim, J. Hone and K. L. Shepard, ***Nat. Phys.***, 7, 693-696, (2011).

[19] C. R. Dean, A. F. Young, I. Meric, C. Lee, L. Wang, S. Sorgenfrei, K. Watanabe, T. Taniguchi, P. Kim, K. L. Shepard and J. Hone, ***Nat. Nanotechnol.***, 5, 722-726, (2010).

[20] G.-H. Lee, Y.-J. Yu, X. Cui, N. Petrone, C.-H. Lee, M. S. Choi, D.-Y. Lee, C. Lee, W. J. Yoo, K. Watanabe, T. Taniguchi, C. Nuckolls, P. Kim and J. Hone, ***ACS Nano***, 7, 7931-7936, (2013).

[21] T. Taniguchi and K. Watanabe, ***J. Cryst. Growth***, 303, 525-529, (2007).

[22] S. Reich, A. C. Ferrari, R. Arenal, A. Loiseau, I. Bello and J. Robertson, ***Phys. Rev. B***, 71, 205201, (2005).

[23] R. Geick, C. H. Perry and G. Rupprecht, ***Phys. Rev.***, 146, 543-547, (1966).

[24] A. M. van der Zande, P. Y. Huang, D. A. Chenet, T. C. Berkelbach, Y. You, G.-H. Lee, T. F. Heinz, D. R. Reichman, D. A. Muller and J. C. Hone, ***Nat. Mater.***, 12, 554-561, (2013).

[25] Y. Kobayashi, S. Sasaki, S. Mori, H. Hibino, Z. Liu, K. Watanabe, T. Taniguchi, K. Suenaga, Y. Maniwa and Y. Miyata, ***ACS Nano***, 9, 4056-4063, (2015).

[26] Y. Zhang, Y. Zhang, Q. Ji, J. Ju, H. Yuan, J. Shi, T. Gao, D. Ma, M. Liu, Y. Chen, X. Song, H. Y. Hwang, Y. Cui and Z. Liu, ***ACS Nano***, 7, 8963-8971, (2013).

[27] H. Zeng, G.-B. Liu, J. Dai, Y. Yan, B. Zhu, R. He, L. Xie, S. Xu, X. Chen, W. Yao and X. Cui, ***Sci. Rep.***, 3, 1608, (2013).

[28] H. Terrones, E. Del Corro, S. Feng, J. M. Poumirol, D. Rhodes, D. Smirnov, N. R. Pradhan, Z. Lin, M. A. Nguyen, A. L. Elias, T. E. Mallouk, L. Balicas, M. A. Pimenta and M. Terrones, ***Sci. Rep.***, 4, 4215, (2014).

[29] H. Li, Q. Zhang, C. C. R. Yap, B. K. Tay, T. H. T. Edwin, A. Olivier and D. Baillargeat, ***Adv. Funct. Mater.***, 22, 1385-1390, (2012).

[30] Y. Gao, Z. Liu, D.-M. Sun, L. Huang, L.-P. Ma, L.-C. Yin, T. Ma, Z. Zhang, X.-L. Ma, L.-M. Peng, H.-M. Cheng and W. Ren, ***Nat. Commun.***, 6, 8569, (2015).

[31] W. Zhao, Z. Ghorannevis, L. Chu, M. Toh, C. Kloc, P.-H. Tan and G. Eda, ***ACS Nano***, 7, 791-797, (2012).

[32] Y. Hoshi, T. Kuroda, M. Okada, R. Moriya, S. Masubuchi, K. Watanabe, T. Taniguchi, R. Kitaura and T. Machida, ***Phys. Rev. B***, 95, 241403, (2017).

[33] S. Zhao, T. Hotta, T. Koretsune, K. Watanabe, T. Taniguchi, K. Sugawara, T. Takahashi, H. Shinohara and R. Kitaura, ***2D Mater.***, 3, 025027, (2016).

[34] T. Hotta, T. Tokuda, S. Zhao, K. Watanabe, T. Taniguchi, H. Shinohara and R.

Kitaura, ***Appl. Phys. Lett.***, 109, 133101, (2016).

[35] H. Ago, H. Endo, P. Solis-Fernández, R. Takizawa, Y. Ohta, Y. Fujita, K. Yamamoto and M. Tsuji, ***ACS Appl. Mater. Interfaces***, 7, 5265-5273, (2015).

[36] D. Dumcenco, D. Ovchinnikov, K. Marinov, P. Lazić, M. Gibertini, N. Marzari, O. L. Sanchez, Y.-C. Kung, D. Krasnozhon, M.-W. Chen, S. Bertolazzi, P. Gillet, A. Fontcuberta i Morral, A. Radenovic and A. Kis, ***ACS Nano***, 9, 4611-4620, (2015).

Chapter 3

3.Biexcitonic emission from WS_2 grown on hBN

3.1. Introduction

As shown in Chapter 2, we obtained high-quality WS_2 samples by direct CVD growth on hBN. To confirm the quality of samples, we focused on their PL properties.

Monolayer group VI TMDC represent an excellent field for exploring fundamental physics in two dimensions, such as excitonic effects and correlated effects in optical properties [1-4]. Due to the huge binding energy of excitons in TMDC, we can observe PL emission from excitons and trions even at room temperature [4-12]. We can also expect the emergence of further peculiar complex many-body states like higher-order excitons in TMDC [13-15]. For example, we can expect the existence of biexcitons, higher order excitonic states that contain two electrons and two holes. The binding energy of a biexciton is proportional to the ratio of the carrier's effective mass, dimensionality, and exciton binding energy [16,17]. In WS_2, due to the large binding energy of excitons (estimated as about 0.32 to 0.71 eV) [11,12,18], we can expect the emergence of biexciton states, but there are a few reports of successful observation of this state [19-22]. And one of these reports states that to observe biexcitons, it needs high excitation power (e.g., over 25 kW/cm^2) [21].

Here, we report the observation and stabilization of biexciton states in WS_2 atomic layers grown on hBN. As shown in Chapter 2, we achieved high-quality WS_2 samples by a direct CVD growth method onto exfoliated hBN. CVD-grown WS_2 on hBN (WS_2/hBN) shows sharper PL emission than that of other substrates. This means that there are no trap states resulting from the substrate effect, and excitons can diffuse longer than in WS_2 on other substrates and form biexcitons; thus, we can expect stabilization of biexciton states, and our sample allows these fundamental quantum mechanics to be observed. As shown in Chapter 2, while WS_2/hBN shows a single peak PL emission from neutral excitons at room temperature, at 80 K, WS_2/hBN shows four peaks around 1.99–2.10 eV in the PL spectrum. Through detailed PL measurement, we conclude that these can be assigned to PL emission from excitons, trions, another trion state, and a biexciton state. Interestingly, we have observed biexciton states even at an extremely low excitation power of about 240 W/cm^2 at 82 K. The excitation power at which we observed the biexciton state is about 18 or 100 times lower than in previous reports [21,22]. These results clearly indicate that in our sample, higher order excitonic states are stabilized, providing an excellent opportunity for investigating these states in a TMDC.

3.2. Observing biexcitonic emission from WS_2/hBN

3.2.1. Temperature dependence of PL

Initially, we cooled WS_2/hBN samples cryostatically (CryoVac GmbH Conti-Cryo-Micro, with temperature controller TIC-304 MA or Janis cryostat) and measured PL properties with a confocal measurement system (Horiba Jobin Yvon LabRAM HR-800 or a handmade PL measurement system). For excitation, we used a

488 nm CW laser (COHERENT Sapphire LP) (Figure 3.1(a)) or a 520 nm supercontinuum laser (Figure 3.1(b)).

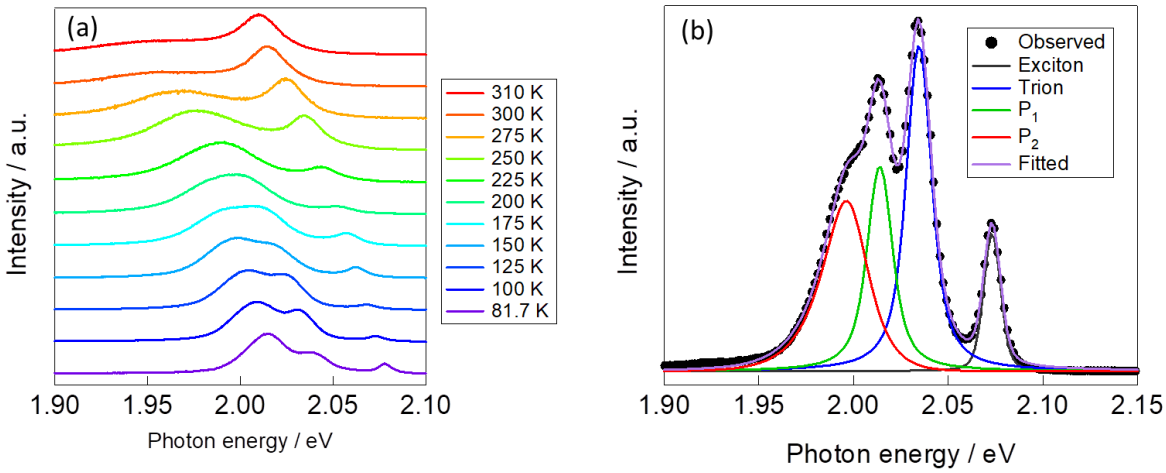

Figure 3.1 (a): Temperature dependence of PL properties of WS_2/hBN; (b): PL spectrum of WS_2/hBN at 80 K.

Figure 3.1(a) shows the temperature dependence of the PL properties of WS_2/hBN. At room temperature, as before, WS_2/hBN shows single-peak PL emission originating from excitons. However, at low temperatures, WS_2/hBN show additional PL peaks from other excitonic states, such as trion and trapped states. This is because at room temperature, excitons trapped in these states can revert to free excitons by absorbing thermal energy. However, at low temperatures, they do not have enough energy to revert to free excitons and we can observe PL emissions from these states. In fact, at 175 K, there are three peaks around 2.0 to 2.1 eV (Figure 3.1(a)). Figure 3.1(b) show the PL spectrum measured at 80 K. They show four peaks in this spectral region. Fitting of these peaks was done with Voigt function (for exciton, trion, and P_1) and distribution function of biexcitons in two dimension (for P_2) as follows [23]:

$$\mathrm{I_{XX}}(\hbar\omega) = \frac{\exp\left(-\dfrac{E_{\mathrm{ex}} - E_{\mathrm{XP_2}} - \hbar\omega}{k_{\mathrm{B}} T_{\mathrm{eff}}}\right)}{1 + \exp\left(-\dfrac{E_{\mathrm{ex}} - E_{XP_2} - \hbar\omega}{\Gamma_{\mathrm{BE}}}\right)} \tag{2.1}$$

$E_{\mathrm{ex}}, E_{\mathrm{XP}_2}, \hbar\omega, k_{\mathrm{B}},$ and T_{eff} correspond to the peak position of exciton, binding energy of biexciton, photon energy, Boltzmann constant and effective temperature, respectively. The denominator of equation (2.1) represents the 2D density of states (step like) with broadening factor, Γ_{BE}.

It is clear that PL emission at 2.073 eV is from excitons and that at 2.035 eV is from trions because their binding energy is 39 meV, which is consistent with previous reports [11,24]. However, it is difficult to assign the PL peaks denoted as P_1 (at 2.014 eV) and P_2 (at 1.998 eV) in Figure 3.1(b). To assign these features, we measured three PL properties: the excitation power dependence, the circularly polarized excitation PL, and time-resolution PL.

At low temperatures, we can observe a blue shift of exciton peaks (Figure 3.1(a)). This is caused by electron-phonon interactions and can be fitted with a Varshni plot, which explains band gap modulation by this interaction [25]. The Varshni equation is defined as follows:

$$\mathrm{E_g} = E_0 - \frac{\alpha T^2}{T + \beta} \tag{2.2}$$

Eg, E_0, and T correspond to the energy gap, energy gap at 0 K, and temperature, respectively, while α and β are constants. The result of fitting is shown in Figure 3.2 and Table 3.1. In this result, at P_1 state, contribution from P_2 state might exist.

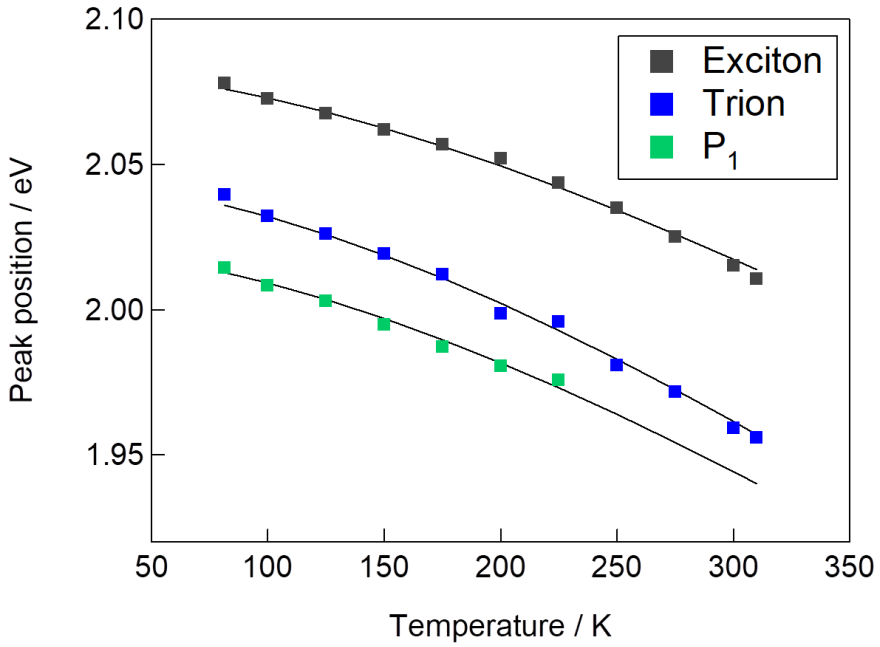

Figure 3.2. Varshni plot

Table 3.1 : Varshni parameters

		Obtained value
Exciton	α / eVK^{-1}	0.000589
	β / K	514.1
	E(0) / eV	2.083
Trion	α / eVK^{-1}	0.000719
	β / K	480.0
	E(0) / eV	2.045
P_1	α / eVK^{-1}	0.000657
	β / K	473.5
	E(0) / eV	2.021

3.2.2. Excitation power dependence

To assign these features, the most simple and effective method is to measure their excitation power dependence. We can estimate their origin by fitting this equation to the

experimental results:

$$I \propto I_{ex}^{\alpha} \qquad (2.3)$$

I, I_{ex}, and α correspond to the integrated intensity of the peak, the integrated intensity of excitons, and a constant, respectively. Typical values of α in PL emission from trion and localized states are about 1.1 and 0.6, respectively [19]. On the other hand, biexcitons show superlinear dependence (α ~ 1.2 to 1.9) [14,19,22]. We measured excitation power dependence at 80 K from excitation power of 0.37 μJ/cm^2 to 6.6 μJ/cm^2. The result is shown in Figure 3.3(a).

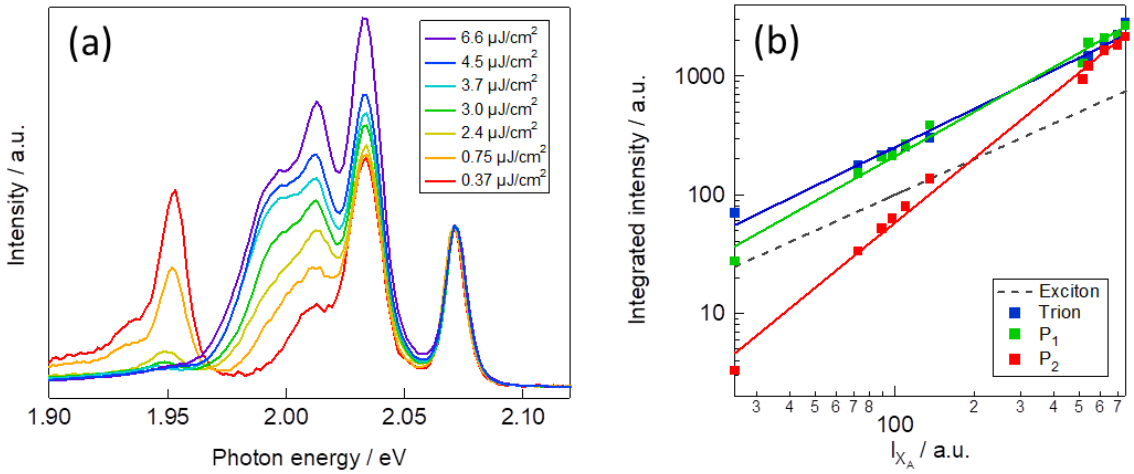

Figure 3.3 (a): Excitation power dependence PL of WS_2/hBN at 80 K. (b): Excitation power dependence of trion, P_1, and P_2.

As shown in Figure 3.3(b), trion and P_1 states show similar α value of about 1.08 and 1.25, respectively. This indicates that P_1 originates from another trion state. On the other hand, as shown in Figure 3.3(b), the P_2 state exhibits a superlinear relationship, and α is about 1.82. This clearly indicates that this state originates from biexcitons. To assign this state as biexciton, we must check that α does not reach 2. Since biexcitons are

formed when two excitons collide, in an ideal case such as the GaAs quantum well system, where the full thermal equilibrium exists, biexciton states should show α = 2 [26]. Usually, α does not reach 2 and is typically about 1.2 to 1.9 in TMDC [14,19,22]. This is because, due to the large binding energy of the biexciton state (we will discuss this later), there is no thermal equilibrium between the exciton and biexciton states, and biexcitons cannot be decomposed into two excitons. This results in a small value of α, which is consistent with previous reports.

3.2.3. Binding energy of biexciton states

As shown earlier, the binding energy of biexcitons is related to that of excitons. In our case, the binding energy of a biexciton is calculated from the difference between the photon emission energy peaks.

$$E = E_{ex} - E_{P_2} \quad (2.4)$$

E_{Ex} and E_{P2} are the PL emission energies of exciton and P_2 states, respectively. Using this equation, we calculated the binding energy of biexcitons as 75 meV. The ratio of the binding energy of a biexciton to that of an exciton, which is known as the Haynes factor, is about 0.11 to 0.23. This is consistent with previous reports including quantum well system [14,16,27] and is about ten times larger than the thermal energy at 80 K (k_BT = 6.9 meV). This large biexciton binding energy prohibits the decomposition of biexcitons into two excitons. The observed binding energy of biexcitons is larger than in previous reports [19,21,22]. Since Bohr radii of biexcitons are larger than that of excitons and would be more sensitive to screening. The difference of density of free carriers and environment, especially the difference of the substrate might make binding energy of

biexcitons large in WS_2/hBN.

3.2.4. Circularly polarized excitation PL

To obtain more evidence to assign P_2 to biexciton states, we measured their valley polarization using a circularly polarized supercontinuum laser at 2.33 eV with an input power of 15 uJ/cm^2 at 54 K. Figure 3.4 shows the results. To calculate the valley polarization, we used this equation:

$$P = \frac{I(\sigma+) - I(\sigma-)}{I(\sigma+) + I(\sigma-)} \quad (2.5)$$

P, I(σ+), and I(σ-) correspond to the polarization, and the intensities of peaks showing co-circular and contra-circular polarization with excitation.

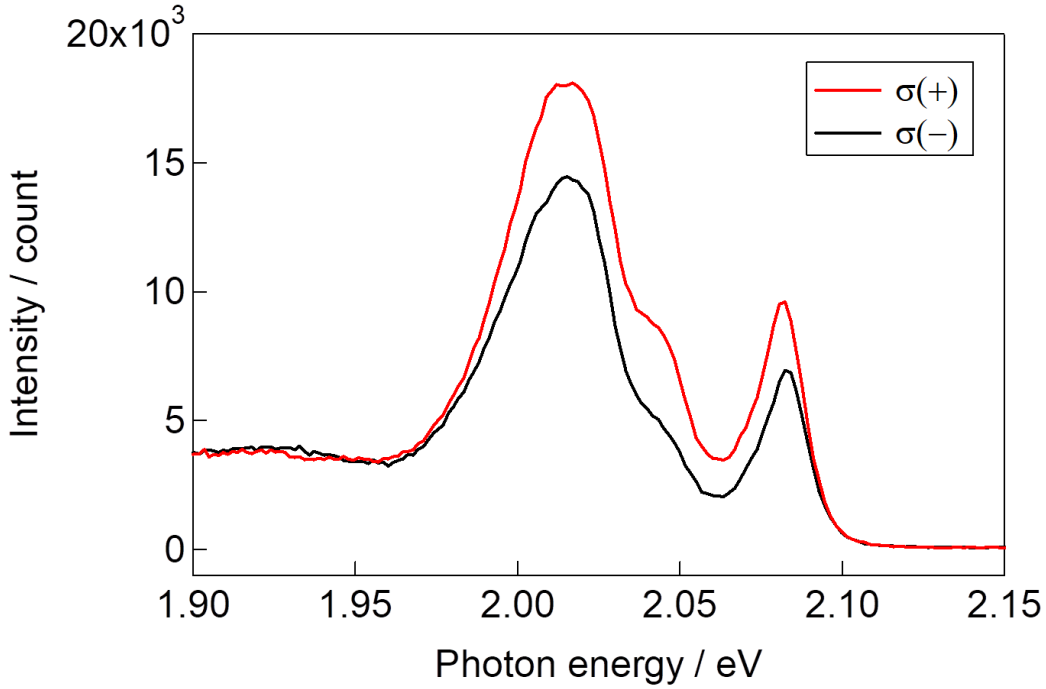

Figure 3.4. Circularly polarized excitation PL.

Table 3.2. Calculated valley polarization.

State	Exciton	Trion	P_1	P_2
Polarization	0.176	0.266	0.201	0.127

As shown in Table 3.2, the P_2 state shows valley polarization of about 13 percent. This is smaller than that of excitons and trions. In previous reports, the valley polarization of biexcitons is also smaller than that of excitons and trions, and if the states originated from localized states, they showed no valley polarization [14,21]. The fact that P_2 states show smaller valley polarization than excitons and trions supports our argument.

3.2.5. Time-resolution PL

We measured the PL lifetimes of these states at 80 K, to obtain further information on them. Since four peaks in the PL spectrum are merged, we used a band-pass filter (Semrock® laser line filter 633 nm) and a combination of long-pass and short-pass filters to select these peaks. We used the following biexponential function,

$$\mathrm{D(t)} = A * \exp\left(-\frac{t}{\tau_1}\right) + (1-A) * \exp\left(-\frac{t}{\tau_2}\right) \quad (2.6)$$

where τ_1, τ_2, and A are the lifetimes of the fast and slow decay components, and the ratio of τ_1 to τ_2, respectively. By convoluting this function and the instrument response function (IRF), we fitted the obtained time-resolved PL intensity. The obtained time-resolved PL intensity and fittings are shown in Figure 3.5.

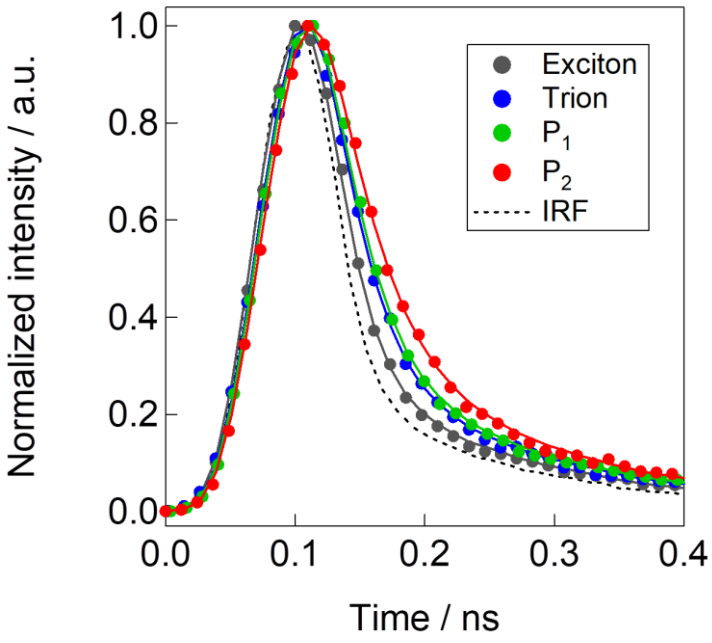

Figure 3.5. Time-resolution PL of WS_2/hBN. Black dotted line shows impulse response function.

Table 3.3. shows the fitting results.

Table 3.3. calculated radiative lifetime of PL peaks at 80 K.

	Exciton	Trion	P_1	P_2
τ_1 / ps	15	22	24	31

Table 3.3 shows the fast decay component of fitting. Obtained the lifetimes of excitons, trions, P_1, and P_2 are 15, 22, 24, and 31 ps, respectively. This result indicates that the lifetime of biexcitons is shorter than that of excitons, which is also consistent with previous reports, and this short lifetime means that P_2 does not originate from a localized state [14], but this is not consistent with the results from a conventional quantum well system, where the lifetime of biexcitons is half that of excitons [26]. This

difference is caused by the large binding energy of excitons. As shown earlier, the binding energy of biexcitons (~75 meV) is larger than the thermal activation energy at 80 K (~6.9 meV). Also, there is no thermal equilibrium between exciton and biexciton states. This lack of thermal equilibrium results in long lifetimes.

The following processes are assumed,

$$2\mathrm{X} \rightleftarrows \mathrm{XX}$$

$$\mathrm{X} \rightarrow \mathrm{T}$$

$$\mathrm{X} \rightarrow \hbar\omega_{\mathrm{X}}$$

$$\mathrm{XX} \rightarrow \mathrm{X} + \hbar\omega_{\mathrm{XX}}$$

where X, XX, T, $\hbar\omega_{\mathrm{x}}$, and $\hbar\omega_{\mathrm{XX}}$ are excitons, biexcitons, trions, and PL emissions of excitons and biexcitons, respectively. From these processes with assuming the non-radiative decay process, we obtained the following rate equation for the number of excitons and biexcitons;

$$\frac{dN_{\mathrm{X}}(t)}{dt} = G - \left(\frac{1}{\tau_{\mathrm{XR}}} + \frac{1}{\tau_{\mathrm{T}}} + \frac{1}{\tau_{\mathrm{NR}}}\right) * N_{\mathrm{X}}(t) - \frac{2}{\tau_{\mathrm{EB}}} * N_{\mathrm{X}}(t)^2 + \left(\frac{1}{\tau_{\mathrm{XXR}}} + \frac{2}{\tau_{\mathrm{BE}}}\right) * N_{\mathrm{XX}}(t) \tag{2.7}$$

$$\frac{d}{dt}N_{\mathrm{XX}}(t) = \frac{1}{\tau_{\mathrm{EB}}} * N_{\mathrm{X}}(t)^2 - \left(\frac{1}{\tau_{\mathrm{BE}}} + \frac{1}{\tau_{\mathrm{XXR}}} + \frac{1}{\tau_{\mathrm{XXNR}}}\right) * N_{\mathrm{XX}}(t) \tag{2.8}$$

G corresponds to an exciton generation function, and t, N_X, and N_{XX} correspond to the time, the number of excitons, and the number of biexcitons; τ_{XR}, τ_T, τ_{NR}, τ_{EB}, τ_{BE}, τ_{XXR}, and τ_{XXNR} represent the radiative lifetimes of excitons, lifetimes of exciton-trion conversion, non-radiative decay of excitons, lifetimes of exciton-biexciton conversion and biexciton-exciton conversion, and radiative and non-radiative decay of biexcitons, respectively. These two equations cannot be solved numerically, but assuming that the number of excitons follows a single exponential decay process,

$$N_{\mathrm{X}}(t) = N_{\mathrm{X}}(0) * \exp\left(-\frac{1}{\tau_{\mathrm{X,obs}}}\right) \tag{2.9}$$

we can obtain the number of biexcitons numerically under the steady state approximation.

$$N_{\mathrm{XX}}(t) = \frac{\tau_1\tau_2}{\tau_1 - \tau_2} * \left(\frac{N_{\mathrm{X}}(0)^2}{\tau_{\mathrm{EB}}}\right) * \left(\exp\left(-\frac{1}{\tau_1}\right) - \frac{\tau_2}{\tau_1} * \exp\left(-\frac{t}{\tau_2}\right)\right) \tag{2.10}$$

$$\frac{1}{\tau_1} = \frac{2}{\tau_{\mathrm{X,obs}}}, \quad \frac{1}{\tau_2} = \frac{1}{\tau_{\mathrm{BE}}} + \frac{1}{\tau_{\mathrm{XXR}}} + \frac{1}{\tau_{\mathrm{XXNR}}}$$

As shown in equation (2.10), the number of excitons is composed of two terms. The lifetime of biexcitons should be half of that of excitons when the first decay term, $\exp\left(-\frac{1}{\tau_1}\right)$ is dominant. On the other hand, when the second term, $\exp\left(-\frac{t}{\tau_2}\right)$ is not negligible, the lifetime of biexcitons is no longer half that of excitons. In the cases like the quantum well system, due to the small binding energy of biexcitons (~ 2 meV in GaAs quantum well), the second term in equation (2.10) is negligible and biexcitons show shorter lifetime than that of excitons [26,28]. On the other hand, in WS_2/hBN, since the binding energy of biexcitons is large enough to avoid decomposition of biexcitons into excitons, the second term in equation (2.10) is not negligible. This makes the observed long lifetime of biexcitons possible. This is consistent with previous reports. Similar tendency of long lived biexcitons are also observed in (Zn, Cd)Se/ZnSe quantum wells [29].

3.3. Biexcitonic emission in low excitation power

We then tried to observe biexcitonic emission at extremely low excitation power. Figure 3.6 shows a PL spectrum of WS_2/hBN at 81.7 K, using a 2.54 eV CW laser with

an input power of 2.8 μW or 240 W/cm^2. As shown in the figure, biexcitonic emission is shown in this energy region. Compared with a previous report, these conditions represent an extremely low excitation power (about 18 or 100 times lower than in the previous report) [21,22].

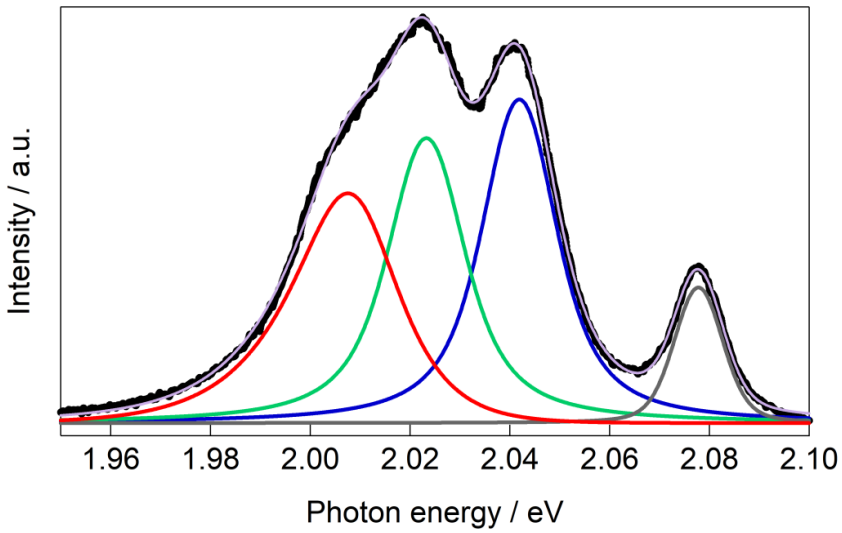

Figure 3.6. PL spectrum of WS_2/hBN at 81.7 K.

Since the incident power is small, we must estimate the validity of this phenomenon. To form a biexciton, two excitons must collide. Then, we must compare the diffusion length of an exciton and the average exciton-exciton distance to estimate whether they can collide to form biexcitons. We can estimate the diffusion length of an exciton from the formula, $L = 2(D\tau_{EX})^{0.5}$, where D and τ_{EX} represent the diffusion coefficient and the lifetime of an exciton (15 ps). D can be estimated from the Einstein relation. Einstein relation is given as: $D \sim k_BT/M\Delta$ [2], where k_B, M, and Δ are the Boltzmann constant, the translational mass of a neutral exciton (~0.55 m_0 at K point), and homogeneous line width of neutral exciton (~3.2 meV). At 81.7 K, the estimated value of D is ~ 9.3 cm^2/s.

Then, L was calculated as ~ 240 nm. The average exciton-exciton distance is estimated from the carrier lifetime, the exciton generation rate ($2.5 \times 10^8/cm^2$), which is calculated from the absorption coefficient of WS_2 [30], The incident photon energy (2.54 eV), and the power (2.8 μW or 240 W/cm^2); we can estimate the exciton-exciton distance as 420 nm. This is comparable to the diffusion length of excitons. This indicates that biexcitons can exist even at a small excitation power. The small homogeneous line width of the PL emission from exciton means that in WS_2/hBN, the dephasing time of an exciton is long, and makes L longer up to 240 nm even within the short lifetime of an exciton. This long L would originate from decreasing the scattering significantly by the roughness of the substrate of the ultra-flat WS_2 sample in our WS_2/hBN.

Not only the flatness of the substrate, but the small number of localized states and free carriers in WS_2/hBN also encourage the formation of biexcitons. As shown in Figure 3(a), under higher excitation power, PL emission from localized states appeared at 1.8~2.0 eV [19] is suppressed. This strongly suggests that the number of localized states in our sample is smaller than that in previous reports [19]. Furthermore, as already discussed, in our sample, the number of free carriers is small. And this means that number of trion formation is reduced. Higher order excitons like biexcitons are formed when excitons are collided. And other processes of reducing the number of excitons like the formation of trions and localized excitons compete with the formation of these higher order excitonic states. The smaller number of localized states thus contributes to make observing biexciton states easy in our WS_2/hBN samples. The difference of this number of free carriers may originate from the substrates which we used. As discussed before, on hBN, there are no origin of trap centers such as dangling bonds, surface roughness and charged impurities like SiO_2/Si [31].

3.4. PL properties of WS_2 grown on other substrates

To compare with WS_2/hBN, we synthesized WS_2 on SiO_2/Si and sapphire (c-plane) directly. Figure 3.8(a) and (c) shows the temperature dependence of PL spectra from WS_2 grown on SiO_2/Si and sapphire. The blue shift with decreasing temperature originates from a temperature dependent bandgap change, which is also observed in WS_2 grown on hBN. The peak blue shift and calculated Varshni parameters are shown in Figure 3.9 and Table 3.4. As shown in Figure 3.7(b) and (d), although a shoulder is seen at around 2.0 eV, WS_2 grown on both substrates shows no additional peaks at 81.7 K. Excitation was done by 2.54 eV CW laser with input power of 240 or 480 W/cm^2.

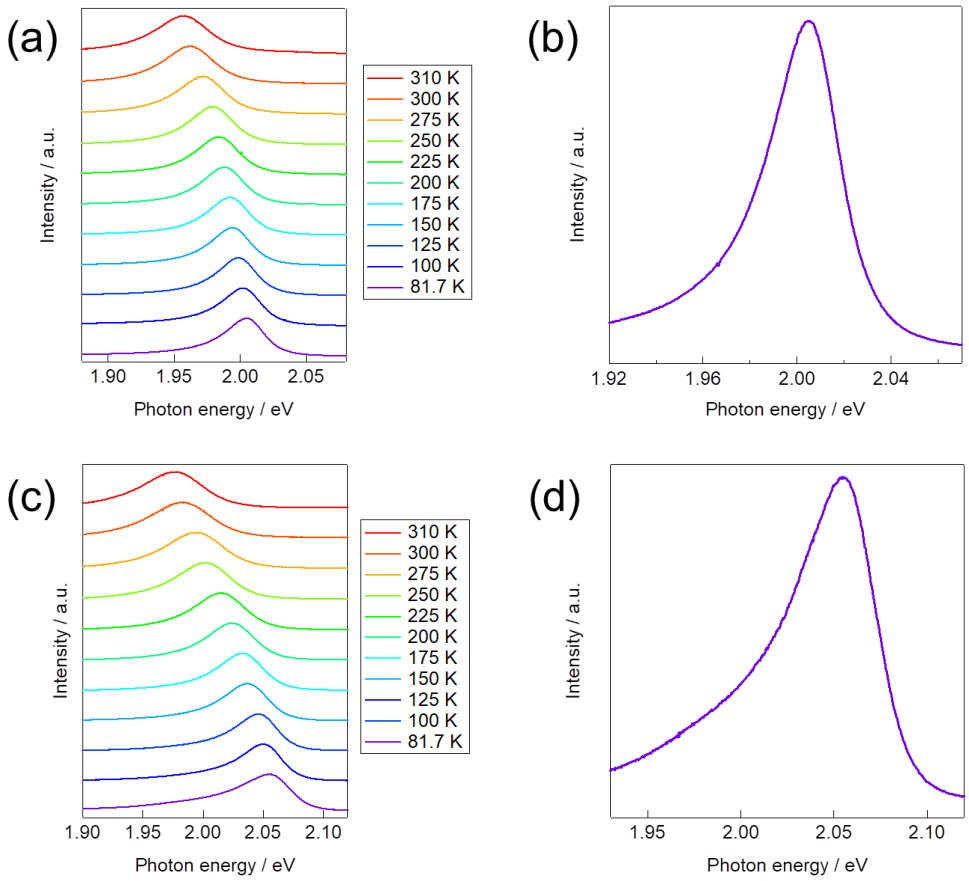

Figure 3.7. (a): Temperature dependence of PL properties of WS_2 grown on SiO_2/Si; (b): PL spectrum of WS_2 on SiO_2/Si at 81.7 K; (c) and (d): Those of WS_2 grown on a sapphire substrate.

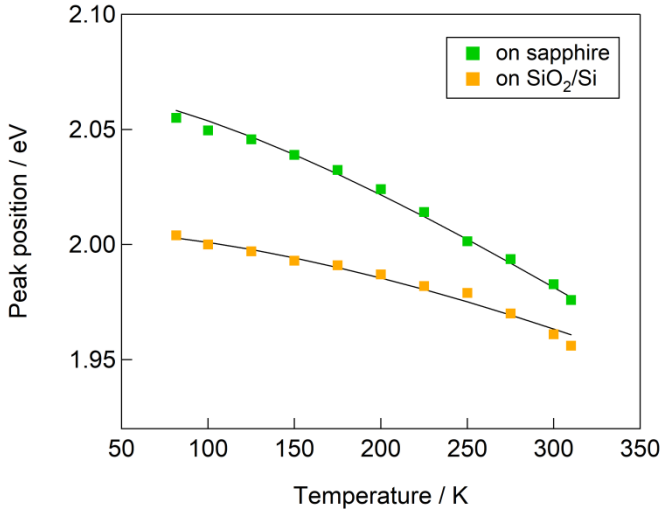

Figure 3.8. Exciton peak position and fitting with the Varshni equation (black line).

Table 3.4. Varshni plot.

Substrate	Parameter	
SiO_2/Si	α / eVK^{-1}	5.03×10^{-4}
	β / K	737
	E(0) / eV	2.01
Sapphire	α / eVK^{-1}	5.50×10^{-4}
	β / K	267
	E(0) / eV	2.07

This could be caused by the surface roughness of the substrate, which prevents excitons from diffusing sufficiently to form biexcitons. Thus, they show no additional peaks at this temperature.

3.5. Conclusion

In summary, we achieved high-quality WS_2 samples by direct CVD growth on hBN.

CVD-grown WS_2 on hBN exhibits PL emission from excitons, two types of trion, and biexcitons at 80 K. The excitation power dependence, lifetime, and circularly polarized excitation PL measurements are consistent with biexcitons existing in WS_2/hBN. In WS_2/hBN, biexcitons can exist under an extremely low excitation power of about 240 W/cm^2. We believe that this can be achieved with a minimal number of localization centers in our samples. These results clearly mean that the direct CVD growth method represents an excellent field for exploring novel optical physics in two dimensions.

3.6. References

[1] Z. Wang, J. Shan and K. F. Mak, ***Nat. Nanotechnol.***, 12, 144-149, (2017).

[2] S. Mouri, Y. Miyauchi, M. Toh, W. Zhao, G. Eda and K. Matsuda, ***Phys. Rev. B***, 90, 155449, (2014).

[3] A. Splendiani, L. Sun, Y. Zhang, T. Li, J. Kim, C. Y. Chim, G. Galli and F. Wang, ***Nano Lett.***, 10, 1271-1275, (2010).

[4] K. He, N. Kumar, L. Zhao, Z. Wang, K. F. Mak, H. Zhao and J. Shan, ***Phys. Rev. Lett.***, 113, 026803, (2014).

[5] K. F. Mak, C. Lee, J. Hone, J. Shan and T. F. Heinz, ***Phys. Rev. Lett.***, 105, 136805, (2010).

[6] H. R. Gutiérrez, N. Perea-López, A. L. Elías, A. Berkdemir, B. Wang, R. Lv, F. López-Urías, V. H. Crespi, H. Terrones and M. Terrones, ***Nano Lett.***, 13, 3447-3454, (2012).

[7] W. Zhao, Z. Ghorannevis, L. Chu, M. Toh, C. Kloc, P.-H. Tan and G. Eda, ***ACS Nano***, 7, 791-797, (2012).

[8] D. Y. Qiu, F. H. da Jornada and S. G. Louie, ***Phys. Rev. Lett.***, 111, 216805, (2013).

[9] A. Ramasubramaniam, ***Phys. Rev. B***, 86, 115409, (2012).

[10] K. F. Mak, K. He, C. Lee, G. H. Lee, J. Hone, T. F. Heinz and J. Shan, ***Nat. Mater.***, 12, 207-211, (2013).

[11] B. Zhu, X. Chen and X. Cui, ***Sci. Rep.***, 5, 9218, (2015).

[12] A. Chernikov, T. C. Berkelbach, H. M. Hill, A. Rigosi, Y. Li, O. B. Aslan, D. R. Reichman, M. S. Hybertsen and T. F. Heinz, ***Phys. Rev. Lett.***, 113, 076802, (2014).

[13] C. Mai, A. Barrette, Y. Yu, Y. G. Semenov, K. W. Kim, L. Cao and K. Gundogdu, ***Nano Lett.***, 14, 202-206, (2014).

[14] Y. You, X.-X. Zhang, T. C. Berkelbach, M. S. Hybertsen, D. R. Reichman and T. F. Heinz, ***Nat. Phys.***, 11, 477-481, (2015).

[15] J. Pei, J. Yang, X. Wang, F. Wang, S. Mokkapati, T. Lu, J. C. Zheng, Q. Qin, D. Neshev, H. H. Tan, C. Jagadish and Y. Lu, ***ACS Nano***, 11, 7468-7475, (2017).

[16] D. A. Kleinman, ***Phys. Rev. B***, 28, 871-879, (1983).

[17] S.-Y. Shiau, M. Combescot and Y.-C. Chang, ***Ann. Phys.***, 336, 309-330, (2013).

[18] Z. Ye, T. Cao, K. O'Brien, H. Zhu, X. Yin, Y. Wang, S. G. Louie and X. Zhang, ***Nature***, 513, 214-218, (2014).

[19] J. Shang, X. Shen, C. Cong, N. Peimyoo, B. Cao, M. Eginligil and T. Yu, ***ACS***

Nano, 9, 647-655, (2015).

[20] Z. He, W. Xu, Y. Zhou, X. Wang, Y. Sheng, Y. Rong, S. Guo, J. Zhang, J. M. Smith and J. H. Warner, ***ACS Nano***, 10, 2176-2183, (2016).

[21] G. Plechinger, P. Nagler, J. Kraus, N. Paradiso, C. Strunk, C. Schüller and T. Korn, ***Phys. Status Solidi RRL***, 9, 457-461, (2015).

[22] M. S. Kim, S. J. Yun, Y. Lee, C. Seo, G. H. Han, K. K. Kim, Y. H. Lee and J. Kim, ***ACS Nano***, 10, 2399-2405, (2016).

[23] M. Nakayama, K. Suyama and H. Nishimura, ***Phys. Rev. B***, 51, 7870-7873, (1995).

[24] A. A. Mitioglu, P. Plochocka, J. N. Jadczak, W. Escoffier, G. L. J. A. Rikken, L. Kulyuk and D. K. Maude, ***Phys. Rev. B***, 88, 245403, (2013).

[25] Y. P. Varshni, ***Physica***, 34, 149-154, (1967).

[26] J. C. Kim, D. R. Wake and J. P. Wolfe, ***Phys. Rev. B***, 50, 15099-15107, (1994).

[27] D. Birkedal, J. Singh, V. G. Lyssenko, J. Erland and J. M. Hvam, ***Phys. Rev. Lett.***, 76, 672-675, (1996).

[28] L. Wang and J. H. Simmons, ***Appl. Phys. Lett.***, 67, 1450-1452, (1995).

[29] R. Spiegel, G. Bacher, A. Forchel, B. Jobst, D. Hommel and G. Landwehr, ***Phys. Rev. B***, 55, 9866-9871, (1997).

[30] N. Peimyoo, J. Shang, C. Cong, X. Shen, X. Wu, E. K. L. Yeow and T. Yu, ***ACS Nano***, 7, 10985-10994, (2013).

[31] J.-H. Chen, C. Jang, S. Xiao, M. Ishigami and M. S. Fuhrer, ***Nat. Nanotechnol.***, 3, 206-209, (2008).

Chapter 4

4.Fabrication and optical properties of hBN-encapsulated WS_2/MoS_2 van der Waals heterostructures

4.1. Introduction

2D vdW heterostructures, especially those based on the TMDC, offer great opportunities for exploring properties at the 2D limit [1-4]. As discussed in Chapter 1, TMDC are direct-gap semiconductors, and, because of their large binding energy, excitons dominate their optical response [5-7]. Many recent papers have shown that TMDC and various 2D materials like graphene and hBN can be fabricated into vdW heterostructures with various sequences [8-11]. These various compounds of 2D vdW heterostructures suggest that we can design 2D vdW heterostructures with desired electronic band structure and physical properties of 2D heterostructures.

Recent studies of interlayer excitons in type-II vdW heterostructures of TMDC show an excellent opportunity to explore the basic physics of two-dimensional excitons and the valley degree of freedom of them. As shown in Chapter 1, monolayer 2H-phase TMDC have two unequal valleys at the K and K′ points in their electronic band structure, and these unequal K and K′ points makes the valley degree of freedom [12]. In TMDC with odd numbers of such layers, excitation by circularly polarized light can

create photoexcited carriers at the K or K′ points, resulting in valley-polarized 2D excitons [12-14]. These valley polarized excitons and carriers in TMDC can also be observed in TMDC-based vdW heterostructures like $WSe_2/MoSe_2$ and WSe_2/MoS_2 [1,3]. Recent reports of vdW heterostructures based on TMDC with type-II band alignment have shown that interlayer excitons—that is, excitons that occur in materials with electrons and holes in different layers—can be formed in such systems [2,9,15,16]. Compared with intralayer excitons in monolayer TMDC [17-19], interlayer excitons tend to have a much longer lifetime (~138 ns) [15] and a longer valley depolarization lifetime (~39 ns) [3]. These properties strongly indicate that heterostructures based on TMDC with type-II band alignment are excellent platforms for exploring exotic 2D excitonic effects and realizing "valleytronics" technologies by controlling the valley degree of freedom.

To explore basic physics of 2D excitons and the possibility for optic and optoelectronic applications of a heterostructure based on TMDC with type-II band alignment, we need to understand the interlayer excitons that appear in this system. TMDC are multivalley semiconductors in which intravalley and intervalley excitons (electrons and holes located at the same or different valleys) can be formed by photo excitation [13]. In the heterostructures, interlayer interactions can make electronic band different. This make the energies of the valence-band maximum (VBM) and the conduction-band minimum (CBM) different from that of monolayers [20]. As a result, not only K and K′ valleys, other valleys, including Γ and Q or T valleys (point between Γ and K point), can contribute to optical transitions [16,21,22]. Furthermore, as shown in Chapter 1, stacking angle of heterostructures based on TMDC causes different electronic band structures [21,23]. Therefore, various interlayer excitons can occur in

vdW heterostructures based on TMDC, and these interlayer excitons can show various optical properties [16,24,25]. In previous reports, interlayer exciton peaks in the PL spectra of a WS_2/MoS_2 heterostructure originate from interlayer excitons corresponding to K–K (direct transition) and K–Γ transitions (indirect transition) [26]; however, further theoretical analysis and spectroscopic characterization and are necessary to determine the origin of these PL spectrum.

Here, we report observations and peak identification of three different PL emissions from interlayer excitons in the PL spectra of a WS_2/MoS_2 heterostructure, which show type-II band alignment. To observe fine structures in PL emission from interlayer excitons, we use hBN flakes as an overlayer and substrate to form an hBN-encapsulated WS_2/MoS_2 sample, i.e., hBN/WS_2/MoS_2/hBN (Figure 4.1),

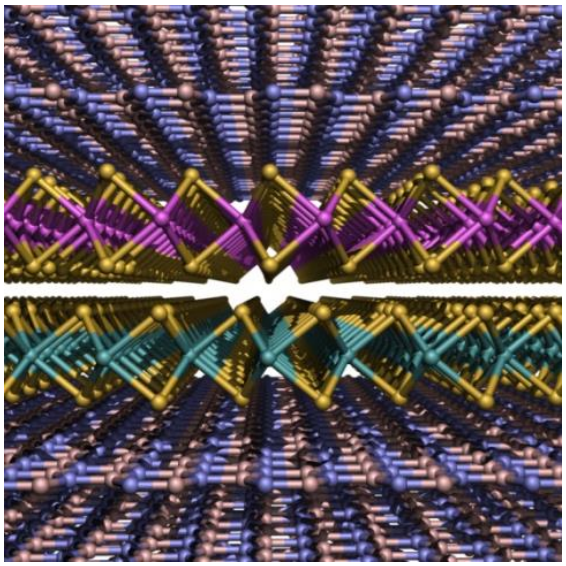

Figure 4.1. A schematic image of the hBN/WS_2/MoS_2/hBN heterostructure. Yellow, magenta, cyan, pink, and light-blue correspond to sulfur, tungsten, molybdenum, boron, and nitrogen atoms, respectively.

As discussed in Chapters 2 and 3, hBN is an atomic layered dielectric material

without dangling bonds on its surface, and it can protect WS_2/MoS_2 from substrate effects such as inhomogeneous broadening of optical transitions, which is caused by some substrate effect like charged impurities and surface roughness [27]. In addition, we have fabricated the heterostructures with controlled the stacking angle, which has important effects on its properties. As previously mentioned, the electronic band structure of WS_2/MoS_2 strongly depends on its stacking angle. Therefore, controlling the stacking angle of heterostructure is very important to assign the origin of interlayer excitons. In general, the dry-transfer method with TMDC crystals which obtained by the mechanical exfoliation method and CVD growth method are used to fabricate these vdW heterostructures [2,9]. In general, exfoliated samples, which are generally used in the typical dry-transfer method, enable control of the stacking angles in the stacking sequence [3]; however, estimating their crystallographic orientation is difficult. In previous studies, second-harmonic-generation microscopy has been used to determine the crystallographic orientation of exfoliated samples [3]. By contrast, in CVD-grown TMDC samples, their crystallographic orientation can be estimated from their crystal shape [28,29]; however, their stacking angle cannot be controlled. In the present work, we developed a new and simple method: direct peeling off and dry transfer of CVD-grown samples. We estimated the crystallographic orientation of WS_2 and MoS_2 obtained by CVD growth by optical microscopy; by transferring the samples through the dry-transfer method, we successfully fabricated stacking-angle-controlled heterostructures. Typical PL spectrum of hBN/WS_2/MoS_2/hBN with a stacking angle of ~60° shows three peaks at 1.3 to 1.7 eV at room temperature. By comparing the results of time resolved PL intensity and PL excitation (PLE) measurements and theoretical calculations, we concluded that the three peaks originate from (1) K–K interlayer

excitons (direct transition), (2) Q–Γ interlayer excitons (indirect transition), and (3) K–Γ interlayer excitons (indirect transition). These results play an important role for understanding the optical and optoelectrical physics of TMDC-based vdW heterostructures.

4.2. Fabrication

As previously mentioned, we developed a new method for fabricating vdW heterostructures. First, we grew WS_2 and MoS_2 crystals on sapphire and hBN, respectively. We then used these crystals to fabricate hBN/WS_2/MoS_2/hBN heterostructures through the dry-transfer method.

4.2.1. CVD growth

WS_2 crystals were grown on sapphire (*c*-plane or the (0001) surface) through the CVD growth method. A schematic of the CVD setup is shown in Figure 4.2.

Before CVD growth, we deposited pure tungsten (Nilaco, 99.98%) onto the sapphire substrate partially by sputtering (Sanyu Electron SC-701 MkII Advance). Then, we deposited elemental sulfur (Sigma-Aldrich, 99.98%) onto the W-coated substrate in a quartz tube. With the samples under Ar flowing at 400 sccm, the quartz tube was heated for 60 min in a three-zone furnace with the three zones at 221, 400, and 900 °C. The sulfur and substrate were placed in the coldest and hottest zones, respectively.

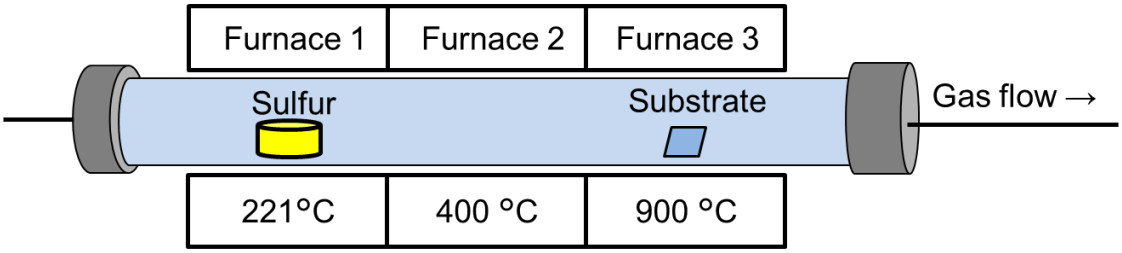

Figure 4.2. Setup for CVD growth of WS_2/sapphire.

Figure 4.3 shows a typical optical microscope image (Leica DM 2500 M) and PL spectrum (obtained using a Renishaw InVia Raman microscope) of grown WS_2 at room temperature. Excitation was performed using a 2.54 eV continuous-wave (CW) laser (COHERENT Sapphire 488 LP). The PL emission spectrum with a single peak at approximately 2 eV strongly indicates that the obtained WS_2 crystal was a monolayer [29].

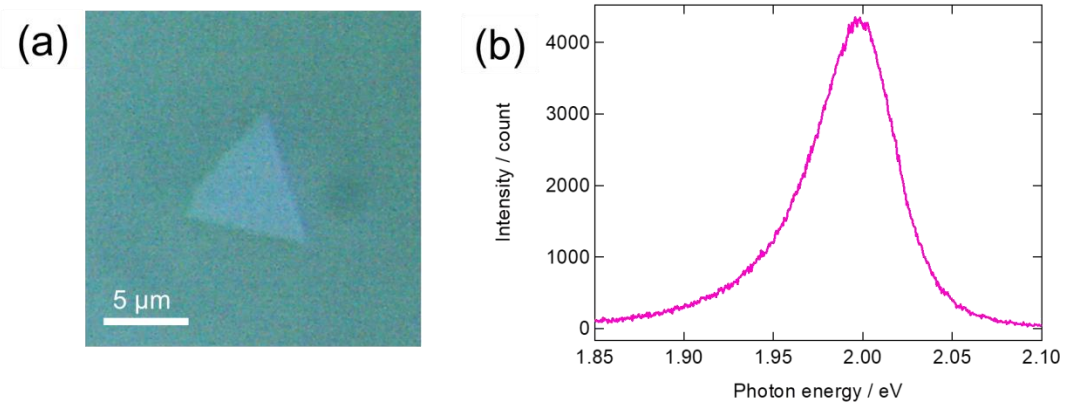

Figure 4.3. (a) A typical optical image of WS_2 on sapphire; (b): the PL spectrum of obtained WS_2 crystal shown in (a).

Second, we grew monolayer MoS_2 by the CVD method using elemental sulfur (Sigma-Aldrich, 99.98%) and molybdenum (VI) oxide (MoO_3, Sigma-Aldrich, 99.5%) as precursors. As a substrate for the CVD growth of monolayer MoS_2, by the

mechanical exfoliation method, we prepared thin hBN flakes on a quartz substrate. All hBN flakes were synthesized by the HPHT method [30]. A schematic image of the CVD setup is shown in Figure 4.4.

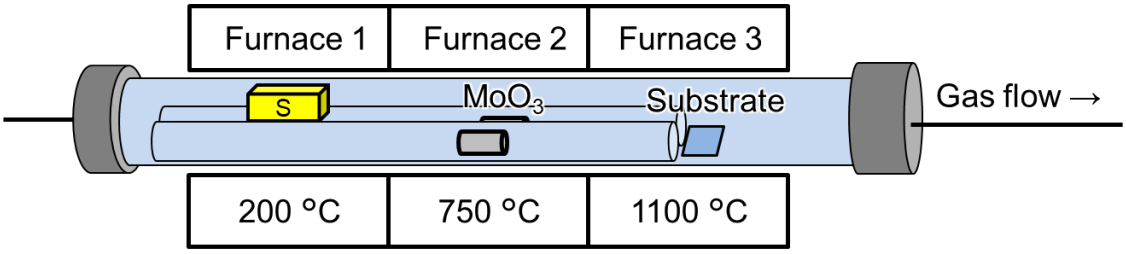

Figure 4.4. A schematic image of CVD growth.

We putted sulfur, MoO_3, and quartz substrate with hBN flakes in a quartz tube. We putted MoO_3 in an inner quartz tube (inner diameter was 10 mm) to avoid sulfurization. With Ar flowing at 200 sccm, we heated the quartz tube for 20 min in a three-zone furnace with the three zones at 200, 750, and 1,100 °C. An optical image and room-temperature PL spectrum of the obtained MoS_2 are shown in Figure 4.5.

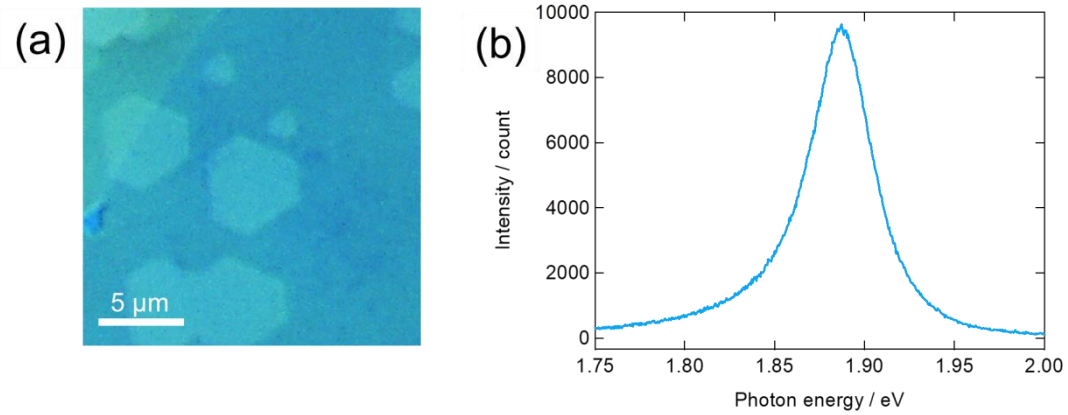

Figure 4.5. (a): A typical optical image of MoS_2 on sapphire. Hexagonal-shaped contrasts correspond to MoS_2 flakes; (b): the PL spectrum of the obtained MoS_2 crystal shown in (a).

The obtained MoS_2 crystal shows strong, single-peak PL emission around 1.89 eV, indicating that the grown MoS_2 is a monolayer [31].

4.2.2. The dry transfer method

Finally, we fabricated the heterostructures. We used a homemade micromanipulation system (with SIGMAKOKI stepper motors) with an optical microscope to fabricate the heterostructures (Figure 4.6). A schematic of the fabrication method is shown in Figure 4.7.

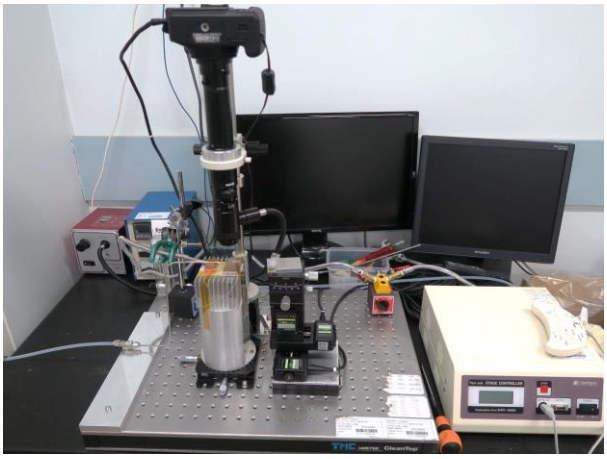

Figure 4.6. A photograph of the homemade micromanipulation system.

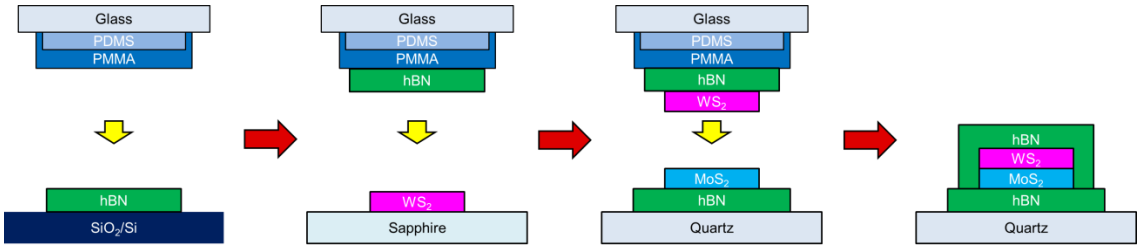

Figure 4.7. A schematic of the fabrication procedure.

First, hBN flakes, which we used as a top layer, were prepared on heavily p-doped 100 nm SiO_2/Si substrates using the mechanical exfoliation method. At first, we picked

the hBN flakes on the SiO_2/Si substrate up on by PMMA (Microchem 495 PMMA A11)/PDMS (Shin-Etsu Silicone KE-106) film on a glass slide. Then, we picked a monolayer WS_2 flake grown on a sapphire substrate up with the hBN/PMMA/PDMS film. Then, we transferred prepared stacked structure, WS_2/hBN/PMMA/PDMS, onto a MoS_2/hBN on a quartz substrate to fabricate a hBN/WS_2/MoS_2/hBN. To make good interlayer contact, we heated all of the substrate during the transfer process. Finally, we removed the PMMA/PDMS film from the fabricated heterostructure by cooling the substrate. After fabricating samples, we heated samples at 200 degree over 10 hours under ~10^{-3} Pa.

In this chapter, unless otherwise specified, all measurements were performed on hBN/WS_2/MoS_2/hBN samples with a stacking angle of 60° (like 2H stacking of a homobilayer).

4.3. Optical properties of hBN/WS_2/MoS_2/hBN at room temperature

To estimate whether the interface between WS_2 and MoS_2 was clean, we characterized some basic optical properties of the hBN/WS_2/MoS_2/hBN heterostructure. In this section, we report the Raman and PL spectra of the fabricated heterostructures and discuss the interface between WS_2 and MoS_2.

4.3.1. Raman spectrum and PL image

Figure 4.8 shows a typical Raman spectrum of heterostructures measured at room temperature using 2.54 eV CW laser excitation (Horiba Jovin Yvon LabRAM HR-800

with COHERENT Sapphire 488 LP). The spectrum in Figure 4.8 shows four main peaks at 356.7 (with a shoulder at the low-frequency side), 384.6, 405.7, and 418.6 cm^{-1}. These peaks are consistent with the Raman mode of monolayer MoS_2 and WS_2, assigned as E′ and A'_1 mode [32-34]. Shoulder of the E′ mode of the WS_2 originates from 2LA(M) mode.

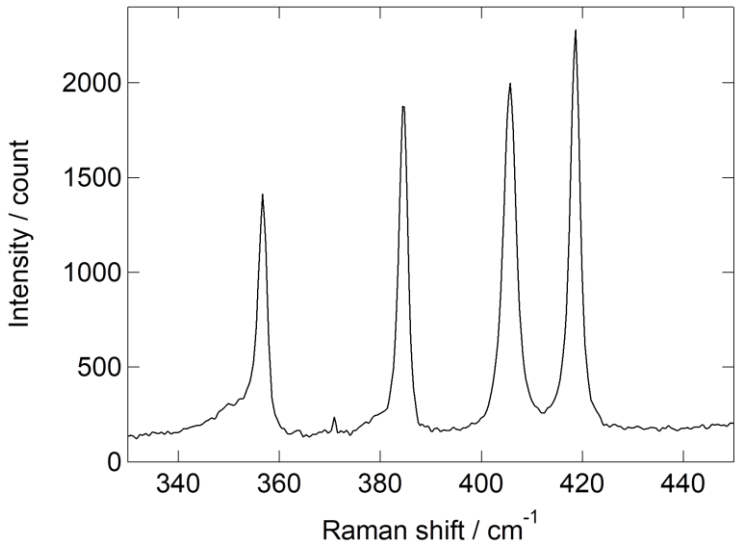

Figure 4.8. Typical Raman spectrum of hBN/WS_2/MoS_2/hBN at room temperature.

Because WS_2/MoS_2 heterostructures are indirect-gap semiconductors as a consequence of their interlayer coupling and due to the charge transfer, their PL intensity is weaker than those of monolayers [35,36]. As shown in the PL image obtained using a fluorescence microscope (Leica TCS SP8 gSTED, excitation by a supercontinuum laser operating at 2.54 eV) (Figure 4.9), PL emission from the stacked region is quenched, which indicates that strong interlayer coupling exists. Thus, the interface between WS_2 and MoS_2 in the fabricated heterostructure is sufficiently clean to couple these two layers.

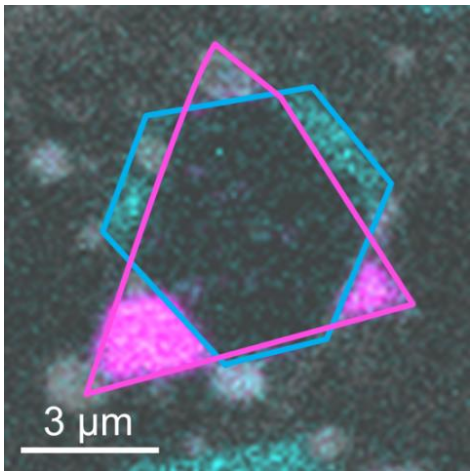

Figure 4.9. PL image of hBN/WS_2/MoS_2/hBN at room temperature. This image combines a transmission bright-field image (monochrome) as well as 1.97–2.07 eV (magenta, PL emission from monolayer WS_2) and 1.71–1.91 eV (cyan, PL emission from monolayer MoS_2) detection. The magenta and cyan lines show the edges of WS_2 and MoS_2 crystals, respectively.

The aforementioned strong interlayer coupling is also observed in the low-frequency Raman spectrum. Figure 4.10 shows the low-frequency region of the Raman spectrum collected at room temperature.

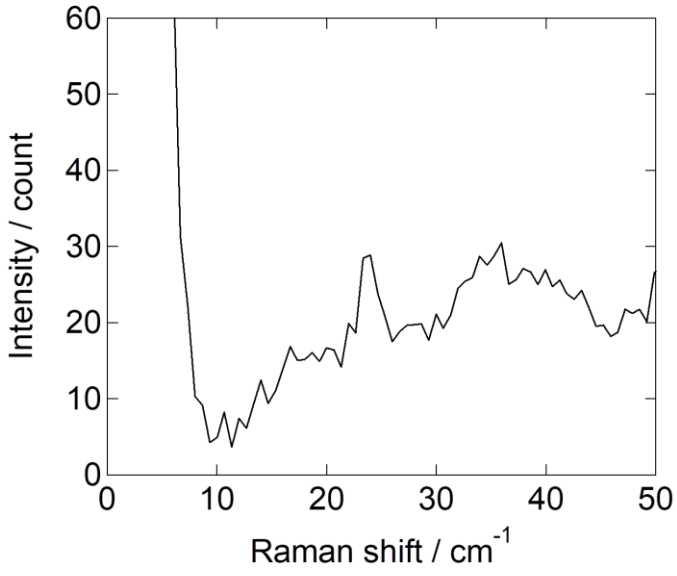

Figure 4.10. The low-frequency Raman spectrum of hBN/WS_2/MoS_2/hBN collected at room temperature.

As shown in the figure, the shear and breathing interlayer vibrational modes [35] are clearly observed at 23.7 and 35.5 cm^{-1}, respectively. These interlayer modes require strong layer–layer coupling in WS_2/MoS_2, thus indicating that the interface between the monolayers is clean [37]. Therefore, the full dry-transfer method we used can produce a clean heterostructure interface.

4.3.2. PL spectrum

To further characterize the hBN/WS_2/MoS_2/hBN heterostructure, we recorded the PL spectrum at room temperature using 2.54 eV CW laser excitation (Renishaw InVia Raman microscope and COHERENT Sapphire 488 LP). The obtained spectrum is shown in Figure 4.11.

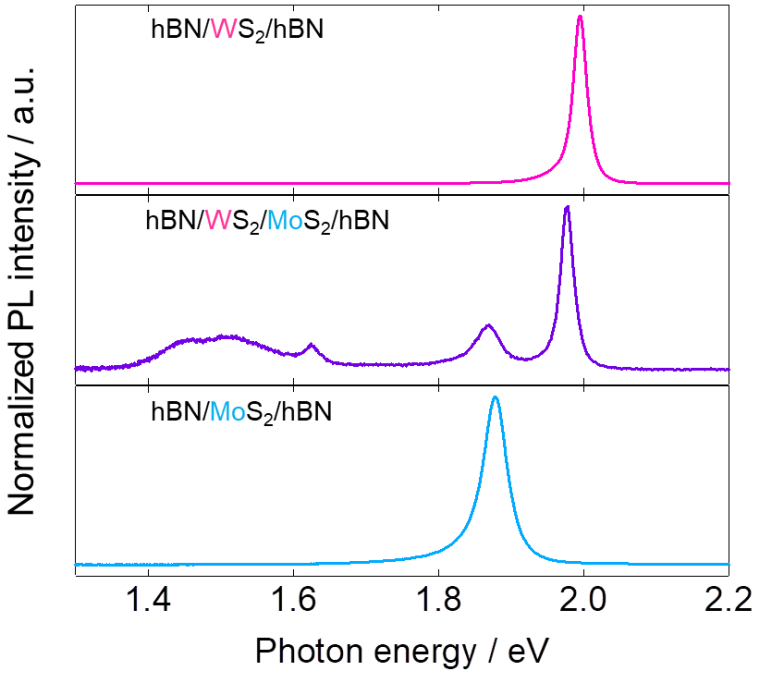

Figure 4.11. Room-temperature PL spectra of hBN/WS_2/hBN, hBN/WS_2/MoS_2/hBN, and hBN/MoS_2/hBN heterostructures.

In Figure 4.11, PL emissions from intralayer excitons in the WS_2 and MoS_2 samples are observed at 2.00 and 1.88 eV, respectively [29,31]. In addition, the PL spectrum of the heterostructure shows additional PL peaks at energies substantially lower than those of intralayer excitons, which range from 1.3 to 1.7 eV. These additional peaks are observed only in the spectra of the heterostructure samples [9,26], and we hypothesize that these PL emission are originate from interlayer excitons.

4.4. Identification of interlayer excitons from hBN/WS_2/MoS_2/hBN

4.4.1. Peak deconvolution

Figure 4.12 shows the lower-energy side of the the hBN/WS_2/MoS_2/hBN heterostructure, with the peaks deconvoluted. Deconvolution of the peaks revealed three peaks at 1.63, 1.52, and 1.44 eV. We referred to as I_1, I_2, and I_3 in the following discussion, respectively.

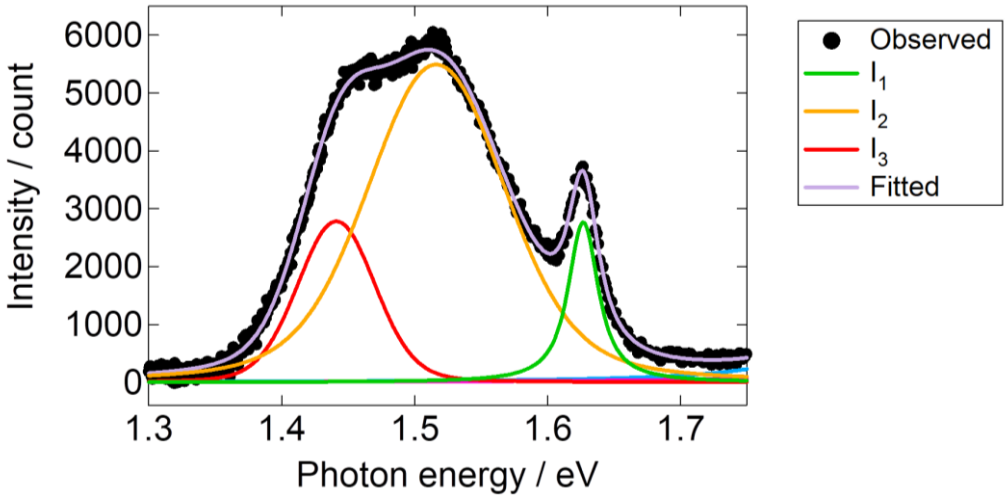

Figure 4.12. PL spectrum of the hBN/WS_2/MoS_2/hBN heterostructure with deconvolution, with an excitation energy of 2.33 eV. We modeled the contributions from I_1, I_2, and I_3 using Voigt functions, which are plotted at green, orange, and red curves, respectively.

4.4.2. PL diffusion

In this spectral region, there is possibility that these features are from bound excitons which trapped at defect sites or impurities. To exclude the possibility of this, we measured the diffusion lengths of exciton by taking PL images captured at room temperature using a homemade PL measurement system equipped with a supercontinuum laser system (NKT Photonics SuperK EXTREME). The beam from the supercontinuum laser was monochromated by a spectrometer (Princeton Instruments SP2150i). Detection was carried out by an electron-multiplying charge-coupled device sensor (Princeton Instruments). Since bound excitons are localized around defects or trapped centers, the diffusion length of these bound excitons should be nearly zero. On the other hand, free excitons can diffuse even micrometers [38,39]. Figure 4.13 (a), (c), and (e) show a PL image of I_1, I_2, and I_3 in WS_2/MoS_2. Figure 4,13 (b), (d), and (f) show corresponding cross-sectional profile, respectively. The inset of Figure 4.13 (a), (c), and (e) is an image of the excitation laser beam. Its corresponding cross-section profile is also shown in Figure 4.13(b), (d), and (f); the excitation energy was 2.43 eV.

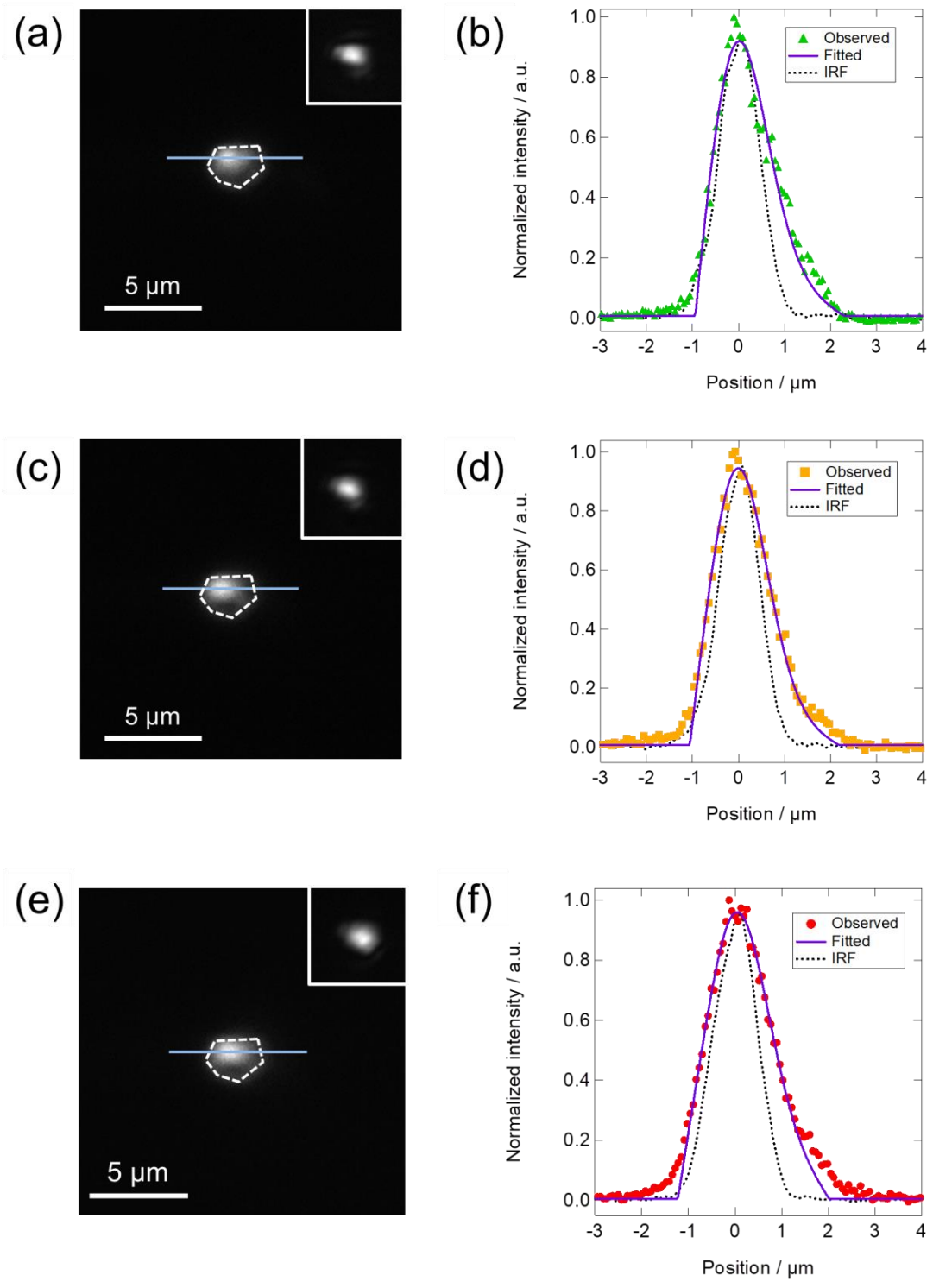

Figure 4.13. (a): A typical PL image of I_1 in the hBN/WS_2/MoS_2/hBN heterostructure. Excitation was done by a 2.43 eV light at a power density of 1.5 μJ/cm^2. The white dotted line shows the edge of the sample. The inset shows the image of incident laser beam; (b): Cross-sectional profile of the PL image of the hBN/WS_2/MoS_2/hBN heterostructure and

excitation laser (impulse response function (IRF)) for I_2 ((c) and (d)) and I_3 ((e) and (f)).

Figure 4.13 clearly shows that all of the PL images are broader than the corresponding excitation laser beam. This strongly suggests that photo excited excitons diffuse along the heterostructures. The broadening of the PL images is not only from exciton diffusion but also from the diffraction limit and the laser spot size of the sample. We fitted the cross sectional profile of the PL images under approximation of 2D diffusion with the following diffusion equation with a decay term:

$$\frac{\partial}{\partial t}N(x,y,t) = D\left(\frac{\partial^2}{\partial x^2}+\frac{\partial^2}{\partial y^2}\right)N(x,y,t) - \frac{1}{\tau}N(x,y,t) \qquad (4.1)$$

where $N(x,y,t)$, D, τ, t, and x correspond to the number of excitons, the diffusion constant of interlayer excitons, the corresponding lifetime of the interlayer excitons, time, and position, respectively. The only unknown parameter in this equation is D because τ can be determined by time-resolved PL measurements (see Section 4.4.4). Assuming that the number of excitons is proportional to the PL intensity in the obtained PL images ($I(x)$), solving this equation give us the value of D. Assuming that initial condition is given as broadening from the diffraction limit and the laser spot, which can be modeled as a Gaussian function, $\sigma^2 = \sigma_{size}{}^2 + \sigma_{diff}{}^2$. Parameter of the spot size of excitation laser σ_{size} can be directly measured from the image of the excitation laser spot. And diffusion from diffraction limit σ_{diff} is approximated as $0.21\lambda/N_A$, where λ and N_A correspond to the wavelength of PL and numerical aperture of the objective lens, respectively [40]. We solved equation (4.1) numerically; we used values of λ = 1.6, 1.5, and 1.4 eV for I_1, I_2, and I_3 respectively as well as N_A = 0.7. We obtained D values of 50, 15, and 30 cm^2/s for I_1, I_2, and I_3, respectively. The diffusion length $L = \sqrt{D\tau}$ of I_1, I_2, and I_3 can be calculated as 760, 560, and 850 nm, respectively, which are consistent

with mobile electrons but not with bound excitons.

4.4.3. DFT calculations

We calculated the electronic band structure of WS_2/MoS_2 heterostructures using DFT to assign the origin of the I_1–I_3 peaks. We used a stacking angle of 60° in these calculations.

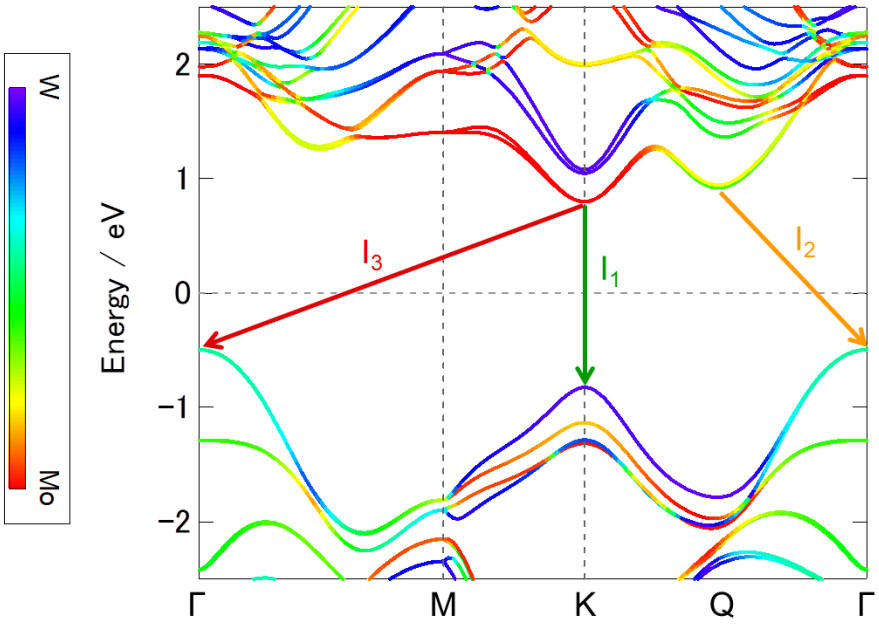

Figure 4.14. The band structure of the WS_2/MoS_2 heterostructure calculated through DFT. Color scale corresponds to the contribution of the each layers.

As shown in the obtained band structure (Figure 4.14), VBMs are located at the Γ point which originates from MoS_2 and WS_2, whereas CBM is located at the K point which originates from MoS_2. This structure suggests that after relaxation, photoexcited carriers should form interlayer excitons in this heterostructure. In this system, four valleys, the valleys located at the K and Q points in the conduction band and the valleys

located at the K and Γ points in the valence band can contribute to optical transitions. Spectral shape of I_1–I_3 indicates the origin of them. Table 4.1 lists the FWHM and ratio of Gaussian component and Lorentzian component of I_1–I_3. Peak fitting was done using Voigt functions.

Table 4.1. FWHM and ratios of the Gaussian and Lorentzian components of interlayer excitons fitted with Voigt functions.

Peak	FWHM/meV	Ratio of Gaussian/Lorentzian FWHM
I_1	27	3.7×10^{-1}
I_2	123	2.8
I_3	69	6.3

As shown in Table 4.1, the FWHM and the ratio of Gaussian component and Lorentzian component of I_2 and I_3 are much larger than those of I_1. This difference strongly indicates that a broadening factor is associated with the I_2 and I_3 peaks like phonon emission and absorption. And considering the energy differences between the K, Γ, and Q valleys, we conclude that I_1, I_2, and I_3 originate from K–K direct transition, Q–Γ indirect transition, and K–Γ indirect transition, respectively.

To obtain more information of the origin of these interlayer excitons, we calculated the imaginary part of the dielectric function for monolayer WS_2, MoS_2, and the WS_2/MoS_2 heterostructure (Figure 4.15).

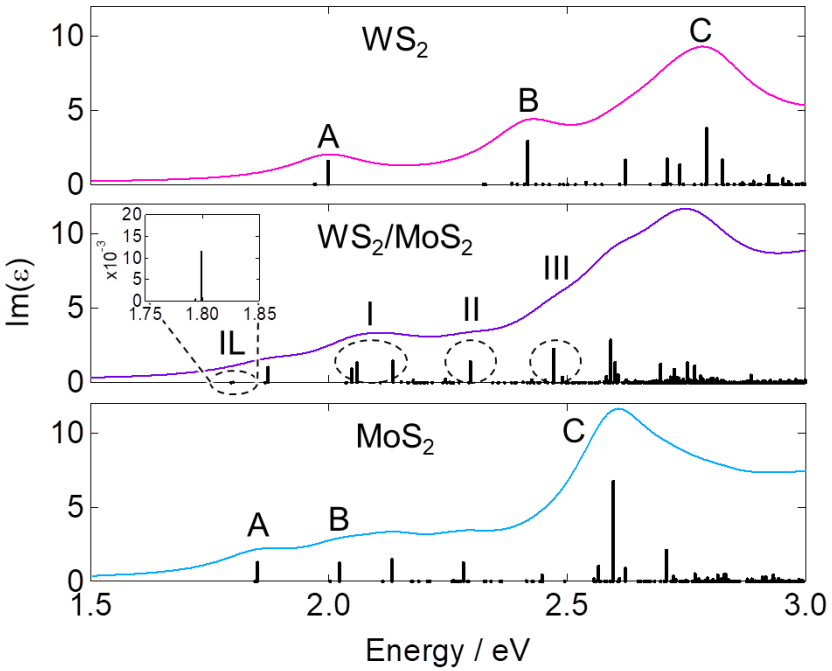

Figure 4.15. Calculated imaginary part of the dielectric functions of monolayer WS_2 (top), MoS_2 (bottom), and heterostructure (middle). Vertical bars denote oscillator strengths at transition energy.

To determine the electron–hole interactions and the quasiparticle energies in these excitonic systems correctly, we solved the Bethe–Salpeter equation with G_0W_0. Peaks in Im(ε) would be appeared in the absorption spectra of materials. Calculated A exciton peak in monolayer WS_2 and MoS_2 is appeared at ~2.0 and ~1.85 eV. These values are very similar to the PL emission from intralayer excitons (Figure 4.11).

We also calculated binding energies for the A exciton peak. The values of them are ~0.45 and ~0.55 eV for WS_2 and MoS_2, respectively. In addition, the calculated peak positions of the B and C excitons consistent to those in previous reports [41,42]. Absorption spectrum and oscillator strength of the heterostructure which we calculated shown in Figure 4.15 is not simply a superposition of the those of the monolayer WS_2 and MoS_2. The peak positions in the spectrum of the heterostructure are slightly shifted

compared to those in the spectra of the individual WS_2 and MoS_2 monolayers. Also, the obtained absorption spectrum for the heterostructure shows the feature from the interlayer transitions. An interlayer excitonic transition is observed in Figure 4(b) at 1.79–1.80 eV. This interlayer transition peak was also appeared in a previous study on the calculating optical transition of the heterostructures [42]. Since electrons and holes are separated spatially, overlap of the wave functions of hole and electron are small. Then, the oscillator strength which we calculated of this interlayer exciton transition is only 1.3% of that of the exciton transition from intralayer excitons in MoS_2. And we calculated a quasiparticle bandgap of the heterostructure. Obtained bandgap is 2.06 eV, and we estimated the interlayer exciton binding energy of 0.27 eV. This value is a similar to that of the A excitons of WS_2 and MoS_2.

The obtained absorption spectrum of interlayer excitons in our calculation is blue-shifted than that of observed in the experimental result (Figure 4.11). The shift is most likely due to the Franck–Condon (FC) shift in the heterostructure. In the heterostructures, FC corrections are not negligible unlike those of monolayers. In previous studies, a significant FC shift is observed in the MoS_2/WSe_2 heterostructure experimentally [43]. Our calculations confirm this result. To calculate the FC shift associated with the interlayer excitation of an electron from WS_2 to MoS_2, we used the constrained-occupation DFT (cDFT) method [44,45]. Figure 4.16 shows a standard protocol.

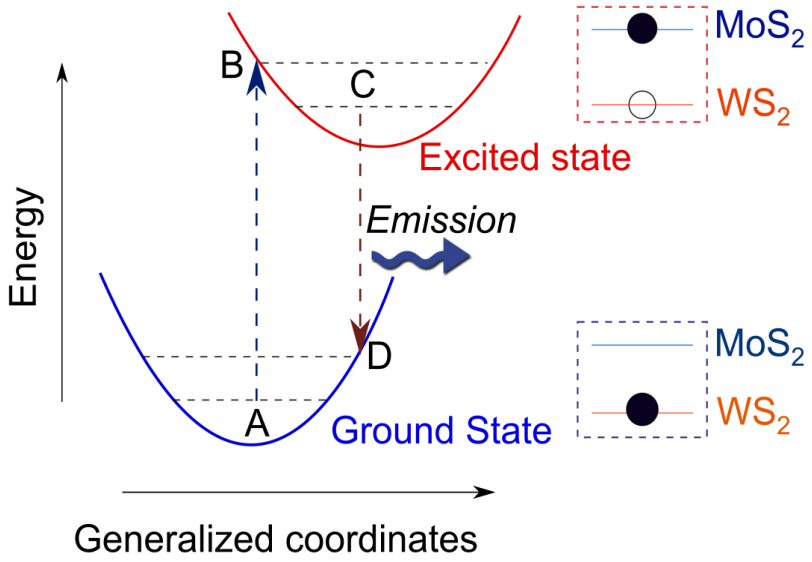

Figure 4.16. A schematic of the FC shift in the heterostructure. The red and blue parabolic curves correspond to the total adiabatic state energy (electronic + vibration) vs. the configurational coordinate for the excited and grand states, respectively. The square boxes at right of the state represent the occupancy of the conduction and valence bands in WS_2 and MoS_2, respectively. The mechanism of recombination is following: 1) The ground-state electron (e^-) (point A) is excited from WS_2 to MoS_2, leaving a hole (h^+) in WS_2 (point B); 2) e^- are relaxed into point C; 3) The e^- from MoS_2 recombined with the h^+ in WS_2 by emitting a photon (point D).

At the excited electronic state, h^+ and e^- are separated on WS_2 and MoS_2, respectively. This was calculated by fixing the occupation of the bands using cDFT. The configuration coordinate diagram was obtained by relaxing positions of the nuclei after the band occupation was fixed in the excited and ground states. The value of FC shift is given by the energy difference between emission ($E_C - E_D$) and absorption ($E_B - E_A$). In our calculations, 0.12 eV of a FC shift was obtained. Therefore, in our calculations, the interlayer emission peak would be appeared at 1.68 eV. This value of emission peak is well match with the experimental result, the I_1 peak is appeared at 1.63 eV (Figure 4.11). This result demonstrates the interlayer origin of the transition. Thus, to describe the emission spectra of interlayer excitons correctly, the FC shift must be considered. And

in this calculation, only direct transitions are represented. This means that in the calculated optical spectrum of WS_2/MoS_2, direct interlayer transition would be appeared at single peak around 1.68 eV. This result is consistent with our assignment that I_1 arises from direct transitions, whereas I_2 and I_3 originate from indirect transitions.

4.4.4. Time resolution of PL

Then, we measured time-resolved PL intensities of interlayer excitons at room temperature. Figure 4.17 plots the results.

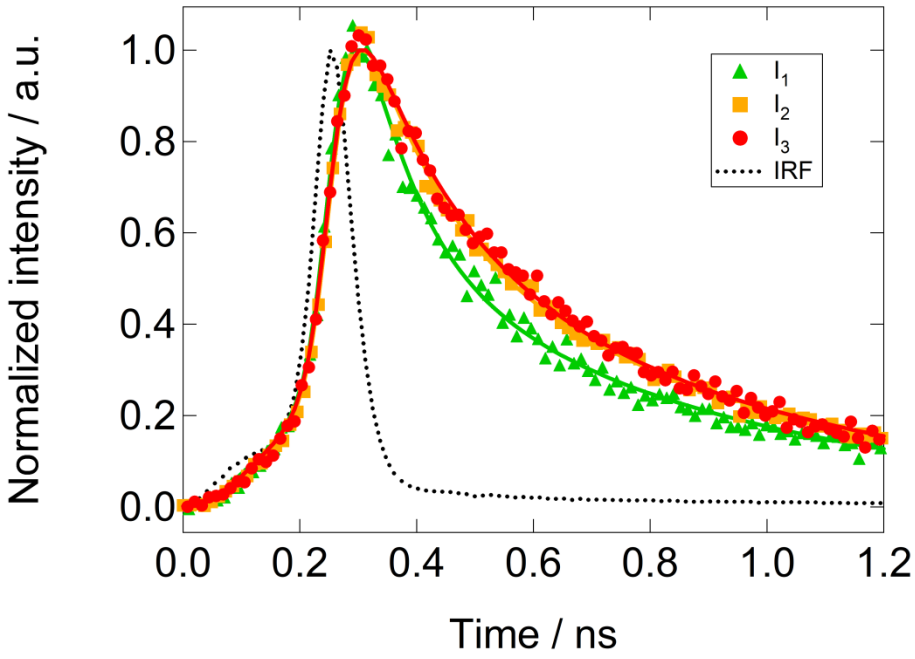

Figure 4.17. Time-resolved PL intensities of I_1, I_2, and I_3 of hBN/WS_2/MoS_2/hBN; the dashed line corresponds to the IRF.

For time-resolution PL measurement, we used the time-correlated single-photon counting module (Becker and Hickl SPC 130) and a supercontinuum laser (NKT

Photonics SuperK EXTREME) as a light source. We obtained lifetimes of I_1 (τ_1), I_2 (τ_2), and I_3 (τ_3) as 87 ± 3, 118 ± 3, and 132 ± 4 ps, respectively by fitting the experimental data to a double-exponential model. Thus, τ_1 is shorter than τ_2 and τ_3. This result is consistent with previous peak assignment that direct interlayer excitons should have shorter radiative decay lifetimes [16]. The obtained lifetime is about 100 picoseconds at room temperature. This value is shorter than the lifetime of interlayer excitons which previously reported at low temperatures in other heterostructures like $MoSe_2/WSe_2$ [2,15,16]. In previous studies, the PL lifetime of interlayer excitons depends on temperature strongly, and at high temperatures, the lifetime is shorter than the that of low temperature [15,16]. Thus, our result about the lifetime is consistent with the results which previously reported.

The results of time-resolved PL intensity of interlayer excitons in another sample is shown in Figure 4.18.

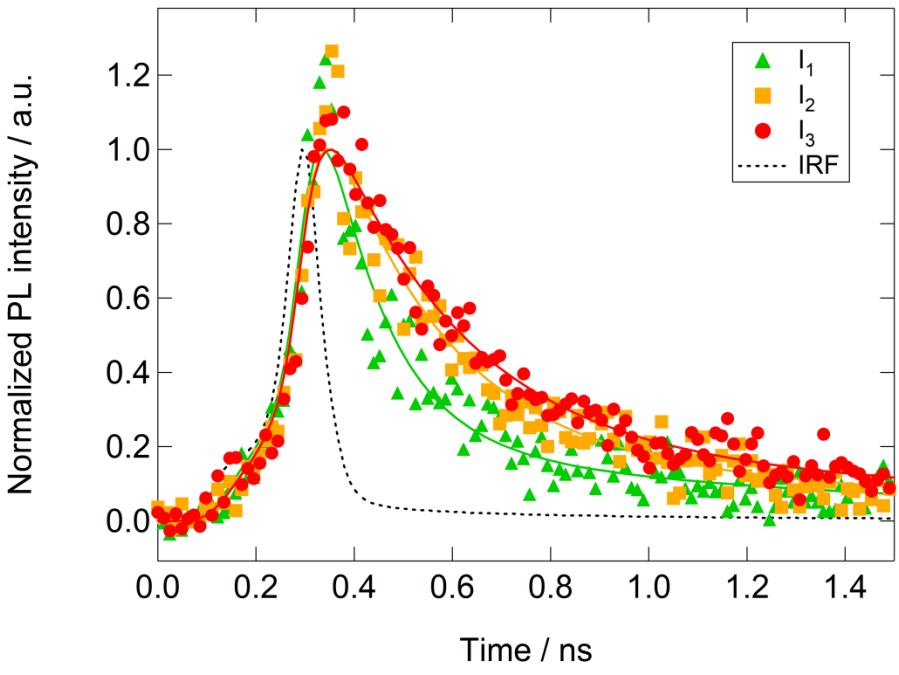

Figure 4.18. Time-resolved PL intensities of I_1, I_2, and I_3 of hBN/WS_2/MoS_2/hBN; the dashed line corresponds to the IRF.

The obtained lifetimes of I_1 (τ_1), I_2 (τ_2), and I_3 (τ_3) are 116 ± 7, 210 ± 13, and 243 ± 12 ps, respectively. We used this value for calculating diffusion coefficient (Section 4.4.2)

4.4.5. PL excitation spectrum

By observing the PL excitation, further information of the interlayer nature of the aforementioned peak can be confirmed. Figure 4.19 shows the result of PLE intensity, which is measured at 40 K.

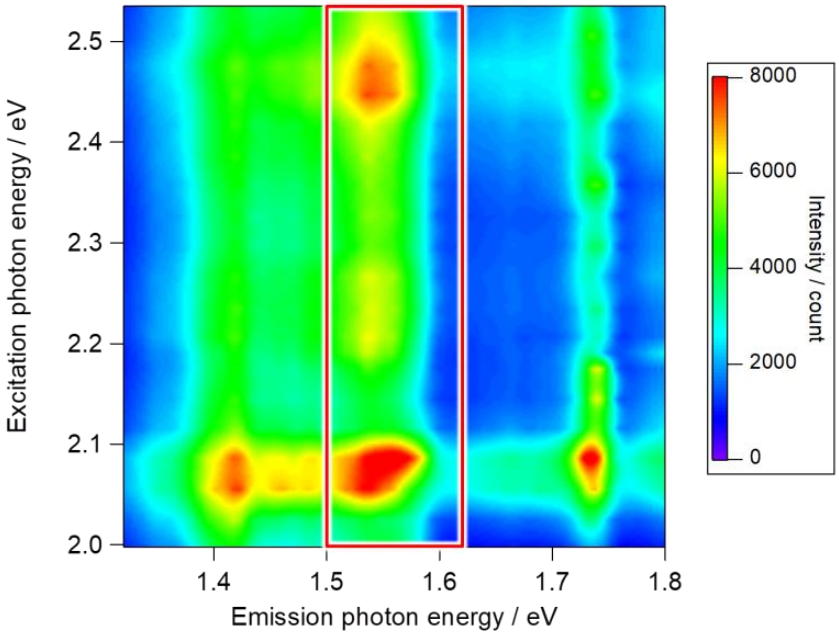

Figure 4.19. PLE plot of hBN/WS_2/MoS_2/hBN heterostructure at 40 K with an excitation power of 0.52–0.90 μJ/cm^2. Peaks with intensity of over 8000 counts are colored as red.

The obtained PL spectra strongly depend on the excitation energy. The region in PL

emission between 1.50-1.62 eV in Figure 4.18 (marked in red) shows the excitation energy dependence of PL emission from a mixture of I_2 and I_3. In this spectral region, there are three peaks at excitation energies of about 2.1, 2.25, and 2.47 eV. This is shown in Figure 4.20(a). These three peak positions match the circled regions labeled I, II, and III in the calculated absorption spectra of the heterostructure (Figure 4.15). These three regions are the point where absorption resonance occurs in the heterostructure, and these resonances would be appeared as peaks in the PLE spectrum. Comparing these regions with individual monolayers reveals that region I corresponds to excitation in MoS_2 B excitons and WS_2 A excitons. On the other hand, regions II and III match with dominant excitations only in MoS_2 and WS_2 B excitons, respectively. The intensity at Region I is stronger than the region II and III because both monolayers are excited. This difference explains the difference in intensity of these three PLE peaks in Figure 4.19. Because charge transfer in MoS_2/WS_2 is very fast and holes can transfer to WS_2 when MoS_2 is excited and vice versa, for electrons if WS_2 is excited [36,46]. Then, even if individual monolayers are excited selectively, interlayer excitons will form. Therefore, interlayer excitons must show emissions in all three (I, II, and III) excitation regions. Thus, because this shows PL intense in all three excitation regions in PLE plot (Figure 4.20(a)), the emission at 1.50–1.62 eV is from PL emission of interlayer exciton. On the other hand, PL emission from I_1 (at approximately 1.73 eV) also shows a similar tendency. In PL emission from I_1, excitonic resonance is appeared but intensity at higher-energy excitation is weaker than that of I_2 and I_3 (Figure 4.20(b)).

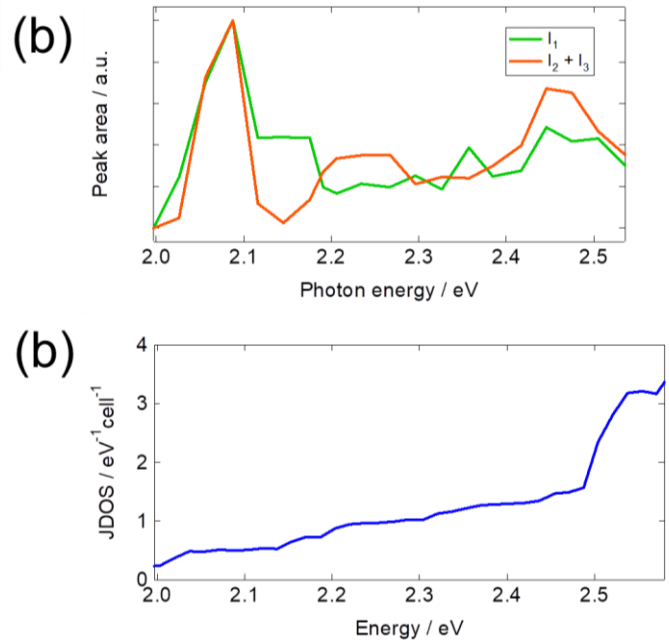

Figure 4.20. (a): Integrated PL intensity of the interlayer exciton peaks of I_1 (1.70–1.765 eV) and mixture of I_2 and I_3 (1.50–1.62 eV) as well as (b): calculated joint density of states (JDOS) of an WS_2/MoS_2 heterostructure from DFT calculations. Some absorption peaks cannot be captured by a single-particle description of ε_2 such as RPA because some peaks are form exciton's excited states.

To get insights into relaxation pathways of photo excited carriers we also calculated the joint density of states (JDOS). Figure 4.20(b) shows the result and this corresponds to the band structure in Figure 4.14. To match the average difference between the bandgap of WS_2 and MoS_2 at the K point and the positions of the A exciton emission from WS_2 and MoS_2 which appear at 2.07 and 1.94 eV, respectively (Figure 4.21), it has been shifted upward by 0.39 eV. Given the size of the sample, the PL emission from MoS_2 is quite weak compared with that from WS_2.

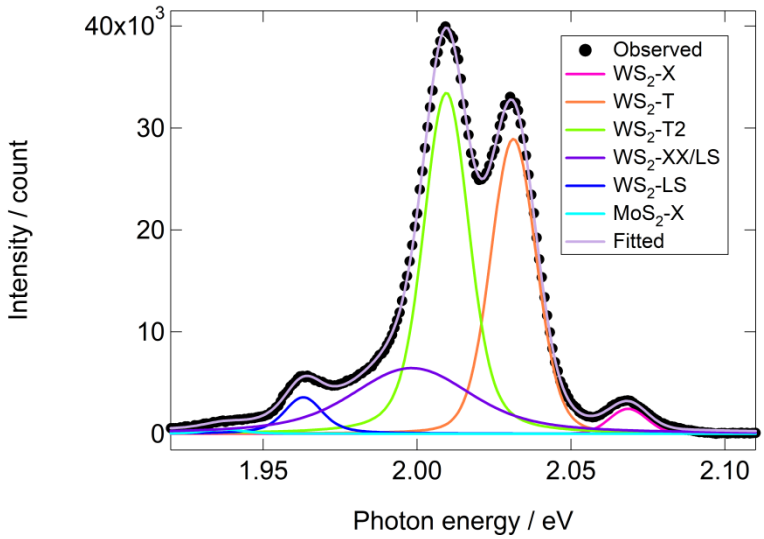

Figure 4.21. PL spectrum arising from intralayer excitons in hBN/WS_2/MoS_2/hBN.

Comparing these three spectra, only the peak which appeared at highest energy region in the PLE spectrum matched by the feature in the JDOS (Figure 4.20). This result indicates that in the absorption properties of the WS_2/MoS_2 heterostructure, excitonic effects play an important role. Then, these properties of the heterostructure cannot be modeled appropriately with single particles. The peak in the JDOS plot appeared at 2.5 eV is from a band-nesting effect. In this region, PL intensity from indirect excitons shows a pronounced peak. However, intensity of I_1 in this energy region is weaker than those of indirect excitons (Figure 4.20(a)). This result suggests that in this region, formation of indirect excitons is more efficiently than those of direct excitons. When in the band-nesting region, photo excited holes and electrons relax in opposite directions in k-space. Then, these carriers may form indirect excitons [47]. This effect may explain the observed difference of the PLE intensity between direct and indirect interlayer excitons.

4.4.6. PL spectrum of WS_2/MoS_2 with different stacking angles

We also prepared heterostructure samples with stacking angle with 0° and 30°. In these samples, the peak positions and appearance of I_1–I_3 depend on the stacking angle (Figure 4.22).

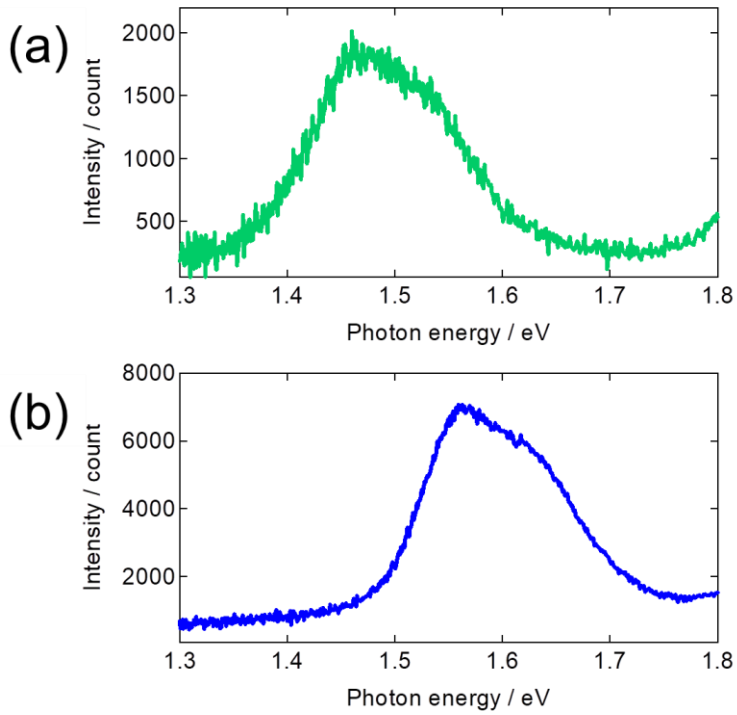

Figure 4.22. Room-temperature PL spectrum of hBN/WS_2/MoS_2/hBN with stacking angles of (a): 0° and (b): 30°.

The peak position in the PL spectrum of the samples with a stacking angle of 0° is similar to those of samples with a stacking angle of 60°. However, with a stacking angle of 30°, the sample shows a large blue shift (~100 meV) than those of 0° or 60°. This large blue shift in the peak position of PL is likely caused by a change in the interlayer distance between WS_2 and MoS_2 by the stacking angle. Modification of the stacking

angle, the interlayer distance can be changed. And this change reduces interlayer coupling in the heterostructure, and modify the energy of the VBM at Γ points and energy gap between K and Γ point [21,23]. When the stacking angle is different from 0° or 60°, the peak energy of the VBM at the Γ point is reduced. This causes modulation of PL peak from indirect excitons (I_2 and I_3) which originate from transition from Q or K point to Γ point. Then, I_2 and I_3 in should show blue shift than those in the sample with a stacking angle of 0° or 60°. In addition, due to the large stacking angle, I_1 transition changes from direct transition to indirect transition [24]. Then, in the sample with a large stacking angle, the I_1 peak is absent. These results are consistent with our hypothesis that these peaks originate from interlayer excitons and with our assignment.

4.5. Conclusion

In summary, we have developed a method for fabricating stacking angle controlled hBN-encapsulated WS_2/MoS_2 heterostructures. Our method is based on the combination of CVD growth method and full-dry-transfer technique. This method enables us to fabricate the clean interface between the layers of heterostructures. The fabricated hBN/WS_2/MoS_2/hBN heterostructures show PL emission not only PL peaks from intralayer but also from interlayer excitons. The PL peak from interlayer excitons can be deconvoluted into three peaks. We succeeded to observe these peaks because the hBN encapsulation make heterostructure with ideal environment and clean interface, which suppressed inhomogeneous broadening of the PL spectra. Theoretical analyses and PL properties measurements revealed that these three PL emissions originate from K–K (direct) interlayer transition and Q–Γ and K–Γ (indirect) interlayer transitions,

respectively. Our results suggest that vdW heterostructures composing multivalley systems like WS_2/MoS_2 can show PL emissions from various interlayer excitons. And these various interlayer excitons may have different decay lifetimes, dispersion lengths, and valley depolarization lifetimes. To develop the valleytronic devices based on vdW heterostructures composed of TMDC, controlling these specifications has important implications.

4.6. References

[1] J. Kim, C. Jin, B. Chen, H. Cai, T. Zhao, P. Lee, S. Kahn, K. Watanabe, T. Taniguchi, S. Tongay, M. F. Crommie and F. Wang, ***Sci. Adv.***, 3, e1700518, (2017).

[2] P. Rivera, J. R. Schaibley, A. M. Jones, J. S. Ross, S. Wu, G. Aivazian, P. Klement, K. Seyler, G. Clark, N. J. Ghimire, J. Yan, D. G. Mandrus, W. Yao and X. Xu, ***Nat. Commun.***, 6, 6242, (2015).

[3] P. Rivera, K. L. Seyler, H. Yu, J. R. Schaibley, J. Yan, D. G. Mandrus, W. Yao and X. Xu, ***Science***, 351, 688-691, (2016).

[4] A. K. Geim and I. V. Grigorieva, ***Nature***, 499, 419-425, (2013).

[5] A. Chernikov, T. C. Berkelbach, H. M. Hill, A. Rigosi, Y. Li, O. B. Aslan, D. R. Reichman, M. S. Hybertsen and T. F. Heinz, ***Phys. Rev. Lett.***, 113, 076802, (2014).

[6] B. Zhu, X. Chen and X. Cui, ***Sci. Rep.***, 5, 9218, (2015).

[7] A. Splendiani, L. Sun, Y. Zhang, T. Li, J. Kim, C. Y. Chim, G. Galli and F. Wang, ***Nano Lett.***, 10, 1271-1275, (2010).

[8] T. Uwanno, Y. Hattori, T. Taniguchi, K. Watanabe and K. Nagashio, ***2D Mater.***, 2, 041002, (2015).

[9] Y. Gong, J. Lin, X. Wang, G. Shi, S. Lei, Z. Lin, X. Zou, G. Ye, R. Vajtai, B. I. Yakobson, H. Terrones, M. Terrones, B. K. Tay, J. Lou, S. T. Pantelides, Z. Liu, W. Zhou and P. M. Ajayan, ***Nat. Mater.***, 13, 1135-1142, (2014).

[10] C. R. Dean, A. F. Young, I. Meric, C. Lee, L. Wang, S. Sorgenfrei, K. Watanabe, T. Taniguchi, P. Kim, K. L. Shepard and J. Hone, ***Nat. Nanotechnol.***, 5, 722-726, (2010).

[11] A. Castellanos-Gomez, M. Buscema, R. Molenaar, V. Singh, L. Janssen, H. S. J. van der Zant and G. A. Steele, ***2D Mater.***, 1, 011002, (2014).

[12] D. Xiao, G.-B. Liu, W. Feng, X. Xu and W. Yao, ***Phys. Rev. Lett.***, 108, 196802, (2012).

[13] K. F. Mak, K. He, J. Shan and T. F. Heinz, ***Nat. Nanotechnol.***, 7, 494-498, (2012).

[14] T. Cao, G. Wang, W. Han, H. Ye, C. Zhu, J. Shi, Q. Niu, P. Tan, E. Wang, B. Liu and J. Feng, ***Nat. Commun.***, 3, 887, (2012).

[15] P. Nagler, G. Plechinger, M. V. Ballottin, A. Mitioglu, S. Meier, N. Paradiso, C. Strunk, A. Chernikov, P. C. M. Christianen, C. Schüller and T. Korn, ***2D Mater.***, 4, 025112, (2017).

[16] B. Miller, A. Steinhoff, B. Pano, J. Klein, F. Jahnke, A. Holleitner and U.

Wurstbauer, ***Nano Lett.***, 17, 5229-5237, (2017).

[17] T. Godde, D. Schmidt, J. Schmutzler, M. Aßmann, J. Debus, F. Withers, E. M. Alexeev, O. Del Pozo-Zamudio, O. V. Skrypka, K. S. Novoselov, M. Bayer and A. I. Tartakovskii, ***Phys. Rev. B***, 94, 165301, (2016).

[18] C. R. Zhu, K. Zhang, M. Glazov, B. Urbaszek, T. Amand, Z. W. Ji, B. L. Liu and X. Marie, ***Phys. Rev. B***, 90, 161302, (2014).

[19] G. Wang, L. Bouet, D. Lagarde, M. Vidal, A. Balocchi, T. Amand, X. Marie and B. Urbaszek, ***Phys. Rev. B***, 90, 075413, (2014).

[20] H.-P. Komsa and A. V. Krasheninnikov, ***Phys. Rev. B***, 88, 085318, (2013).

[21] H. Heo, J. H. Sung, S. Cha, B.-G. Jang, J.-Y. Kim, G. Jin, D. Lee, J.-H. Ahn, M.-J. Lee, J. H. Shim, H. Choi and M.-H. Jo, ***Nat. Commun.***, 6, 7372, (2015).

[22] S. Tongay, W. Fan, J. Kang, J. Park, U. Koldemir, J. Suh, D. S. Narang, K. Liu, J. Ji, J. Li, R. Sinclair and J. Wu, ***Nano Lett.***, 14, 3185-3190, (2014).

[23] N. Lu, H. Guo, Z. Zhuo, L. Wang, X. Wu and X. C. Zeng, ***Nanoscale***, 9, 19131-19138, (2017).

[24] H. Yu, Y. Wang, Q. Tong, X. Xu and W. Yao, ***Phys. Rev. Lett.***, 115, 187002, (2015).

[25] P. K. Nayak, Y. Horbatenko, S. Ahn, G. Kim, J.-U. Lee, K. Y. Ma, A.-R. Jang, H. Lim, D. Kim, S. Ryu, H. Cheong, N. Park and H. S. Shin, ***ACS Nano***, 11, 4041-4050, (2017).

[26] Y. Kobayashi, S. Yoshida, R. Sakurada, K. Takashima, T. Yamamoto, T. Saito, S. Konabe, T. Taniguchi, K. Watanabe, Y. Maniwa, O. Takeuchi, H. Shigekawa and Y. Miyata, ***Sci. Rep.***, 6, 31223, (2016).

[27] M. Okada, T. Sawazaki, K. Watanabe, T. Taniguch, H. Hibino, H. Shinohara and R. Kitaura, ***ACS Nano***, 8, 8273-8277, (2014).

[28] A. M. van der Zande, P. Y. Huang, D. A. Chenet, T. C. Berkelbach, Y. You, G.-H. Lee, T. F. Heinz, D. R. Reichman, D. A. Muller and J. C. Hone, ***Nat. Mater.***, 12, 554-561, (2013).

[29] H. R. Gutiérrez, N. Perea-López, A. L. Elías, A. Berkdemir, B. Wang, R. Lv, F. López-Urías, V. H. Crespi, H. Terrones and M. Terrones, ***Nano Lett.***, 13, 3447-3454, (2012).

[30] T. Taniguchi and K. Watanabe, ***J. Cryst. Growth***, 303, 525-529, (2007).

[31] K. F. Mak, C. Lee, J. Hone, J. Shan and T. F. Heinz, ***Phys. Rev. Lett.***, 105, 136805, (2010).

[32] H. Terrones, E. Del Corro, S. Feng, J. M. Poumirol, D. Rhodes, D. Smirnov, N. R. Pradhan, Z. Lin, M. A. Nguyen, A. L. Elias, T. E. Mallouk, L. Balicas, M. A.

Pimenta and M. Terrones, ***Sci. Rep.***, 4, 4215, (2014).

[33] A. Berkdemir, H. R. Gutiérrez, A. R. Botello-Méndez, N. Perea-López, A. L. Elías, C.-I. Chia, B. Wang, V. H. Crespi, F. López-Urías, J.-C. Charlier, H. Terrones and M. Terrones, ***Sci. Rep.***, 3, 1755, (2013).

[34] C. Lee, H. Yan, L. E. Brus, T. F. Heinz, J. Hone and S. Ryu, ***ACS Nano***, 4, 2695-2700, (2010).

[35] J. Zhang, J. Wang, P. Chen, Y. Sun, S. Wu, Z. Jia, X. Lu, H. Yu, W. Chen, J. Zhu, G. Xie, R. Yang, D. Shi, X. Xu, J. Xiang, K. Liu and G. Zhang, ***Adv. Mater.***, 28, 1950-1956, (2016).

[36] X. Hong, J. Kim, S.-F. Shi, Y. Zhang, C. Jin, Y. Sun, S. Tongay, J. Wu, Y. Zhang and F. Wang, ***Nat. Nanotechnol.***, 9, 682-686, (2014).

[37] C. H. Lui, Z. Ye, C. Ji, K.-C. Chiu, C.-T. Chou, T. I. Andersen, C. Means-Shively, H. Anderson, J.-M. Wu, T. Kidd, Y.-H. Lee and R. He, ***Phys. Rev. B***, 91, 165403, (2015).

[38] N. Kumar, Q. Cui, F. Ceballos, D. He, Y. Wang and H. Zhao, ***Nanoscale***, 6, 4915-4919, (2014).

[39] S. Mouri, Y. Miyauchi, M. Toh, W. Zhao, G. Eda and K. Matsuda, ***Phys. Rev. B***, 90, 155449, (2014).

[40] J. J. Crochet, J. G. Duque, J. H. Werner and S. K. Doorn, ***Nat. Nanotechnol.***, 7, 126-132, (2012).

[41] D. Y. Qiu, F. H. da Jornada and S. G. Louie, ***Phys. Rev. Lett.***, 111, 216805, (2013).

[42] M. Palummo, M. Bernardi and J. C. Grossman, ***Nano Lett.***, 15, 2794-2800, (2015).

[43] H. Fang, C. Battaglia, C. Carraro, S. Nemsak, B. Ozdol, J. S. Kang, H. A. Bechtel, S. B. Desai, F. Kronast, A. A. Unal, G. Conti, C. Conlon, G. K. Palsson, M. C. Martin, A. M. Minor, C. S. Fadley, E. Yablonovitch, R. Maboudian and A. Javey, ***Proc. Natl. Acad. Sci. U. S. A.***, 111, 6198-6202, (2014).

[44] P. H. Dederichs, S. Blügel, R. Zeller and H. Akai, ***Phys. Rev. Lett.***, 53, 2512-2515, (1984).

[45] B. Kaduk, T. Kowalczyk and T. Van Voorhis, ***Chem. Rev.***, 112, 321-370, (2012).

[46] H. Chen, X. Wen, J. Zhang, T. Wu, Y. Gong, X. Zhang, J. Yuan, C. Yi, J. Lou, P. M. Ajayan, W. Zhuang, G. Zhang and J. Zheng, ***Nat. Commun.***, 7, 12512, (2016).

[47] D. Kozawa, R. Kumar, A. Carvalho, K. Kumar Amara, W. Zhao, S. Wang, M. Toh, R. M. Ribeiro, A. H. Castro Neto, K. Matsuda and G. Eda, ***Nat. Commun.***,

5, 4543, (2014).

Appendix

DFT calculations in Chapter 4

We used Vienna Ab Initio Simulation Package (VASP) to perform first-principles DFT calculations [1]. To represent ion-electron interactions, we used all-electron projector augmented wave potentials [2]. To account for the electronic exchange and correlation, the generalized gradient approximation (GGA) parameterized by Perdew-Burke-Ernzerhof (PBE) [3] functional were used. The wave functions were expanded in a plane-wave basis with an energy cut-off of 500 eV. The structure was relaxed until the components of Hellmann–Feynman forces on the atoms were less than 10^{-4} eV/Å. We obtained lattice constant of 3.18 Å for both WS_2 and MoS_2. The stacking order of heterostructure was constructed from the primitive cells of WS_2 and MoS_2 with stacking similar to that observed in 2H-MoS_2 (AA´ stacking). In all of the calculations, a vacuum of 20 Å was used. The interlayer spacing in the heterostructure was optimized using the optB86b-vdW [4] functional. We used this to account for dispersion interactions approximately. Then, we obtained a interlayer distance value of 6.24 Å. In all of the calculations, spin–orbit coupling was included. We used the single-shot G_0W_0 procedure together with a solution of the Bethe–Salpeter equation in the Tamm–Dancoff approximation to calculate the optical spectra [5,6]. This technique correctly accounts for the electron–hole interaction. This interaction is indispensable to obtain an accurate excitonic spectrum. To sample the Brillouin zone for a heterostructure and both monolayers, we used Γ-centered grids of 15 × 15 × 1 and 18 × 18 × 1, respectively. A total of 280 bands, which included 224 empty bands, were used for the heterostructures,

whereas 182 bands with 156 empty bands were included for monolayers. To obtain a converged optical spectrum, these parameters were optimized.

References

[1] G. Kresse and J. Furthmüller, ***Comput. Mater. Sci.***, 6, 15-50, (1996).

[2] P. E. Blöchl, ***Phys. Rev. B***, 50, 17953-17979, (1994).

[3] J. P. Perdew, K. Burke and M. Ernzerhof, ***Phys. Rev. Lett.***, 77, 3865-3868, (1996).

[4] J. Klimeš, D. R. Bowler and A. Michaelides, ***J. Phys.: Condens. Matter***, 22, 022201, (2010).

[5] S. Albrecht, L. Reining, R. Del Sole and G. Onida, ***Phys. Rev. Lett.***, 80, 4510-4513, (1998).

[6] M. Rohlfing and S. G. Louie, ***Phys. Rev. Lett.***, 81, 2312-2315, (1998).

Lists of publications

I. Main Publications (副論文)

1. "Observation of biexcitonic emission at extremely low power density in tungsten disulfide atomic layers grown on hexagonal boron nitride"

   Mitsuhiro Okada, Yuhei Miyauchi, Kazunari Matsuda, Takashi Taniguchi, Kenji Watanabe, Hisanori Shinohara, and Ryo Kitaura

   Sci. Rep., 7, 322 (2017).

2. "Direct and Indirect Interlayer Excitons in a van der Waals Heterostructure of hBN/WS_2/MoS_2/hBN"

   Mitsuhiro Okada, Alex Kutana, Yusuke Kureishi, Yu Kobayashi, Yuika Saito, Tetsuki Saito, Kenji Watanabe, Takashi Taniguchi, Sunny Gupta, Yasumitsu Miyata, Boris I. Yakobson, Hisanori Shinohara, and Ryo Kitaura

   ACS Nano Accepted.

II. Reference Publications (参考論文)

1. "Direct Chemical Vapor Deposition Growth of WS_2 Atomic Layers on Hexagonal Boron Nitride"

   Mitsuhiro Okada, Takumi Sawazaki, Kenji Watanabe, Takashi Taniguchi, Hiroki Hibino, Hisanori Shinohara, and Ryo Kitaura

   ACS Nano, 8, 8273 (2014).

2. "Suppression of exciton-exciton annihilation in tungsten disulfide monolayers encapsulated by hexagonal boron nitride"

Yusuke Hoshi, Takashi Kuroda, **Mitsuhiro Okada**, Rai Moriya, Satoru Masubuchi, Kenji Watanabe, Takashi Taniguchi, Ryo Kitaura, and Tomoki Machida

Phys. Rev. B., 95, 241403 (2017).

III. International Conference

1. "Direct CVD Growth of Monolayer WS_2 on hBN"

   Mitsuhiro Okada, Takumi Sawazaki, Kenji Watanabe, Takashi Taniguchi, Hiroki Hibino, Hisanori Shinohara, and Ryo Kitaura

   The 17th Joint Symposium of Core-to-Core/IRTG Programs on Elements Function for Transformative Catalysis and Materials, Nagoya, Japan, June 2014.

2. "Substrate effect on photoluminescence properties of tungsten disulfide atomic layers"

   Mitsuhiro Okada, Kenji Watanabe, Takashi Taniguchi, Hisanori Shinohara, and Ryo Kitaura

   Sixth Graphene and 2D Materials Satellite Symposium, NT15 The Sixteenth International Conference on the Science and Application of Nanotubes, Nagoya, June 2015.

3. "Substrate effect on photoluminescence properties of tungsten disulfide atomic layers"

   Mitsuhiro Okada, Kenji Watanabe, Takashi Taniguchi, Hisanori Shinohara, and Ryo Kitaura

   NT15 The Sixteenth International Conference on the Science and Application of Nanotubes, Nagoya, June-Jully 2015.

4. “Observation and Characterization of Biexciton states in high-quality Monolayer WS_2”

   Mitsuhiro Okada, Yuhei Miyauchi, Kenji Watanabe, Takashi Taniguchi, Kazunari Matsuda, Hisanori Shinohara, and Ryo Kitaura

   APS March Meeting 2016, Baltimore, MD, USA, March 2016.

5. “hBN-encapsulated Group-VI TMDC van der Waals Heterostructures : Fabrication and Optical Properties”

   Mitsuhiro Okada, Yusuke Kureishi, Kenji Watanabe, Takashi Taniguchi, Hisanori Shinohara, and Ryo Kitaura

   29th International Microprocesses and Nanotechnology Conference, Kyoto, Japan, November 2016.

6. “hBN-encapsulated Group-VI TMDC van der Waals Heterostructures : Fabrication and Optical Properties”

   Mitsuhiro Okada, Yusuke Kureishi, Shohei Higuchi, Kenji Watanabe, Takashi Taniguchi, Hisanori Shinohara, and Ryo Kitaura

   APS March Meeting 2017, New Orleans, LA, USA, March 2017

7. “Identification of Interlayer Excitons in WS_2/MoS_2 van der Waals Heterostructures”

   Mitsuhiro Okada, Yusuke Kureishi, Alex Kutana, Kenji Watanabe, Takashi Taniguchi, Boris I. Yakobson, Hisanori Shinohara, and Ryo Kitaura

   The 8th A3 Symposium on Emerging Materials: Nanomaterials for Energy and Electronics, Suzhou, China, October 2017

8. “Identification of Interlayer Excitons in WS_2/MoS_2 van der Waals Heterostructures”

   Mitsuhiro Okada, Yusuke Kureishi, Alex Kutana, Kenji Watanabe, Takashi Taniguchi, Boris I. Yakobson, Hisanori Shinohara, and Ryo Kitaura

JSPS-DST Japan-Indo Conference in Nagoya, Nagoya, Japan, November 2017.

Main Publications